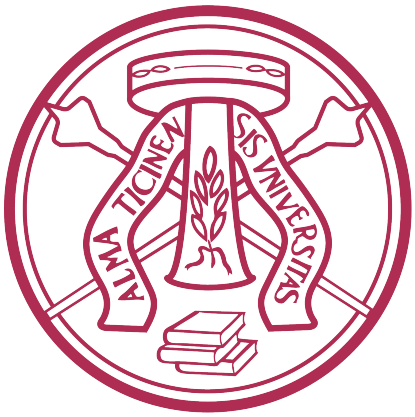


UNIVERSITÀ
DI PAVIA

Physics Departement

Master Degree in Physical Sciences

Characterization of the Signal-over-Fiber Readout Electronics for the DUNE Vertical Drift

Thesis for the degree of:
Anna Galletti

Supervisor:
Prof. Alessandro Menegolli
Università degli Studi di Pavia
Co-supervisor:
Dr. Sabrina Sacerdoti
CNRS, APC Laboratoire, Paris

A.A. 2025-2026

Abstract

Questa tesi illustra le tecnologie che verranno impiegate per la rivelazione dei neutrini nella futura costruzione dell'esperimento DUNE (Deep Underground Neutrino Experiment). DUNE è un esperimento long-baseline di nuova generazione, che si pone come obiettivo principale quello di trovare una risposta ad alcune delle questioni irrisolte del Modello Standard, attraverso il fenomeno dell'oscillazione dei neutrini.
Per la rivelazione di queste particelle, il progetto DUNE mira a sviluppare una tecnologia innovativa basata sulla precisione dei rivelatori Time Projection Chamber (TPC), implementati in argon liquido (LAr) e su scala dimensionale senza precedenti. Questa tecnologia impone alcuni requisiti molto stringenti, tra cui il funzionamento dei dispositivi a temperatura criogenica e la necessità di un Photon Detection System (PDS) estremamente efficiente.
Il presente lavoro approfondisce il PDS e, in particolare, il sistema di readout elettronico del segnale di scintillazione che le particelle cariche producono attraversando il LAr. La tesi presenta quindi il lavoro svolto durante il tirocinio, svolto nell'ambito del programma Erasmus Traineeship, presso il laboratorio APC di Parigi, il quale è impegnato nello sviluppo dell'elettronica di readout per il modulo Vertical Drift del Far Detector di DUNE.
Nello specifico verrà presentato il lavoro di sviluppo e calibrazione del testbench che servirà a validare alcune delle schede elettroniche della catena di acquisizione del segnale. Infine, verranno discussi i test di caratterizzazione di alcuni componenti elettronici chiave del sistema di readout, come laser e fotodiodi, che contribuiranno alla realizzazione del progetto finale.

This thesis illustrates the technologies that will be employed for neutrino detection in the construction of the Deep Underground Neutrino Experiment (DUNE). DUNE is a next-generation long-baseline experiment that aims to answer to some of the unresolved questions of the Standard Model, through the phenomenon of neutrino oscillation.
For the detection of these particles, the DUNE project aims to develop an innovative technology based on the precision of Time Projection Chamber (TPC) detectors, implemented in liquid argon (LAr) and on an unprecedented dimensional scale. This technology imposes some very stringent requirements, including the operation of certain devices at cryogenic temperatures and the need for an extremely efficient Photon Detection System.
The present work delves into the PDS and, in particular, the electronic readout system of the scintillation signal that charged particles produce crossing the LAr. The thesis therefore presents the work carried out during the internship at the APC laboratory in Paris, which is engaged in the development of the readout electronics for the Vertical Drift module of the Far Detector.
The construction of the experiment is starting. This thesis describes the development and calibration of the testbench that will serve to test some of the electronic boards of the signal acquisition chain will be presented. Finally, the characterization tests of some key electronic components of the readout system, such as lasers and photodiodes, which will contribute to the realization of the final project, will be discussed.

Contents

1 Neutrino Physics in the Standard Model **9**
- 1.1 Discovery and Fundamental Properties of Neutrinos . . . 9
  - 1.1.1 Neutrino Interactions . . . 13
- 1.2 Neutrino sources . . . 14
  - 1.2.1 Solar Neutrinos . . . 15
  - 1.2.2 Others Neutrino Sources . . . 17
- 1.3 Neutrino Mass Problem and Flavor Oscillations . . . 19
  - 1.3.1 Neutrinos Oscillations . . . 20
  - 1.3.2 The Mixing Parameters . . . 21
  - 1.3.3 Mass Ordering and Matter Effects . . . 27
- 1.4 Open Problems in Neutrino Physics . . . 31

2 Deep Underground Neutrino Experiment (DUNE) **32**
- 2.1 Physics's goal of the detector . . . 34
- 2.2 The LBNF Neutrino Beam . . . 36
- 2.3 The DUNE Near Detector Complex . . . 38
- 2.4 The DUNE Far Detector . . . 39
  - 2.4.1 LArTPC Technology . . . 40
  - 2.4.2 The Horizontal Drift Far Detector . . . 42
  - 2.4.3 The Vertical Drift Far Detector . . . 43
  - 2.4.4 ProtoDUNE . . . 46

3 DUNE Vertical Drift Photodetection System **47**
- 3.1 LAr Scintillation Light Production . . . 47
- 3.2 The X-ARAPUCA Technology . . . 49
- 3.3 Photodetecion System in VD . . . 53
  - 3.3.1 Power over Fiber System . . . 54
- 3.4 Signal over Fiber System . . . 55
  - 3.4.1 Cold electronics . . . 55
  - 3.4.2 Warm electronics . . . 59

4 Measurements at APC laboratory **62**
4.1 SoF Transmitter and Laser Characterization 62
4.2 SoF Warm Receiver Testbench 69
4.2.1 Setup Descriprition 70
4.2.2 DAQ description 81
4.2.3 System Stability and Setup Calibration 83
4.3 SoF Warm Receiver Measurement 87
4.3.1 Receiver's channels performance 87
4.4 Results of the Measurements 100

Introduction

"In Neutrino phisycs, the fields makes discoveries
but it cries out for more events,
better reconstructed events,
and the only answer to that is to build better and larger detectors."

— Francis Halzen, Nobel prize 2026

The Standard Model theory represents the fundamental pillar of our understanding of fundamental interactions and the universe at the subatomic level. Developed and refined starting from the second half of the twentieth century, this theory elegantly brings together 17 fundamental particles, describing their dynamics through three fundamental interactions: the electromagnetic interaction, the weak force, and the strong force.

However, among the particles described by the model, neutrinos have recently stood out as the most mysterious and fascinating. From their first theoretical postulation to modern measurements, the numerous peculiarities that distinguish them have made their study one of the most active and stimulating fields of modern research.

They are neutral fermions, lacking electric charge, and endowed with an extremely small mass. For many years, in fact, theory incorrectly described them as massless particles. Neutrinos interact with matter almost exclusively through the weak force, coupling based on their flavor (electron, muon, or tau) solely with the left-handed component of the corresponding charged leptons within the isospin doublets.

One of the most difficult experimental challenges in the study of these particles is related to their extremely low cross-section; their probability of interacting with matter is so low that it makes them incredibly elusive and difficult to detect.

This extremely weak interaction has led the scientific community to develop increasingly cutting-edge technologies. To observe these rare events, the need arose to design detectors with gigantic volumes and enormous target masses, often positioned in underground laboratories to shield the background noise of cosmic rays, with the aim of maximising the interaction probability. All these characteristics, from their elusive nature to the discovery of flavor oscillations, will be illustrated and explored in depth in a chapter dedicated to the history and physics of the neutrino.

The second chapter will present in detail the DUNE (Deep Underground Neutrino Experiment) project, an ambitious new-generation long-baseline experiment designed to study the phenomenon of neutrino oscillations with unprecedented sensitivity. The experimental structure necessary to detect the oscillation of these particles is extremely complex and is divided into several fundamental components. Firstly, it is essential to have a controlled source, namely an intense neutrino beam whose kinematic properties, such as energy and momentum, are known with extreme precision. Knowing the exact initial composition of the beam in terms of flavor is an essential requirement; for this reason, the project includes the construction of a near detector whose task is to characterise the primary flux before state transitions occur. Subsequently, after traveling the optimal distance to maximize the oscillation probability, the particles will be observed in the Far Detector. The primary physical objectives of this massive apparatus range from the definitive determination of the neutrino mass ordering to the measurement of the CP symmetry violation phase, parameters whose implications are of crucial importance for the entire physics of fundamental interactions.

However, the realization of this experiment also represents a technological challenge, as it requires combining two apparently contrasting characteristics. On one hand, extremely high resolution in event reconstruction is needed to ensure maximum precision in measuring oscillation parameters; on the other hand, it is essential to have a very large-scale target volume to compensate for the extremely low cross-section typical of neutrino electroweak interactions. The DUNE project aims to reach this delicate compromise by implementing, for the first time on masses of tens of kilotons, the Liquid Argon Time Projection Chamber (LArTPC) technology.

The use of this technology, in turn, requires a highly efficient scintillation light photodetection system. In this regard, the third chapter will illustrate the operation of the Photon

Detection System (PDS) within the Vertical Drift (VD) module, with particular attention to the X-ARAPUCA technology. The latter is essential for capturing the VUV (vacuum ultraviolet) photons produced by the liquid argon and shifting their wavelength toward the visible spectrum, thus making them detectable by silicon photomultipliers (SiPMs).

Numerous international research centers collaborate on the development of this project; in particular, the work described in this thesis is part of the activities of the DUNE group at the APC (AstroParticule et Cosmologie) laboratory in Paris. This group focuses on the development of the electronic readout system associated with the X-ARAPUCA modules positioned directly on the cathode surface of the VD module. Since the cathode operates at very high voltages (up to hundreds of kilovolts), it is impossible to use traditional copper cables; the design solution requires the use of special optical fibers (Signal-over-Fiber, SoF technology) to transport the light signal outside the cryostat, ensuring perfect electrical insulation.

Finally, the fourth chapter will present the experimental measurements carried out in the laboratory, aimed at characterizing and validating the correct operation of the entire optical transmission and reception electronic chain. It will also describe in detail the work done for the design and optimization of the testbench for the room-temperature reception boards (warm receiver). This test apparatus will play a crucial role during the subsequent large-scale production phase, allowing for quick and automated verification that the response of each board maintains the rigorous standards of linearity and uniformity required for the success of the DUNE experiment.

Chapter 1

Neutrino Physics in the Standard Model

The discovery of the neutrino and the subsequent theoretical and experimental breakthroughs represent relatively recent milestones in particle physics. Due to this ongoing evolution, the neutrino remains one of the most compelling subjects of modern fundamental research. To understand the reasons driving this profound interest, this initial chapter is dedicated to examining the fundamental characteristics of the particle and outlining some critical questions about neutrino's physics that still remain unanswered.

1.1 Discovery and Fundamental Properties of Neutrinos

Neutrinos were proposed in 1933 whilst studying the energy spectrum of the electron/ positron pair involved in β decay. The β decay is a spontaneous process in certain nuclei, whereby the decaying nucleus transforms into a different nucleus; the nucleus changes its atomic number by swapping a neutron for a proton(proton for a neutron), whilst simultaneously emitting an electron (positron).
James Chadwick, followed by Ellis and Wooster, was the first to carry out studies on the energy spectrum of the particles emitted during the decay; the result was a continuous energy spectrum, which led Wolfgang Pauli in 1930 to conclude that the description of the decay process was incomplete[1].

In order to provide a complete description of β decay, the conservation of energy, momentum and total spin, together with the continuous energy spectrum observed experimentally, it becomes necessary to introduce the neutrino: a neutral particle (due to charge conservation), with half-integer spin (due to angular momentum conservation) and

proposed massless.
The neutrino undoubtedly interacts with matter, taking part in the decay processes of radioactive nuclei; however, as a neutral particle, it cannot interact electromagnetically. This led Heisenberg and Fermi, as well as Dmitri Iwanenko and Igor Tamm, to investigate more thoroughly the nature of the interaction in which a neutron is transformed into a proton, emitting an electron and a neutrino. This study culminated in Fermi's formulation of beta decay, which modeled the phenomenon as a point-like, four-fermion contact interaction[2].

While this theory is incomplete in describing all possible weak processes at higher energies, it represented a monumental theoretical leap. Utilizing Fermi's mathematical framework, Hans Bethe and Rudolf Peierls calculated the theoretical cross-section for neutrino-nucleon interactions for the first time in 1934. They demonstrated that the interaction probability was extremely small, yielding a value on the order of $\sigma \approx 10^{-43}$ cm^2.

Due to this extremely small cross-section, detecting the neutrino directly seemed almost impossible for a long time. However, in the 1950s, Frederick Reines and Clyde Cowan solved this problem by placing their detector near the Savannah River nuclear reactor and they officially become the first to measure the flux of invisible particles, by detecting the products of β-inverse decay[3] [4]:

$$\bar{\nu} + p \rightarrow e^+ + n \tag{1.1}$$

The electron and the neutron had to be detected in coincidence via scintillation processes; the coincident events had to be correlated with the number of observed decay events, which in turn depended on the cross-section of the interactions as predicted by Fermi's theory. This experimental confirmation earned Reines the Nobel Prize in 1995, see Fig. 1.1a.
The confirmation of the existence of the neutrino is merely the starting point for a deeper investigation of its fundamental properties and its exact placement within the theoretical framework of the Standard Model (SM).

Also around the 1950s, Lee and Yang began to develop chiral theories to describe physical phenomena that use the helicity of a particle as a fundamental parameter [5]. Helicity is a quantum mechanical observable defined as the projection of a particle's spin vector onto the direction of its momentum vector. It determines the "handedness" of a particle: if the spin aligns with the direction of motion, the particle has positive helicity and it's called "right-handed" (RH), whereas if the spin is anti-parallel to the motion, it has negative

helicity and it's called "left-handed" (LH). In the Dirac formalism, chiral eigenstates are determined using the γ_5 matrix: LH particles correspond to an eigenvalue of -1, whereas RH particles correspond to an eigenvalue of $+1$.
For strictly massless particles, helicity is an intrinsic, Lorentz-invariant property.
In a chiral theory, the particle's interaction is strictly dependent on its chirality. Since helicity is not invariant under parity transformation, chiral theories violate parity conservation, and interactions involving LH particles have different probabilities to those involving right-handed particles. Assuming neutrinos to be massless, purely LH particles, any parity-reversed interaction would require a right-handed neutrino. As the weak force does not interact with right-handed neutrinos, such mirror processes are entirely suppressed.

These properties emerge and are verified in two extremely important experiments. C.S. Wu's experiment[6], in 1956, utilises the possibility to reverse a magnetic field to verify that, under parity transformation, the number of β decay events recorded differs, and therefore the probability of interaction changes.
The experiment, shown in Fig 1.1b, utilises the β decay of ^{60}Co and measures the direction of the emitted photons using scintillation detectors; the fact that the probability of observing events involving right-handed electrons is greater than in the opposite configuration confirms that weak interactions (such as those occurring in β decay) do not conserve parity.

In 1958, a year later, M. Goldhaber, L. Grodzins and A.W. Sunyar succeeded in measuring the intrinsic helicity of the neutrino, which turned out to be an intrinsically left-handed particle. Its antiparticle $\bar{\nu}$, by contrast, exhibits the opposite property and is a purely RH particle. At this point, the neutrino appears as a massless, charge-neutral fermion with intrinsic helicity, ready to be incorporated into the framework of Dirac's theory alongside the other half-integer spin fermions.

The chiral states of a particle, which are eigenstates of the parity operator, represent solutions to the Dirac equations. In the case of neutrinos, as they possess intrinsic helicity, the chiral eigenstate is nothing other than the particle itself. This type of eigenstate and these considerations have made it possible to formulate the V-A theory of β decay, a theory that follows the pattern of QED but takes the form of a point-like interaction, without a propagator, with ad hoc currents.

This initial result will be better contextualised within the theory of electroweak interactions, where the neutrino fits perfectly within the LH lepton doublets and interacts via



(a) F. Reines and C. Cowan at the Savannah River plant, operating the equipment that provided the first direct detection of the electron antineutrino in 1956.

(b) Dr. C.S. Wu alongside the experimental setup used to observe the asymmetric beta decay of ^{60}Co, demonstrating parity violation in weak interactions.

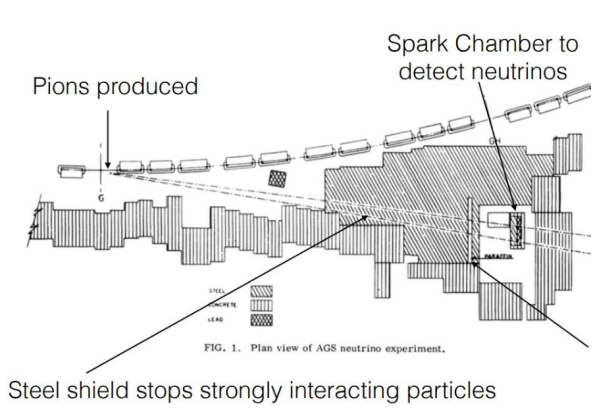
(c) Characteristic particle tracks recorded in a bubble chamber, a pivotal detection technique for observing neutrino interactions and weak neutral currents.

Figure 1.1: Key experimental milestones in the early study of weak interactions and neutrino physics.

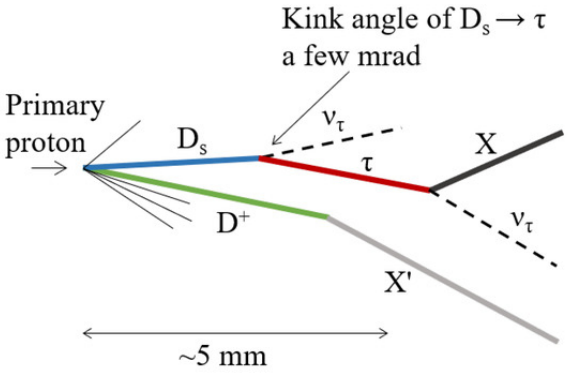
the charged W^+/W^- bosons and the neutral Z_0 boson.
Given that the masses m_W and m_{Z_0} are very large (80.3 and 91.2 GeV respectively), the weak interaction has a very short range, and at low energies the weak interaction can be considered effectively local, and can therefore be approximated by the theory formulated by Fermi[7].

The development of this theory leads to the discovery of an important new property of the particle: its flavor. Indeed, the neutrino is categorised into three lepton families and can always be identified as an electron neutrino ν_e, a muon neutrino ν_μ or a tau ν_τ neutrino. The direct experimental discovery of the other two types of neutrinos stems from weak interactions other than beta decay, such as, for example, the decay of pions and mesons, which decay into muon neutrinos via weak interactions, shown in Fig. 1.2a. The experiment was carried out in 1962 at Brookhaven National Laboratory[8].
While the tau lepton was discovered in 1975 by Martin Perl at SLAC[9], the tau neutrino (ν_τ) proved exceptionally difficult to observe. Before its discovery, the famous experimental confirmation of neutral-current electroweak processes, mediated by the Z_0 boson, took place in 1973 in the Gargamelle bubble chamber at CERN[10], fig. 1.1c. Precision measurements conducted in 1989 at CERN's Large Electron-Positron (LEP)[11] collider mapped the decay width of the Z^0 boson, providing empirical confirmation that there are exactly three generations of active, light neutrinos coupled to the electroweak gauge bosons.

Finally, Tau neutrino was officially detected only in 2000 by the DONUT experiment at Fermilab, recognized by its characteristic track "kink[12], see in Fig 1.2b."



(a) AGS experiment for the discovery of ν_μ



(b) Schematic of the dacay of D_s for the discovery of ν_τ in DONUT experiment

Figure 1.2: On the left a), the plan view of the AGS neutrino experiment that led to the discovery of the muon neutrino (ν_μ). A proton beam creates pions which decay into muons and neutrinos; a massive steel shield stops all strongly interacting particles and muons, allowing only neutrinos to reach the spark chamber detector. On the right b), the accelerator-based production of tau neutrinos (ν_τ), as observed in experiments like DONUT. A primary proton beam interacts with a target to produce a D_s meson, which decays into a tau lepton (τ) and a tau neutrino, exhibiting the characteristic decay kink.

1.1.1 Neutrino Interactions

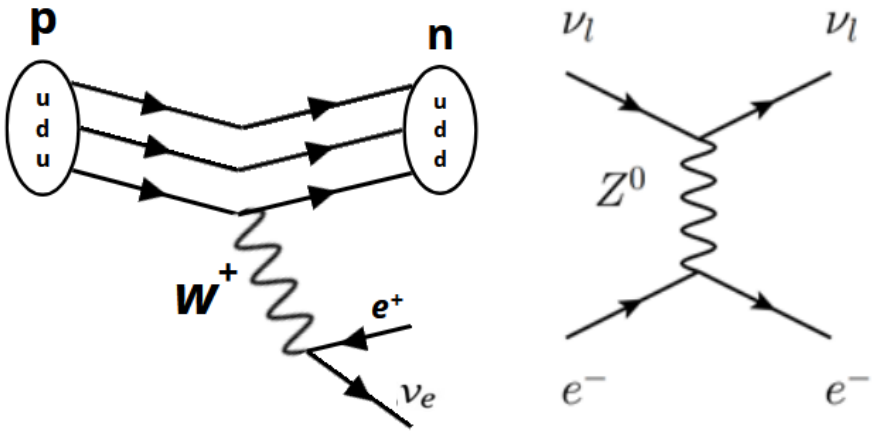
In the Standard Model, the electroweak sector unifies two types of interactions that initially appeared distinct: the weak interaction and electromagnetism. Leptons are organized into Left-Handed (LH) weak isospin doublets based on the three lepton families. Right-Handed (RH) states, on the other hand, participate as singlets of e, μ, τ, as RH neutrinos have not been observed.

$$L_\ell = \begin{pmatrix} \nu_\ell \\ \ell^- \end{pmatrix}_L, \quad \ell = e, \mu, \tau. \tag{1.2}$$

In the framework of the Standard Model, a current represents the flow of fermions coupling to a mediating gauge boson to facilitate a fundamental interaction. Depending on whether the interaction involves an exchange of electric charge, the current is classified as either a Charged Current (CC) or a Neutral Current (NC)[7].

- **Charged-Current (CC) interactions** are mediated by the charged $W^{\pm}$ bosons. To conserve charge in both the initial and final states, the interaction vertex connects two different states of the same weak isospin doublet (e.g., a neutrino converting into its corresponding charged lepton). Common detection channels include inverse beta decay and charged-current quasi-elastic (CCQE) scattering on nucleons. A CC diagram is represented in Figure 1.3a.

- **Neutral-Current (NC) interactions** are mediated by the neutral Z^0 boson. In this case, the vertex of the Feynman diagram connects a fermion to itself; the transition involves an exchange of momentum, but no exchange of electric charge or flavor. Typical channels include elastic neutrino-electron scattering and coherent elastic neutrino-nucleus scattering. An example of this type of interaction is represented by the Feynman diagram in Figure 1.3b.



(a) Charged-Current (CC) interaction mediated by the W^+ boson, illustrating the exchange between a lepton and a nucleon.

(b) Neutral-Current (NC) elastic scattering of a neutrino off an electron, mediated by the Z^0 boson.

1.2 Neutrino sources

In this session, we explore the primary neutrino sources in detail, driven by two main objectives. On the one hand, these sources represent the essential primary sources for experiments, providing us with the fluxes required to analyse the physical phenomena associated with these particles in the laboratory. On the other hand, studying them is fundamental to tracing the evolution of our theoretical understanding, demonstrating how

the analysis of these effects continues to guide and shape cutting-edge research in physics across various fields, from high-energy physics to astrophysics.

1.2.1 Solar Neutrinos

In 1938, research into the solar model had been carried out, which explored in depth the chemical reactions that produce solar energy and, more generally, the nuclear fusion that powers star formation.
Bethe's work highlighted how the Sun is a source of electron neutrinos, which are emitted during thermonuclear fusion processes in the core of a star at an energy of approximately 1 MeV[13][14]. The most interesting aspect drawing attention to these particles, particularly during the development of standard solar models, is the fact that they can be regarded as ideal probes originating from the solar core, as their interaction with matter on their journey towards Earth is practically negligible.

It soon became clear that, despite a considerable flux of neutrinos ($610^{10} cm^{-2} s^{-1}$), their cross-section is so small that ingenious methods are required to detect them.
At the end of 1964, John Bahcall proposed using the reaction that converts chlorine into argon to observe neutrinos. This marked the start of construction of the first major Homestake experiment[15] conducted by Ray Davis.

Located 1,478 metres underground in the Homestake gold mine in South Dakota, the experiment utilised a large horizontal tank containing 615 tonnes of perchloroethylene (C_2Cl_4), equivalent to approximately 2.16×10^{30} atoms of chlorine-37. By utilising the inverse beta decay reaction ($\nu_e + {}^{37}\mathrm{Cl} \rightarrow {}^{37}\mathrm{Ar} + e^-$) with an energy threshold of 0.814 MeV, Homestake measured an average capture rate of approximately 2.56 SNU[1]. However, this result was in stark contrast to theoretical predictions: John Bahcall's Standard Solar Model predicted a capture rate of around 8 SNU. The fact that Homestake observed only about a third of the expected electron neutrinos introduced a profound anomaly that became famously known as the Solar Neutrino Problem.

A significant practical limitation of this experimental setup was its energy threshold. While the Standard Solar Model predicts that neutrinos are produced across various stages of the nuclear cycle with distinct energy spectra, the detector was only sensitive to a small

[1]SNU is a unit of measurement used in neutrino physics to quantify the capture rate of solar neutrinos. It is defined as 10^{-36} neutrino captures per target atom per second.

fraction of higher-energy neutrinos. The complete solar neutrino spectrum includes pp, ^{7}Be, pep, and ^{8}B neutrinos, along with a small contribution from the CNO cycle. Homestake chlorine experiment was energetically sensitive only to the higher-energy ^{7}Be and ^{8}B neutrinos, consequently, the most abundant, low-energy solar neutrinos remained entirely undetected.

To verify this deficit at lower energies, other radiochemical experiments were devised. These experiments utilised a specific capture reaction with a very low energy threshold of 0.233 MeV: an incoming electron neutrino interacts with a ^{71}Ga nucleus, transmuting it into radioactive ^{71}Ge and emitting an electron.
The detectors employed utilised enormous quantities of gallium chloride solution (101 tonnes in total)and confirmed the discrepancy with the results obtained at a significance level greater than 5σ.

The next step was taken with the design of the Cherenkov water detector. Kamiokande was the first direct-counting experiment: a large detector containing 3,000 tonnes of water, in which ultra-relativistic particles emit the characteristic Cherenkov light cone, detected by 1,000 PMTs arranged on the surface.
Following improvements to the detector, the detection of solar neutrinos began in 1986, with a threshold of 7 MeV (i.e. sensitivity limited to solar ^{8}B neutrinos only).
Kamiokande observed the scattered electrons from the elastic reaction $\nu_e + e^- \rightarrow e^- + \nu_e$.
In 1989, Kamiokande announced that it had observed only about 45 per cent of the expected solar neutrinos, confirming the solar neutrino problem.

This experimental evidence points to three possibilities: the first is the hypothesis that the experiments were incorrect, which is unlikely; the second is that the solar models that had been developed were incorrect, but this would have been strange as they had yielded other consistent and stable results; and the third hypothesis was that the electron neutrinos produced in the solar core changed their flavor and arrived on Earth as ν_μ and ν_τ.

The hypothesis of neutrino oscillation is the most likely, but it needs to be verified. This occurred in 1985, when Herbert Chen discovered a reaction capable of measuring the flux of solar neutrinos, regardless of their flavor. This reaction is:

$$\nu_x + d \text{ß} \nu_x + p + n \tag{1.3}$$

The decisive experiment at the Sudbury Neutrino Observatory (SNO)[16] uses a large Cherenkov detector containing 1,000 tonnes of heavy water (D_2O), monitored by 9,500

photomultipliers. In 2001, a major result, illustrade in Fig. 1.4, was reported: the total neutrino flux is similar to that predicted by standard solar models (approximately $5 \times 10^6 cm^{-2} s^{-1}$), although the flux of ν_e is the same as in previous experiments.
This confirms that the solar models are correct and that neutrinos oscillate; a discussion of neutrino oscillation is provided in the next section.

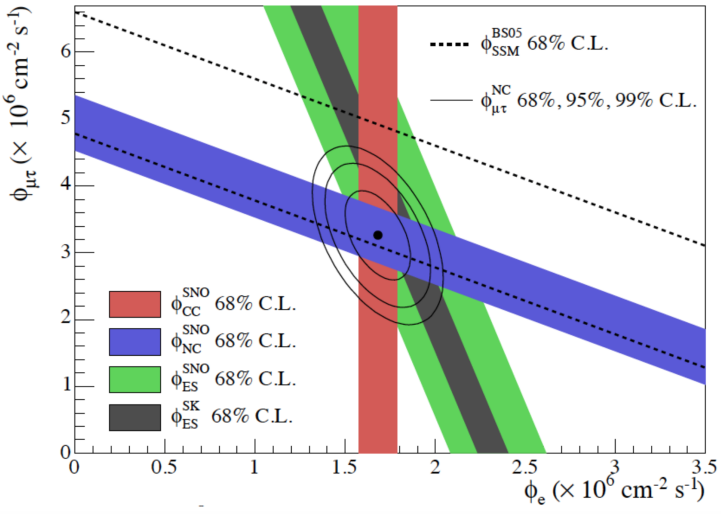


Figure 1.4: Flux of μ and τ neutrinos versus the flux of electron neutrinos. The filled bands show the 68% C.L. measurements for the CC (red), NC (blue), and ES (green) reactions from the SNO experiment, along with the ES measurement from Super-Kamiokande (dark grey). The dashed lines represent the prediction of the Standard Solar Model (SSM). The intersection of the experimental bands demonstrates that the total neutrino flux is consistent with the SSM, confirming the phenomenon of neutrino flavor oscillation.

1.2.2 Others Neutrino Sources

Atmospheric Neutrinos

Cosmic rays interact in the Earth's upper atmosphere, generating pions and kaons, whose decay produces muons and muon neutrinos; many of these muons subsequently decay into electrons and a pair of neutrinos (a muon neutrino and an electron neutrino).
These fluxes, known as atmospheric neutrinos, were predicted and described in the early 1960s and detected for the first time in 1965 in deep mines in India and South Africa.

Scientific interest in these neutrinos was revived in the early 1980s with the construction of large underground detectors designed to observe the proton decay, against which atmospheric neutrinos represented a background noise.

Between the late 1980s and early 1990s, the Kamiokande and IMB Cherenkov detectors recorded a modest deficit of muon neutrinos from the antipodes, an anomaly initially not confirmed by other track detectors such as Fréjus and NUSEX due to limited statistical data. Although the deficit could theoretically be explained by neutrino oscillation, such a premature announcement was still the subject of heated debate [17].

The definitive breakthrough came with the Super-Kamiokande experiment. In June 1998, after just two years of data collection, the collaboration announced the unequivocal observation of a deficit in muon neutrinos arriving from the opposite side of the Earth, which was immediately interpreted as an oscillation between the muon neutrino and the tau neutrino.
This evidence was subsequently supported by data from other experiments (such as MACRO[18] and Soudan 2[19]) and definitively confirmed by the long-baseline K2K experiment[20], which directed an accelerator-generated muon neutrino beam over a distance of 250 km towards the Super-Kamiokande water Cherenkov detector .

Astrophysical Neutrinos

On February 23, 1987, large underground proton-decay experiments such as Kamiokande II[21] and IMB[22] unexpectedly detected a neutrino burst from Supernova 1987A. This milestone observation confirmed that core-collapse supernovae release immense quantities of neutrinos, carrying away approximately 99% of the explosion's gravitational binding energy[23].
The observable neutrino sky, however, extends far beyond stellar explosions. At the most extreme energies, powerful cosmic accelerators[2]produce astrophysical neutrinos reaching the PeV scale.
The IceCube[24] observatory provided the first historic evidence of this high-energy flux in 2013, effectively inaugurating a new era of multi-messenger astronomy.
At the absolute opposite end of the energy spectrum lie the cosmological neutrinos originating from Big Bang. Having decoupled from the primordial plasma just one second after the universe's birth, these particles now permeate all of space. Nevertheless, their ultra-low kinetic energy, lingering in the micro-electronvolt range, makes their direct experimental detection one of the most formidable challenges in modern physics[23].

[2]such as Active Galactic Nuclei (AGNs) and Gamma-Ray Bursts (GRBs)

Artificial Neutrinos

Nuclear reactors represent an extremely intense and stable artificial source of electron antineutrinos ($\bar{\nu}_e$), generated during the fission of the uranium and plutonium nuclei that make up the fuel.
The resulting fission fragments, being heavily neutron-rich, are unstable and release energy through a chain of β^- decays, emitting electrons and antineutrinos (approximately six $\bar{\nu}_e$ per fission event, with energies of the order of a few MeV).
The detection of these particles in laboratories typically occurs via inverse beta decay ($\bar{\nu}_e + p \rightarrow n + e^+$). This reaction has a very low energy threshold, whilst conversion to heavier flavors via charged currents (such as $\bar{\nu}_\mu + p \rightarrow n + \mu^+$) is kinematically impossible at reactor energies, since the production of a muon requires energy greater than its rest mass ($m_\mu \approx 106$ MeV).

Alongside nuclear reactors, particle accelerators provide another intense and controllable source of artificial neutrinos. In these facilities, a high-power proton beam is smashed into a target and produces a secondary spray of hadrons (predominantly pions).
These charged particles are collected and directed by powerful magnetic horns into a long evacuated decay tunnel[25]. As the pions travel through the tunnel, they decay into muons and muon neutrinos (e.g., $\pi^+ \rightarrow \mu^+ + \nu_\mu$).
Massive absorbers are used to stop the residual hadrons and muons, a collimated beam of neutrinos remains and travels toward the detectors. This technique gives physicists the crucial ability to tune the beam's energy spectrum and select positive or negative pions to create dedicated neutrino or antineutrino beams, making it the cornerstone of modern long-baseline oscillation experiments.

1.3 Neutrino Mass Problem and Flavor Oscillations

In Standard Model theory, neutrinos appear in the Lagrangians as purely LH fields, while antineutrinos, by contrast, appear as RH fields.
These fields are fully integrated into the theory, participating in electroweak interactions as massless particles, as they cannot acquire mass via the Higgs mechanism of spontaneous symmetry breaking. However, the experimental observations discussed in the previous chapter raise an important question regarding whether neutrinos are truly massless particles. This implies that neutrinos are more complex than the Standard Model suggests, pointing towards new physics beyond its current description.

The phenomenon of the neutrino flux deficit, for example, suggests to investigate a potentially undiscovered neutrino mass, since oscillations between different neutrino states would be explained by assuming a mass difference between the particles. Whilst the theory of oscillations has been rigorously developed and verified through various experiments, confirming that neutrinos have mass, as we'll see later, the origin of this mass remains an open question.
The nature of the neutrino's mass could be explained by the following theories:

- The Dirac mass theory requires the existence of a right-handed neutrino, but in a sterile state, which is inert with respect to all interactions in the Standard Model.
- The Majorana theory: the mass term appears at the cost of sacrificing lepton number conservation.
- The seesaw mechanism theory: in this case, RH neutrinos exist, they have a large mass and do not interact, but give rise to the extremely small masses of LH neutrinos.

None of these theories has been verified with certainty, and all remain possible; despite this unresolved question, we can explore the phenomenon of oscillations in detail.

1.3.1 Neutrinos Oscillations

Experiments involving solar neutrinos and atmospheric neutrinos open a significant chapter in neutrino physics: research on neutrino oscillations, which began with Pontecorvo's idea in 1957, when he conceived the possibility of a mechanism for the oscillation of neutrino flavor states during their propagation.
Let us consider the state ν_e, endowed with a certain momentum p, and describe its evolution over time through its wave function $|\nu_e(t)\rangle$. The oscillation mechanism predicts that, during its evolution over time, the same neutrino can become either the ν_μ or ν_τ neutrino with a certain probability, as follows:

$$|\nu_e(t)\rangle = A(t)|\nu_e\rangle + B(t)|\nu_\mu\rangle + C(t)|\nu_\tau\rangle \tag{1.4}$$

To understand this phenomenon, we must distinguish between two different types of eigenstates. Interaction eigenstates are the neutrinos we already know, detected experimentally through their specific flavor and lepton family in electroweak interactions.
To introduce oscillation, however, we must assume that these interaction eigenstates do not have a defined physical mass.

In mathematical terms, this implies that the free Hamiltonian in vacuum is not diagonalized by the flavor eigenstates, but rather by a different set of states known as the mass eigenstates. Consequently, the interaction (flavor) eigenstates are linear combinations of these mass eigenstates, and vice versa. The invertible and unitary matrix that relates the mass eigenstates to the physical flavor states is called U^{PMNS} (Pontecorvo-Maki-Nakagawa-Sakata) and has the following form [23]:

$$U^{PMNS} = \begin{pmatrix} 1 & 0 & 0 \\ 0 & \cos\theta_{23} & \sin\theta_{23} \\ 0 & -\sin\theta_{23} & \cos\theta_{23} \end{pmatrix} \begin{pmatrix} \cos\theta_{13} & 0 & \sin\theta_{13}e^{-i\delta_{CP}} \\ 0 & 1 & 0 \\ -\sin\theta_{13}e^{i\delta_{CP}} & 0 & \cos\theta_{13} \end{pmatrix} \begin{pmatrix} \cos\theta_{12} & \sin\theta_{12} & 0 \\ -\sin\theta_{12} & \cos\theta_{12} & 0 \\ 0 & 0 & 1 \end{pmatrix} P \tag{1.5}$$

Most commonly used in its compact form:

$$|\nu_\alpha\rangle = \sum_i U^*_{\alpha i} |\nu_i\rangle \tag{1.6}$$

Where i is the mass state index and α is the flavor state index. The overall matrix is the product of three 3×3 square matrices, each of which represents a rotation whose main parameter is one of the three mixing angles, and depends on its sine and cosine. In one of the three matrices, a third parameter also appears: the phase δ_{CP}. The P matrix, on the other hand, is a diagonal matrix that depends on two other parameters: the Majorana phases[3].

All these parameters are the focus of current research into neutrino physics; in the following sections, we shall explain what they represent in more detail.

1.3.2 The Mixing Parameters

To understand the role of the mixing angle, it is useful to return to the representation of the Hamiltonian matrix; by considering, for example only two neutrino flavor states, we can see how the mixing phenomenon depends on the difference in the masses of the two mass eigenstates.
In the basis of the mass eigenstates, the matrix is diagonal; its eigenvalues represent the physical energy of the states, given by $E_i = \sqrt{|p|^2 + {m_i}^2}$. With the following considerations:

- The ultra-relativistic approximation where $E_i \approx p + \frac{m_i^2}{2p}$.

[3]If neutrinos were to prove to be Majorana particles, these additional physical phases would not, however, affect oscillation phenomena, but rather other, rarer events.

- The possibility to remove the term p common to the states.
- The possibility to add the common term $-\frac{(m_2^2+m_1^2)}{4p}$.

In the mass eigenstate basis, the corresponding Hamiltonian matrix is time-independent and takes the following form[23]:

$$H = \begin{pmatrix} \frac{m_1^2}{2p} - \frac{(m_2^2+m_1^2)}{4p} & 0 \\ 0 & \frac{m_2^2}{2p} - \frac{(m_2^2+m_1^2)}{4p} \end{pmatrix} = \begin{pmatrix} -\frac{\Delta m^2}{4p} & 0 \\ 0 & \frac{\Delta m^2}{4p} \end{pmatrix} \tag{1.7}$$

Here, it is important to note that $\Delta m^2 = m_2^2 - m_1^2$. In the flavor basis, the Hamiltonian becomes non-diagonal and time-dependent through the action of the mixing matrix, incorporating the phase evolution of the individual mass eigenstates.

At this point, it is easily understood how, in the same way, the time evolution of the interaction state in a vacuum acquires a phase that depends on the square of the difference in masses. Since a flavor state is produced as a quantum superposition of mass eigenstates, its initial composition is determined by the mixing angle θ through trigonometric coefficients. As the system propagates, each mass component evolves independently by acquiring its own phase. Combining these initial projection coefficients with the respective phase factors yields the time-evolved states for the two-flavor framework:

$$|\nu_e(t)\rangle = \left(\cos\theta\, e^{+i\frac{\Delta m^2}{4p}t}\right)|\nu_1\rangle + \left(\sin\theta\, e^{-i\frac{\Delta m^2}{4p}t}\right)|\nu_2\rangle, \tag{1.8}$$

$$|\nu_\mu(t)\rangle = \left(-\sin\theta\, e^{+i\frac{\Delta m^2}{4p}t}\right)|\nu_1\rangle + \left(\cos\theta\, e^{-i\frac{\Delta m^2}{4p}t}\right)|\nu_2\rangle. \tag{1.9}$$

In this case, there are only two neutrinos and a single mass difference term governs the evolution of the states over time. In the three-neutrino case, however, there are three mass differences, which are conventionally denoted as follows[26]

$$\Delta m_{21}^2 = m_2^2 - m_1^2 \tag{1.10}$$

$$\Delta m_{31}^2 = m_3^2 - m_1^2 \tag{1.11}$$

$$\Delta m_{32}^2 = m_3^2 - m_2^2 = \Delta m_{31}^2 - \Delta m_{21}^2. \tag{1.12}$$

Assuming that the parameters of the squared mass differences are known with a good degree of precision, the question regarding the mass of neutrinos remains open in two respects: firstly, the absolute value of any single mass is unknown; and secondly, the correct

order of the masses is also unknown.

Before returning to this problem, we will introduce the key steps that led to the measurement of these initially unknown parameters. Central to this effort is the calculation of flavor change probabilities, which is essential for modeling expected event rates in neutrino detectors.
The survival probability, for a given type of neutrino, indicates the probability that an interaction state will be preserved over time. The transformation probability, into a neutrino of a different flavor, indicates the probability that a neutrino, whilst propagating, will transform into another flavor.

$$P_{survive} = \langle \nu_{initial} | \nu(t) \rangle \tag{1.13}$$

$$P_{disapparence} = 1 - P_{survive} \tag{1.14}$$

Both oscillation probabilities depend on the mixing angle and the square of the mass difference (fixed parameters); if either of these parameters is zero, oscillation cannot occur; they also depend on the neutrino's momentum p.
To investigate the macroscopic effects of neutrino oscillations, it's more practical to use the oscillation length, L_{osc}, which is the distance over which an oscillation is completed, i.e. the phase of the oscillation is 2π.
It is straightforward to introduce the generic distance variable L if we consider that neutrinos are super-relativistic and that we can therefore set $p = E$ and take $t = L$ (if $c = 1$); in this case, the phase of the oscillation of eq. 1.8 changes as follows

$$\frac{\Delta m^2 t}{4p} = \frac{\Delta m^2 L}{4E}. \tag{1.15}$$

From this point onwards, we can evaluate neutrino oscillation experiments based on the baseline distance at which they operate relative to the neutrino energy as can be seen in the table 1.1 below[26].
For experiments utilizing artificial sources, such as long-baseline accelerator beams or nuclear reactors, the setup typically features a near detector to determine the composition of the unoscillated initial flux, and a distant detector located at a baseline L_{osc}. This distance is chosen based on the beam energy relative to the mass difference scale being investigated. Experiments observing natural sources, such as solar or atmospheric neutrinos, rely on a single massive detector and infer the initial flux either from robust theoretical models (e.g., the Standard Solar Model) or by comparing the flux of neutrinos arriving from different zenith angles, which correspond to different travel distances through the Earth.

$\langle E_\nu \rangle$	Neutrino Source	L	$\Delta m^2\,[\mathrm{eV}^2]$
$\sim$ MeV	Reactors	~ 10 m	10^{-1}
$\sim$ MeV	Sun	~ 150 Mkm	$10^{-10} - 10^{-11}$
$\sim$ MeV	Long-baseline reactors	~ 150 km	10^{-5}
~ 10 GeV	Accelerators	~ 100 m	$1 - 10$
$\sim$ GeV	Atmospheric	~ 6000 km	$10^{-2} - 10^{-3}$
$\sim$ GeV	Long-baseline accelerators	~ 150 km	10^{-3}

Table 1.1: Characteristics of different neutrino sources, typical energies, baseline lengths, and squared mass differences.

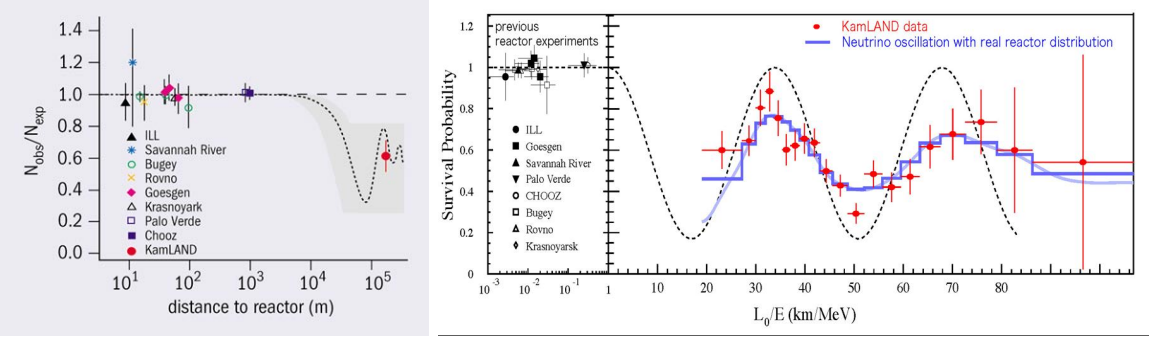
In the most general framework, the transition probability from an initial flavor α to a flavor β is obtained by computing the square modulus of the transition amplitude. By expanding the states through the PMNS mixing matrix components, the probability can be compactly written as:

$$P(\nu_\alpha \to \nu_\beta) = \left| \sum_i U_{\beta i} e^{-i \frac{m_i^2 L}{2E}} U^*_{\alpha i} \right|^2$$

Here, $U^*_{\alpha i}$ and $U_{\beta i}$ represent the complex conjugate and standard elements of the PMNS matrix, respectively, dictating the coupling between the flavor states (α, β) and the mass eigenstates (i). Expanding this square modulus yields both constant terms and oscillatory interference terms, which are directly driven by the non-zero mass splittings Δm^2_{ij} and the kinematic parameter L/E.[4]

Furthermore, the experiments are categorised according to whether they measure the number of neutrinos that have disappeared relative to a specific flavor in the initial beam (disappearance experiments), or the number of neutrinos of a different flavor that have appeared after travelling a specific distance (appearance experiments). The results of oscillation experiments are often presented in graphs showing the probability of oscillation as a function of distance L.
Initially, the aim was to confirm neutrino oscillation by experimentally verifying a point on the function where the probability of oscillation is not equal to 1.

[4]Mathematically, expanding the square modulus produces diagonal elements and off-diagonal cross-terms. These cross-terms are the interference terms; they oscillate with phases proportional to $\Delta m^2_{ij} L/(4E)$ and encapsulate both the flavor transition dynamics and any potential CP-violating effects governed by the complex phase of the PMNS matrix.



(a) Ratio of observed to expected $\bar{\nu}_e$ events as a function of the distance from the reactors.

(b) Survival probability as a function of L_0/E. T

Figure 1.5: Experimental evidence of reactor antineutrino oscillations. The combination of historical short-baseline data and KamLAND results perfectly traces the theoretical expectation for no-oscillation (ratio 1) and the subsequent spectral distortion. Unlike previous short-baseline experiments, KamLAND observes a clear deficit at ~ 180 km. Images adapted from the KamLAND Collaboration.

This was achieved, for example, through the KamLAND experiment, which provided evidence for reactor antineutrino oscillations by being situated at an average distance of approximately 180 km from the source. The parameters investigated by KamLAND define what is known as the solar sector, because these same variables (θ_{12} and the mass splitting Δm^2_{21}) are responsible for the flavor transitions observed in solar neutrinos.

This experiment provided the definitive evidence we expected regarding the non-zero mass difference; therefore, at least one neutrino must have $m \neq 0$.The KamLAND result yields a best-fit that evaluates the optimal agreement between the measured oscillation probability[5], the investigated energies, the mixing angle, and the squared mass difference. The high-precision results from KamLAND provide the following best-fit parameters for the solar oscillation sector [27]:

$$\sin^2(2\theta_{12}) = 0.92^{+0.06}_{-0.07} \tag{1.16}$$

$$\Delta m^2_{21} = (7.59 \pm 0.21) \times 10^{-5}\ \text{eV}^2 \tag{1.17}$$

The first results concerning the second mass-squared difference and the corresponding mixing angle (parameters commonly referred to the atmospheric sector) come from the study of atmospheric neutrinos, in particular the transformation of muon neutrinos into

[5]Experimentally, this is quantified by measuring the survival probability $P(\bar{\nu}_e \to \bar{\nu}_e)$, which manifests as a deficit in the detected electron antineutrino flux compared to the theoretical, unoscillated expectation from the reactors.

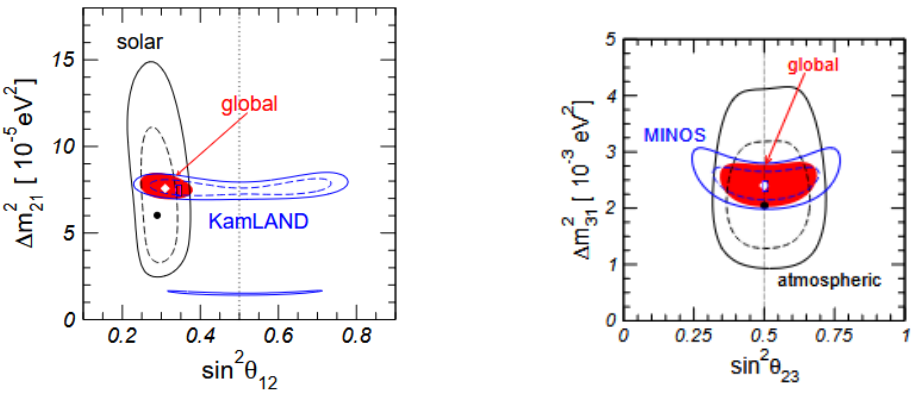
tau neutrinos. This measurement, carried out by the Super-Kamiokande experiment, is consistent with the following best-fit values for the atmospheric sector [28]:

$$\sin^2(2\theta_{23}) \simeq 1.00 \quad (> 0.92 \text{ at } 90\% \text{ C.L.}) \tag{1.18}$$

$$|\Delta m^2_{32}| = (2.8 \pm 0.4) \times 10^{-3} \text{ eV}^2 \tag{1.19}$$

These results were subsequently confirmed by the K2K experiment[29], which utilised a beam of muon neutrinos generated by an accelerator directed towards a detector situated at a distance of approximately 250 km.

The final key element of the three-neutrino mixing matrix, the third angle θ_{13}, was measured experimentally in 2012. While the Daya Bay[30] collaboration provided a highly precise and definitive measurement, this milestone was actually a shared global triumph, with the angle being measured almost simultaneously by other major experiments, including RENO[31], Double Chooz[32], and T2K[33].
Focusing on the Daya Bay setup, the experiment utilised the continuous flux of electron antineutrinos produced by six nuclear reactors, monitoring them at eight underground detection stations situated at both short and long distances. By comparing these measurements, the experiment observed a clear deficit in the arrival rate of electron antineutrinos at the most distant hall.



(a) Solar sector parameters

(b) Atmospheric sector parameters

Figure 1.6: Comparison of the allowed parameter spaces for neutrino oscillations. The left panel shows the constraints on Δm^2_{21} versus $\sin^2\theta_{12}$, displaying individual contours from solar neutrino experiments (black), the KamLAND reactor experiment (blue), and the combined global fit (red). The right panel displays the constraints on Δm^2_{31} versus $\sin^2\theta_{23}$, comparing data from atmospheric neutrino observations (black), the MINOS accelerator experiment (blue), and the corresponding global fit (red).

This measurement made it possible to determine a non-zero value for θ_{13}, in particular the result was $\sin^2 2\theta_{13} = 0.092 \pm 0.017$, with a statistical significance exceeding 5σ. This result definitively completed the picture of the three standard mixing angles, paving the way for research into CP violation in the lepton sector.

Let us now examine the role of the phase δ_{CP} in more detail. For values of $\delta_{CP} \neq 0, \pi$, and assuming that none of the elements $U_{\alpha i}$ vanishes, the matrix U_{PMNS} is a complex matrix and therefore CP invariance is violated in the complex sector. To verify this violation of CP symmetry, attempts are made to measure the value of this phase; to achieve this, it is useful to consider that, in practice, this means that neutrinos and antineutrinos have different oscillation probabilities:

$$P(\nu_\alpha \to \nu_\beta) \neq P(\bar{\nu}_\alpha \to \bar{\nu}_\beta) \tag{1.20}$$

While the three-flavor oscillation framework is now firmly established, the experimental sensitivity varies significantly across the different parameters. The solar parameters (θ_{12} and Δm^2_{21}) and the reactor mixing angle (θ_{13}) are currently measured with high precision, typically at the level of a few percent. Conversely, the atmospheric sector requires further refinement.The precise octant of the atmospheric mixing angle remains unresolved.

For the time being, experiments have only begun to set limits on the value of δ_{CP}; for example, the results seem to favour negative values of δ_{CP},but they are not precise enough. In fact, all values between π and 2π, as well as those that preserve symmetry and set $\delta_{CP} = 0, \pi$, are consistent with the global data collected.

An overview of all the current oscillation parameters is provided in Table 1.2.

Sector	**Parameters**	**Dominant Source**	**Current Status**
Solar	θ_{12}, Δm^2_{21}	Sun, Reactors (LBL)	High precision ($\sim 3\%$ uncertainty)
Atmospheric	θ_{23}, $\lvert\Delta m^2_{31}\rvert$	Atmosphere, Accelerators	Octant and mass sign unknown
Reactor	θ_{13}	Reactors (SBL)	High precision
CP Violation	δ_{CP}	Accelerators (LBL)	Weakly constrained

Table 1.2: Summary of neutrino oscillation sectors, their governing parameters, and current experimental sensitivity.LBL and SBL stand for Long-Baseline and Short-Baseline, respectively.

1.3.3 Mass Ordering and Matter Effects

After exploring the role of oscillation parameters and mentioning some of the most important experiments that can be conducted, we can focus on their essential role in future

discoveries regarding particle physics beyond the Standard Model (SM), as anticipated in previous sections.

Although a much more complete general picture of the parameters is now available, the atmospheric sector has not yet been investigated with sufficient precision.
The atmospheric angle θ_{23}, which determines the mixing between ν_μ and ν_τ neutrinos, still remains to be determined precisely. If the mixing is maximal, the ν_3 eigenstate is a perfect mix of ν_μ and ν_τ. Otherwise, θ_{23} might not be exactly $45°$ and could fall into the first or second octant; in this case, one component carries more weight than the other.
Knowing this value with precision would yield higher resolution in long-baseline appearance experiments, for example in the $\nu_\mu \rightarrow \nu_e$ transition, which is an essential requirement for unambiguously measuring CP symmetry violation and resolving the mass hierarchy.

For this purpose, an even more important role is played by the yet-unknown sign of the mass squared difference Δm^2_{31}. This allows to distinguish between two different mass hierarchy configurations:

- Normal Ordering (NO): $m_1 < m_2 < m_3$
- Inverted Ordering (IO): $m_3 < m_1 < m_2$

The drawback is that the vacuum oscillations discussed so far do not allow sensitivity to the sign of Δm^2_{31}, as they depend solely on its absolute value.
Fortunately, flavor oscillations in matter could be an essential turning point to resolve this question, as the oscillation probabilities partially change their analytical expression, becoming sensitive to the sign of the mass squared difference.

During their propagation in matter, neutrinos can interact with leptons of the same flavor via charged-current interactions, exchanging a virtual W boson. This type of interaction introduces an additional potential term for the ν_e neutrino into the Hamiltonian matrix, which translates into an "effective" squared mass contribution[23]:

$$A = 2\sqrt{2} G_F N_e E \tag{1.21}$$

where G_F is the Fermi constant and N_e is the electron number density of the matter traversed by the neutrinos.

The equation describing the evolution of the flavor state in matter also changes, and consequently, the oscillation probability formula. In an effective two-flavor approximation, this is known as the Mikheyev–Smirnov–Wolfenstein (MSW) effect. Within the new equation, two new parameters appear, θ_M and λ_ν^M, driven by the generic vacuum parameters θ and Δm^2[34]:

$$P^M_{\nu_e \to \nu_e} = 1 - \sin^2 2\theta_M \sin^2\left(\frac{\pi L}{\lambda_\nu^M}\right), \tag{1.22}$$

$$\sin 2\theta_M = \frac{s_{2\theta}}{\sqrt{\left(\frac{A}{\Delta m^2} - c_{2\theta}\right)^2 + s_{2\theta}^2}}, \tag{1.23}$$

$$\lambda_\nu^M = \frac{\lambda_\nu}{\sqrt{\left(\frac{A}{\Delta m^2} - c_{2\theta}\right)^2 + s_{2\theta}^2}}. \tag{1.24}$$

$$\tag{1.25}$$

where $c_{2\theta} = \cos(2\theta)$ and $s_{2\theta} = \sin(2\theta)$.

The most interesting fact that drew attention to matter oscillations is the resonance phenomenon that occurs when $A = \Delta m^2 \cos 2\theta$: the mixing becomes maximal, even if θ in vacuum is small. This represents an amplification of oscillation effects that occurs when a neutrino traverses layers of matter with varying density, as happens in the case of solar neutrinos.

To highlight the potential of studying neutrino oscillations in matter, let us look at the $\nu_\mu \to \nu_e$ transition probability formula through matter, in a constant density approximation, to first order:

$$\begin{aligned} P(\nu_\mu \to \nu_e) \approx{}& \sin^2\theta_{23} \sin^2 2\theta_{13} \frac{\sin^2(\Delta_{31} - aL)}{(\Delta_{31} - aL)^2} \Delta_{31}^2 + \\ &+ \sin 2\theta_{23} \sin 2\theta_{13} \sin 2\theta_{12} \frac{\sin(\Delta_{31} - aL)}{(\Delta_{31} - aL)} \Delta_{31} \frac{\sin(aL)}{(aL)} \Delta_{21} \cos(\Delta_{31} + \delta_{CP}) + \\ &+ \cos^2\theta_{23} \sin^2 2\theta_{12} \frac{\sin^2(aL)}{(aL)^2} \Delta_{21}^2 \end{aligned} \tag{1.26}$$

where $\Delta_{ij} \equiv \Delta m^2_{ij} L/4E_\nu$, $a = G_F N_e/\sqrt{2}$, G_F is the Fermi constant, N_e is the electron number density in the Earth, L is the baseline in km, and E_ν is the neutrino energy in GeV. Although the formula appears very complicated, two significant aspects should be noted:

- Both the MSW effect (namely the parameter a) and δ_{CP} cause a particle-antiparticle

asymmetry, meaning they change sign when passing from the neutrino oscillation probability to that of antineutrinos ($\bar{\nu}_\mu \rightarrow \bar{\nu}_e$).

- The MSW effect introduces a sensitivity to the Δm^2_{31} parameter, which is a turning point for definitively establishing the neutrino mass ordering.[6]

In the energy range of a few GeV, the asymmetry increases with the baseline because neutrinos traverse a greater amount of matter and have more opportunities to interact; therefore, long-baseline experiments are preferred for investigating this effect.
As illustrated in Figure 1.7, when the resonance phenomenon occurs with increasing matter density (and thus an increasing number of electrons encountered), the composition of the bars representing the neutrino flavor mixing for each mass eigenstate changes drastically depending on whether the hierarchy is NH or IH.

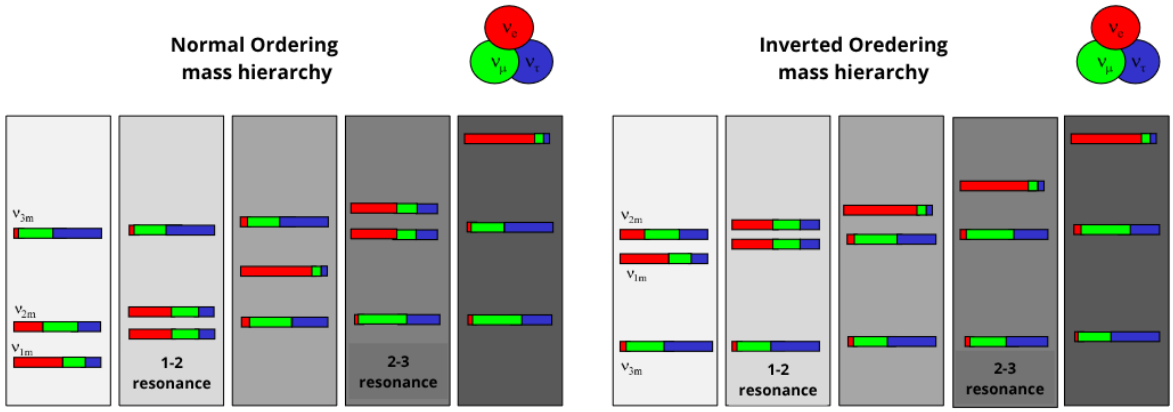


Figure 1.7: Dependence of the neutrino mass and flavor spectrum on matter density, comparing the normal mass hierarchy (left panel) to the inverted mass hierarchy (right panel). Matter density increases progressively from left to right across the panels, starting from the vacuum state on the far left. Each horizontal level represents an effective mass eigenstate in matter ($\nu_{1m}, \nu_{2m}, \nu_{3m}$), with the colored bars indicating their flavor composition: red for electron flavor (ν_e), green for muon flavor (ν_μ), and blue for tau flavor (ν_τ). The intermediate panels highlight the regions corresponding to the 1-2 and 1-3 MSW resonances [7].

[6]This matter-induced asymmetry arises because the Earth is composed entirely of ordinary matter, containing an abundance of electrons and virtually no positrons. Consequently, only electron neutrinos (ν_e) and antineutrinos ($\bar{\nu}_e$) experience forward coherent scattering via charged-current interactions with these ambient electrons, generating an effective potential with opposite signs for matter and antimatter.

1.4 Open Problems in Neutrino Physics

Before delving into the specifics of the DUNE experiment in the upcoming chapters, for the sake of completeness, it is fitting to conclude this chapter about neutrino physics, and about the experiments that have expanded our knowledge in this field, by briefly summarizing three additional open questions regarding these particles. These open questions represent the objectives for future experiments and have not yet been discussed. The three-flavor oscillation framework successfully describes the vast majority of experimental data, pointing toward physics beyond the Standard Model[35][26].

Future facilities aim to shed light on the Absolute Mass Scale, to which oscillation phenomena are insensitive. The most stringent bounds come from cosmological observations (Planck satellite) and direct kinematic measurements. The KATRIN experiment[36], investigating tritium beta decay, has set an upper limit on the effective electron antineutrino mass of $m_\beta < 0.8$ eV.

The possibility of the Majorana Nature of Neutrinos arises from the fact that neutrinos are the only elementary fermions that are electrically neutral; if this were proven, it would mean that they are their own antiparticles. Confirming this Majorana nature would provide a natural explanation for their extraordinarily small masses via the see-saw mechanism and open a pathway to explain the universe's matter-antimatter asymmetry through leptogenesis. This hypothesis is primarily tested by searching for neutrinoless double beta decay ($0\nu\beta\beta$), an extremely rare hypothetical nuclear transition.

Finally, several anomalies observed in short-baseline accelerator and reactor experiments (such as LSND[37] and MiniBooNE[38]) hint at flavor transitions driven by a mass splitting $\Delta m^2 \sim 1$ eV^2. This is incompatible with the three-flavor paradigm and suggests the existence of a fourth, "sterile" neutrino. Such a particle would not participate in Standard Model weak interactions but would mix with the active flavors .

Chapter 2

Deep Underground Neutrino Experiment (DUNE)

Following the introduction of the fundamental concepts of neutrino physics and the unresolved questions in the previous chapter, the necessity to develop new experiments capable of obtaining the long-sought physical results becomes evident. Although there are currently numerous ongoing projects, this thesis will specifically focus on the DUNE (Deep Underground Neutrino Experiment) project. DUNE represents a massive international effort, bringing together 1548 collaborators and 222 institutions from 40 different countries, including CERN.

The international DUNE experiment belongs to the next generation of long-baseline neutrino experiments.
Hosted by the U.S. Department of Energy's Fermilab, the DUNE facility will feature two main detectors sites. A near detector will be situated on-site at Fermilab in Illinois, while a far detector will be located approximately 1.5 km underground at the Sanford Underground Research Facility (SURF) in South Dakota, USA, at a baseline distance of 1300 km from the neutrino source, as shown in fig. 2.1. Being located 1.5 km underground shields the far detector from the background noise of cosmic rays, reducing the cosmic muon flux by six orders of magnitude.

Since a massive target is essential to achieve a sufficient event rate in neutrino oscillation experiments due to their extraordinarily small interaction cross-sections, the far detector will consist of a very large, modular liquid argon time-projection chamber (LArTPC) with a total mass of nearly 70 kt, providing a fiducial mass of at least 40 kt [39][40].

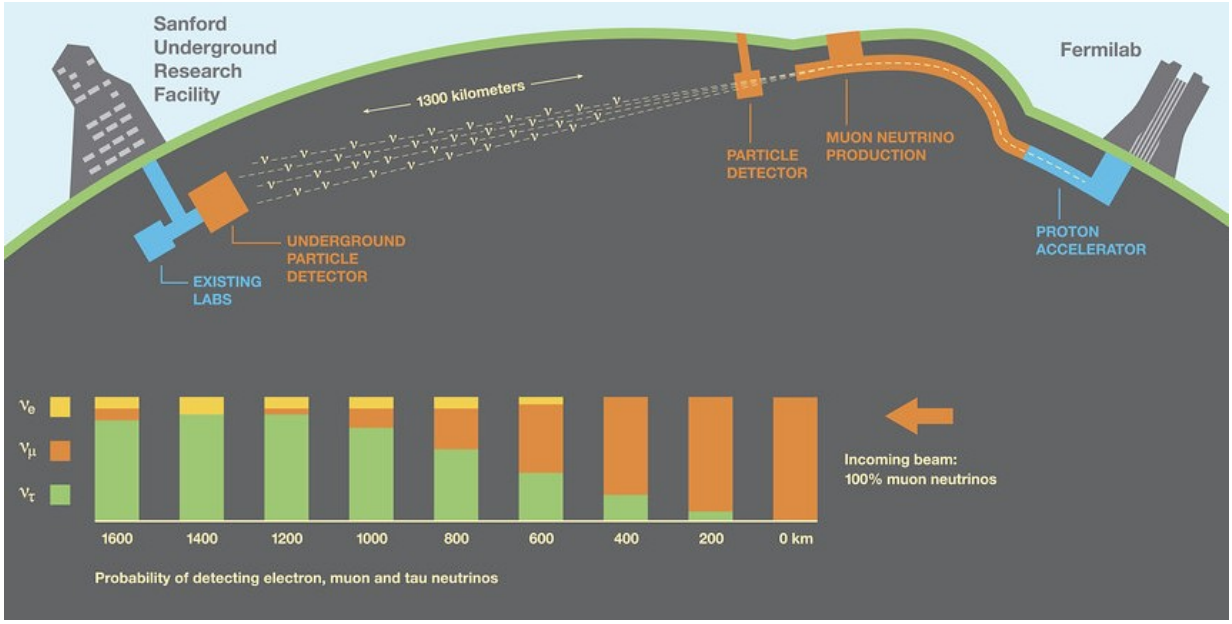


Figure 2.1: "Schematic overview of the LBNF/DUNE project, showing the 1300 km path of the neutrino beam through the Earth from Fermilab (Illinois) to SURF (South Dakota). The bottom panel illustrates the flavor oscillation probability of the initial muon neutrino beam into electron and tau neutrinos as a function of distance. Image courtesy of Fermilab / DUNE Collaboration.

The DUNE project represents an innovative approach to neutrino physics experiments, as it offers unique features and applies exciting technologies that could lead to the desired results[41][42]. For example, DUNE has access to a very intense wide-band neutrino beam compared with those used in other experiments, with energies ranging from 0.5 to 8 GeV. This configuration enables the experiment to observe both the first (around 2.5 GeV) and second (around 0.8 GeV) oscillation maxima simultaneously (see Fig. 2.2).
The ability to observe this type of event across a wide energy range could be exploited to overcome the parameter degeneracy discussed at length in the previous section; a major achievement would be to successfully distinguish the effects of CP violation from those of matter in the oscillation probability, which would provide a useful clue for determining the mass order of neutrinos.
In addition, its underground location provides a low cosmic-ray background, transforming DUNE into a multi-purpose observatory. It is capable of studying a broad range of non-accelerator phenomena, such as atmospheric neutrino oscillations, the potential sub-GeV neutrino flux originating from a galactic core-collapse supernova, and beyond-Standard-Model processes like nucleon decay.

To achieve a large detection volume, many current experiments in neutrino physics use water or ice, which are naturally occurring substances, by exploiting the Cherenkov effect of ultra-relativistic particles; IceCube and KM3net[43] are examples of detectors that have already made a significant contribution to our understanding of neutrino physics.
The DUNE project aims to utilise LArTPC (Liquid Argon Time-Projection Chamber) technology on a large scale, distributed across four 17-kilotonne modules.
The use of LArTPC enables a three-dimensional, image-like reconstruction of events and a calorimetric measurement of energy, making it possible to track particles and separate signals from background noise much more effectively.
The benefits of this technology have already been demonstrated by other experiments such as ICARUS[44] and MicroBooNE[45]; the DUNE project therefore aims to achieve the same level of precision, but for the first time on a much larger scale.
In addition, since liquid argon is a scintillator, advanced photon detection systems are integrated to capture the scintillation light of liqud Argon at 128 nm. These modules utilize SiPMs to efficiently detect the photon signal within the LArTPC volume.
These choices could prove decisive in achieving significant results, but they also present a challenge for the development and practical construction of the detectors in every respect.

2.1 Physics's goal of the detector

This section explores the physics goals of the DUNE project in detail, before moving on to describe its main components. Many of these objectives aim to answer the unresolved questions discussed in the previous chapter, primarily through the phenomenon of neutrino oscillations.

Central to this is the role of the δ_{CP} phase in studying Charge-Parity (CP) symmetry violation within the leptonic sector; as previously mentioned, discovering this violation could provide a crucial explanation for the matter-antimatter asymmetry observed in the universe. To investigate this phenomenon, DUNE aims to measure the oscillation probability of muon neutrinos (ν_μ)—which predominantly make up the initial beam—into electron neutrinos (ν_e), and similarly for their corresponding antiparticles.

Thanks to its wide-band beam and long baseline, DUNE will have simultaneous access to both the first and second oscillation maxima, fig 2.2. As explained in the previous

chapter, this configuration breaks parameter degeneracies, disentangling the effects induced by δ_{CP} from matter effects in the oscillation probabilities.
Extremely high resolution is essential to achieve the desired result. In particular, the LArTPC detector must precisely identify the electromagnetic showers generated by electron neutrinos after oscillation, distinguishing them from background signals.
Under the most favorable scenario, it is projected that with 3.5 years of data taking, DUNE will reach a sensitivity greater than 3σ for the discovery of CP violation, leading in the long term to the ability to resolve the possible values assumed by this parameter.

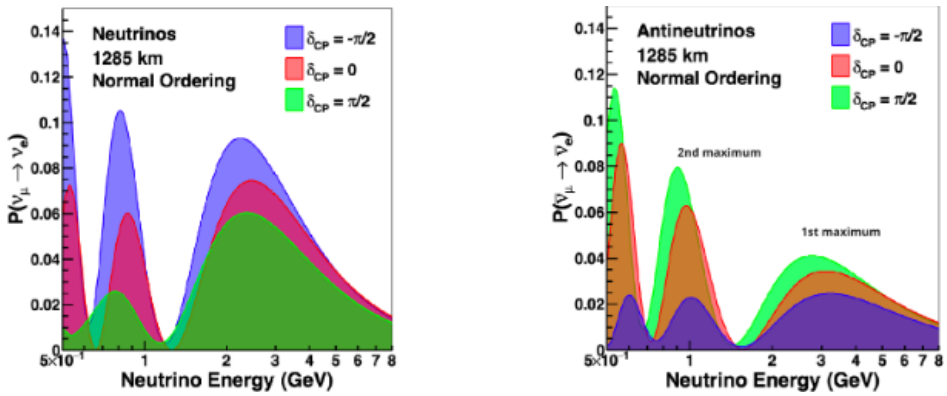


Figure 2.2: Oscillation probabilities $P(\nu_\mu \to \nu_e)$ (left) and $P(\bar{\nu}_\mu \to \bar{\nu}_e)$ (right) as a function of neutrino energy at the DUNE 1300 km baseline. The curves are shown for three different values of the δ_{CP} phase under the Normal Ordering hypothesis. The wide-band beam configuration allows the experiment to simultaneously access both the first and second oscillation maxima, which is crucial for disentangling CP violation from matter effects[46].

Another crucial point in the DUNE collaboration's program is determining the neutrino mass hierarchy, meaning establishing whether the ν_3 mass eigenstate is heavier or lighter than the other two eigenstates.
As seen in the previous chapter, the MSW matter effect is utilized to achieve this goal, taking advantage of the long distance the neutrinos travel between the two detectors to attain a statistical significance of at least 5σ.
LArTPC technology proves essential for measuring the appearance energy spectrum of electron neutrinos (ν_e) with greater precision than previous experiments, spanning a range from 500 MeV to several GeV. DUNE collaboration projections indicate that detector performance could reach a 5σ statistical sensitivity for this discovery, regardless of the true value of the δ_{CP} phase, within 5 years of data taking.

Since atmospheric neutrinos also experience strong resonances due to their journey through the Earth's crust, they could be used in a complementary manner for this same purpose, thereby increasing the experiment's sensitivity. In this case, a technology capable of efficiently distinguishing between neutrino and antineutrino interactions is required; since the DUNE Far Detector is not magnetized, this statistical separation relies entirely on the high-resolution topological and calorimetric capabilities of the LArTPC to analyze the final state [46].
The capabilities of the DUNE project also stem from its potential to function as an astrophysical observatory for sudden events, such as the neutrinos emitted during a core-collapse supernova within our galaxy. The neutrino flux in this scenario is on the order of MeV and crosses the detector's active volume over a timescale of tens of seconds.

DUNE stands out for its sensitivity to the electron neutrino component, unlike the widely used Cherenkov or scintillation detectors, which are primarily sensitive to electron antineutrinos. Liquid argon interacts with ν_e to produce a well-defined electron track. As introduced in the previous chapter, this result allows for a broader understanding of the neutronization phase.

2.2 The LBNF Neutrino Beam

The Long-Baseline Neutrino Facility (LBNF) at Fermilab is responsible for delivering the world's most intense neutrino beam to the DUNE detectors. The beam is generated using protons from the Fermilab Main Injector, shown in Fig. 2.3, benefiting from the Proton Improvement Plan II (PIP-II) upgrade[47]. PIP-II is a new leading-edge, superconducting linear proton accelerator under construction at Fermilab. This upgrade is essential to deliver the unprecedented proton beam power of 1.0 to 1.2 MW (designed to be upgradeable to over 2.0 MW in Phase II), with proton energies ranging from 60 to 120 GeV, required to generate the intense neutrino flux for DUNE.

The process of generating the neutrino beam involves several distinct steps. It begins within the Fermilab accelerator complex, where H^- ions are produced and accelerated by the new PIP-II superconducting linear accelerator. After passing through a foil that strips their electrons to yield bare protons, they are sequentially accelerated by the Booster Ring and the Main Injector to a final energy between 60 and 120 GeV.
This high-energy primary proton beam then collides with a 2.2 m long, 16 mm diameter

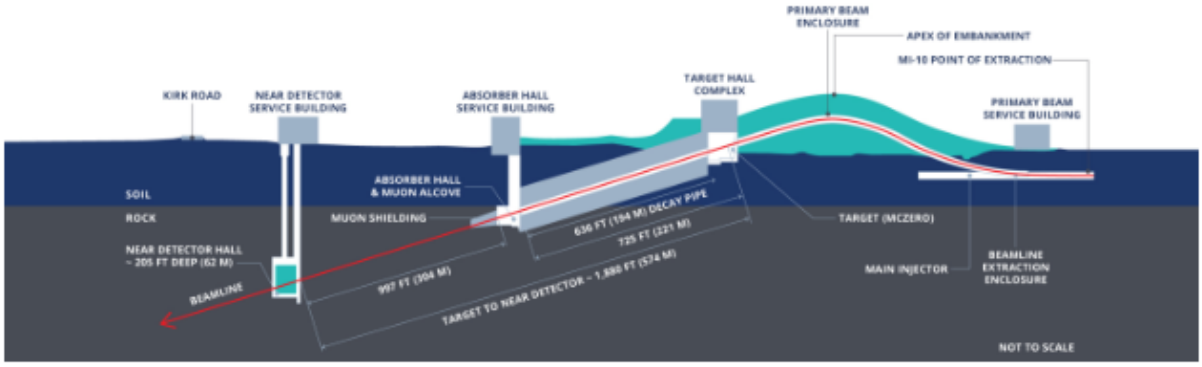


Figure 2.3: Schematic profile of the Long-Baseline Neutrino Facility (LBNF) beamline at Fermilab. The diagram illustrates the primary proton beam extraction, the target hall, and the 194 m long decay pipe where the neutrino beam is generated. Downstream of the hadron absorber, the beam travels through the rock to the Near Detector hall, which is situated 62 m underground at a distance of 574 m from the target. *Image courtesy of Fermilab / DUNE Collaboration.*

cylindrical graphite target. This intense interaction produces a copious secondary beam of charged hadrons, primarily pions and kaons.
Because these secondary particles emerge from the target scattering at various angles, they must be aligned to maximize the final neutrino flux directed toward the detectors. To achieve this, the hadrons pass through a focusing system consisting of three magnetic horns operated with 300 kA currents. These horns act as powerful magnetic lenses, capturing the diverging charged hadrons and focusing them into a highly collimated, forward-moving beam.

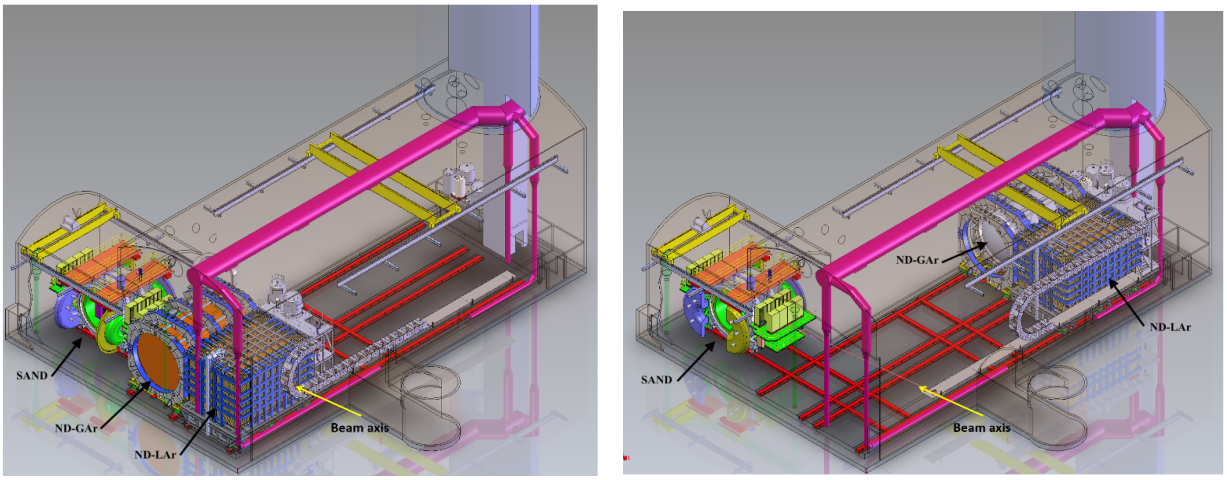
Following the focusing stage, the hadrons enter a 194 m long, helium-filled decay pipe where they decay to produce the intense neutrino flux. Any remaining hadrons and uninteracted protons are subsequently stopped by a hadron absorber located at the end of the decay region.

LBNF beamline can reversing the polarity of the magnetic horns, the facility can select the charge of the focused hadrons. This allows the beamline to operate in two distinct configurations: a forward-horn current (FHC) mode, which produces a predominantly muon-neutrino (ν_μ) beam, and a reverse-horn current (RHC) mode, which produces a predominantly muon-antineutrino ($\bar{\nu}_\mu$) beam. The resulting wide-band neutrino energy spectrum spans from roughly 0.5 to 8 GeV, peaking around 2.5 GeV, which is perfectly tuned to cover the first and second oscillation maxima at the DUNE baseline. Furthermore,

understanding the small intrinsic electron-flavor contamination (∼1%) in both modes is crucial, as it represents the primary background for the ν_e appearance measurement. This dual capability is crucial for the DUNE physics program for observing CP violation in the neutrino sector.

2.3 The DUNE Near Detector Complex

The Near Detector (ND) complex plays a key role in achieving the physical goals of the DUNE experiment. This detector is located at Fermilab, 570 m from the target and 66 m underground, and will be exposed to the extremely intense neutrino flux described above. The main purpose of this system is to measure the reconstructed energy spectrum and the composition of the neutrino beam before oscillations occur. By comparing these data with measurements taken by the far detector, it will be possible to calculate the oscillation probabilities and drastically reduce the systematic uncertainties associated with the neutrino-nucleus interaction cross-sections.
To achieve this aim, the Phase I configuration of the Near Detector comprises three main detectors and a handling system, located as shwon in Fig. 2.4.



(a) On-axis configuration (b) Off-axis configuration (DUNE-PRISM)

Figure 2.4: Schematic overview of the DUNE Near Detector complex showing the movable components (ND-LAr and ND-GAr) positioned directly on the beam axis (left) and moved transversely off-axis (right) as part of the DUNE-PRISM system. SAND remains fixed on-axis in both configurations [48].

The ND-LAr is the central detector, a modular liquid argon Time-Projection Chamber (LArTPC) comprising 35 modules, with a total mass of 150 tonnes, equipped with an inno-

vative pixel charge readout system. As it uses the same target material and the same basic technology as the Far Detector (the detailed operation of which will be explored in the next section), it is possible to analyse the data from neutrino-argon interactions directly, thereby eliminating a large proportion of systematic errors[48].

The TMS (The Muon Spectrometer) is responsible for tracking the outgoing muons escaping from the ND-LAr, accurately measuring their momentum and charge.
Since muons with energies greater than 0.7 GeV/c produced in the interactions are not completely contained within the liquid argon volume of the ND-LAr, a magnetised spectrometer consisting of alternating layers of absorber material and active detection planes is positioned downstream.
The magnetic field will be approximately between 1 and 1.5 T. In a future configuration, the TMS will be replaced by ND-GAr, a high-pressure argon gas detector surrounded by an electromagnetic calorimeter.

One of the most innovative features of this complex is the DUNE-PRISM technology[49]. This system allows the ND-LAr and TMS to be moved laterally, shifting them off-axis by up to 28.5 m. As the detectors move off-axis,a schematic is shown in Fig. 2.4.
the neutrino energy spectrum narrows and shifts towards lower energies, providing a nearly monochromatic beam. This technique enables the measurement of cross-sections at different energies whilst minimising their dependence on theoretical models, a key element for DUNE's entire physics programme.
At present, a prototyping phase is ongoing at various international institutions to finalise the design. In addition to the extraction and consolidation of components for SAND and TMS, the ND-LAr demonstrators are also noted: a full-scale module operated in Bern recorded 70 million cosmic events, whilst at Fermilab a 2×2 demonstrator successfully collected 4.5 days' worth of data directly from the NuMI beam in the summer of 2024.

2.4 The DUNE Far Detector

The DUNE Far Detector (FD) will be installed at a depth of approximately 1.5 km at the Sanford Underground Research Facility (SURF) and will consist of four main modules. Each module will utilise liquid argon Time-Projection Chamber (LArTPC) technology.
The first two modules to be installed are LArTPCs with different design implementations: the Horizontal Drift (HD) and the Vertical Drift (VD). Although both are housed in

cryostats, each containing a huge mass of liquid argon, they differ primarily in the direction of the electrons' drift motion.

2.4.1 LArTPC Technology

Originally proposed in 1977 by Carlo Rubbia[50], the TPC is a detector capable of providing direct information on the tracks left by charged particles; designed to produce high-quality three-dimensional images, it represents an evolution of the older bubble chamber.

Charged particles passing through the active volume ionise the argon molecules, produc-

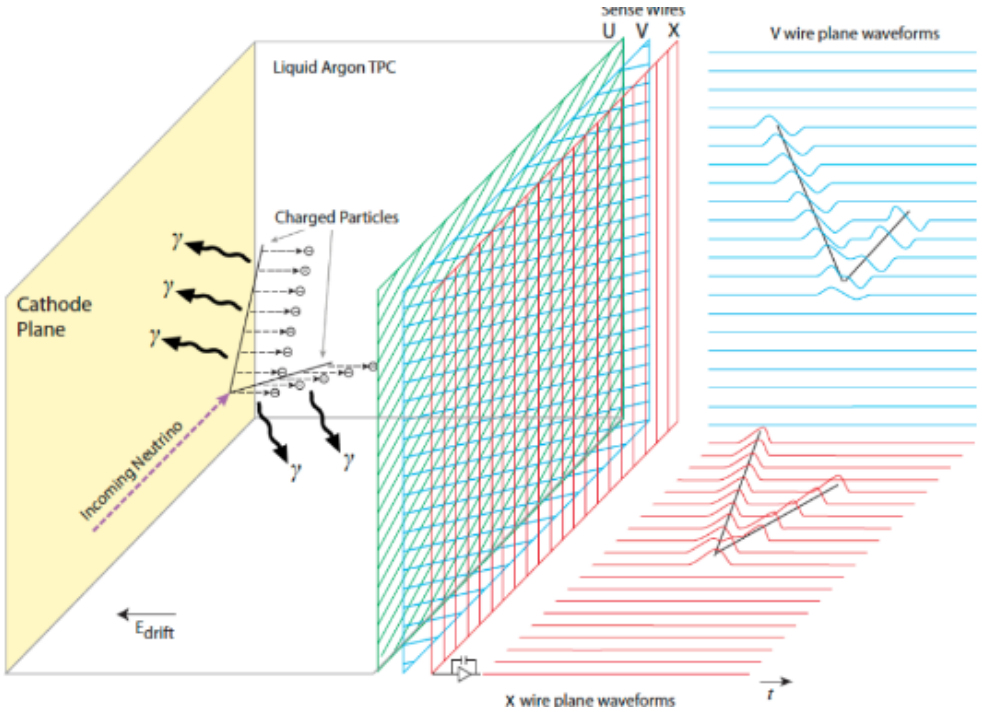


Figure 2.5: Illustration of the operating principle of a Liquid Argon Time Projection Chamber (LArTPC). An incoming neutrino interacts with the argon nucleus, producing charged particles that ionize the medium and generate scintillation light (γ). A uniform electric field (E_{drift}) forces the ionization electrons to drift towards the anode sense wires. Taken from [51].

ing electrons and rapid scintillation light.

The application of a uniform electric field causes the ionisation electrons to separate from the ionised atoms and drift towards the anode. Scintillation light is detected by photodetectors. The Photon Detection System in the cryostat therefore provides the absolute time reference for the event.

By comparing the time t_0 provided by the arrival of the scintillation light with the moment

when the much slower ionisation electrons reach the anode, the system is able to calculate the particle's position, which is essential for the three-dimensional reconstruction of the event.

When the TPC technique is implemented using liquid argon (LAr), the apparatus is known as a Liquid Argon Time-Projection Chamber (LArTPC).
The use of liquid argon is justified by several factors. Firstly, it is a noble gas and therefore offers high electron mobility; amongst noble liquids, argon has a sufficiently high density, abundant scintillation light and a long radiation path, which minimises secondary interactions. In this configuration, liquid argon acts simultaneously as both the target material for neutrino interactions and the active detection medium.
A minimum ionising particle produces approximately 60,000 ionisation electrons per centimetre in liquid argon; this allows for a good 2D reconstruction of the event on the anode plane, after which, by combining the signals recorded on different planes, the interaction can be reconstructed in three dimensions, with the aim of obtaining millimeter-level resolution.

There are two important aspects of the technology that could cause problems with detection. First, the electrons produced by ionization run the risk of being captured during their drift by any contaminants present in the liquid; therefore, one point to keep in mind is the purity level of the argon, which must ensure that the electron survives for approximately 3 ms.
Furthermore, within the liquid, the charge signal does not undergo amplification; for this reason, the electronics responsible for reading the signal must be designed to minimize the signal-to-noise ratio as much as possible.

In the DUNE far detector LArTPC ionisation signal is detected when the drift electrons reach the anode detection planes, guided by a uniform electric field of approximately 500 V/cm, as shown in Fig. 2.5. This choice represents a compromise compared with a high electric field, which would certainly increase the drift velocity, reducing any losses due to argon impurities, but at the same time would suppress electron-ion recombination, an effect that produces a significant proportion of the scintillation light. At 500 V/cm, the drift velocity is 1.6 mm/μs.

The scintillation signal, on the other hand, takes the form of ultraviolet light resulting from the de-excitation of excited argon molecules, emitted at a wavelength of 128 nm. This

process will be described in more detail later in chapter 3, when we discuss the PDS. Liquid argon is an excellent scintillator and is transparent to its own light, emitting approximately 40,000 photons per MeV of deposited energy at a wavelength of 128 nm. The scintillation photons provide the absolute time reference (t_0) of the event, relative to which the arrival time of the electrons is then calculated. Furthermore, the scintillation light contributes to the calorimetric reconstruction of the event and is essential for triggering low-energy events

2.4.2 The Horizontal Drift Far Detector

The Horizontal Drift (HD) was the first module to be designed with ionisation electrons drift horizontally. The detector features an active volume of $12 \times 14 \times 58$ $\mathbf{m}^3$, contained within a massive cryostat measuring $15 \times 14 \times 62$ $\mathbf{m}^3$. The active volume is divided into four drift regions separated by alternating cathode and anode planes as shown in Fig. 2.6. The entire module is contained within a field cage and, under the influence of an electric field of approximately 500 V/cm, generated by a cathode set at 180 kV, situated 3.6 m away from the anode.

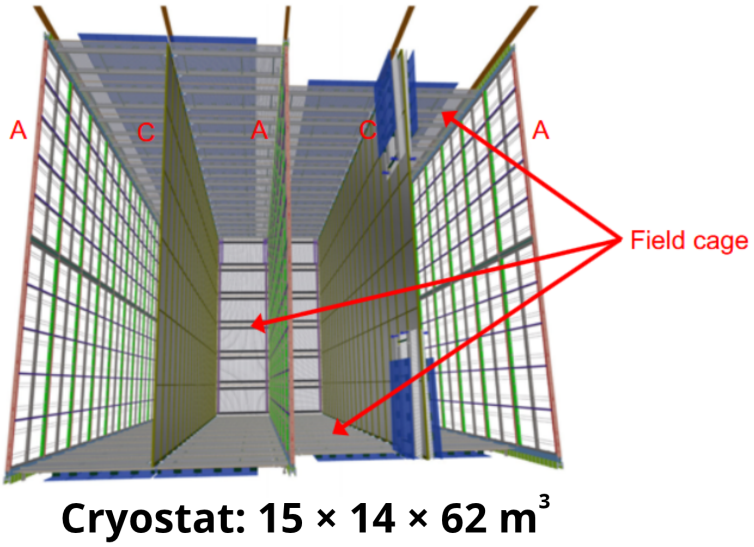


Figure 2.6: Schematic view of the DUNE Horizontal Drift (HD) module. The time projection chamber is segmented by alternating cathode and anode planes generating four drift volumes. Electrons are drifted towards the anode planes where they are read out. Photon detector modules are embedded in the anode planes, and the entire active volume is enclosed by the field cage.

The complex grid-like structure of anodic planes that characterises this module consists

of steel frames entirely covered by thin copper-beryllium wires that are sensitive to the passage of electrons, known as Anode Plane Assemblies (APA). The wires are arranged into 3 layers, the first two layers are induction layers and they have wires arranged at an angle of $\pm 35.7°$ to the vertical. The third layer, the collection layer, has vertical wires; signal-reading electronics, known as 'Cold Electronics' because they are completely immersed in LAr and operate at cryogenic temperatures, are installed on the edges of the APAs.
Note that the signal digitization and readout circuits are installed at the top of the APAs to prevent any loss of the signal from the electron charges, which is quite weak since it does not undergo amplification; however, this choice necessitates the development of specialized electronics.

The latest version of the HD module prototype (ProtoDUNE-HD) was built and operated at CERN between 2020 and 2024, and was tested using both cosmic rays and charged particle beams from the accelerator. The results showed a mean lifetime for electrons sufficient to guarantee a signal that can be detected without difficulty, indicating the purity of the LAr and the proper functioning of the electronic devices.
As the wires making up the anode planes are completely transparent to ultraviolet scintillation light, it is possible to install photodetectors within the APAs. The PD modules used are X-ARAPUCA, which will be described in detail in Chapter 3. They are positioned both near the outer walls and on both sides of the central plane, ensuring effective coverage of the volume.

2.4.3 The Vertical Drift Far Detector

The second module of the FD is called Vertical Drift (VD), because, differently from the HD, the electron's drift motion occurs in a vertical direction respect to the ground.
The VD contains only two drift volumes, each 6.5 m high; in fact, the cathode plane is positioned at the centre of the cryostat, which means that, depending on whether the particle passes through the upper or lower zone, it will drift upwards or downwards. Such a long drift distance is made possible by advances in LAr purification: removing impurities increases the electron lifetime to approximately 10 ms, ensuring that good signals reach the anodes.

The signal readout on the anode planes is known as Charge-Readout Planes (CRP) assembly, and differs from that of the APAs found in HD; in fact, anodes are made with

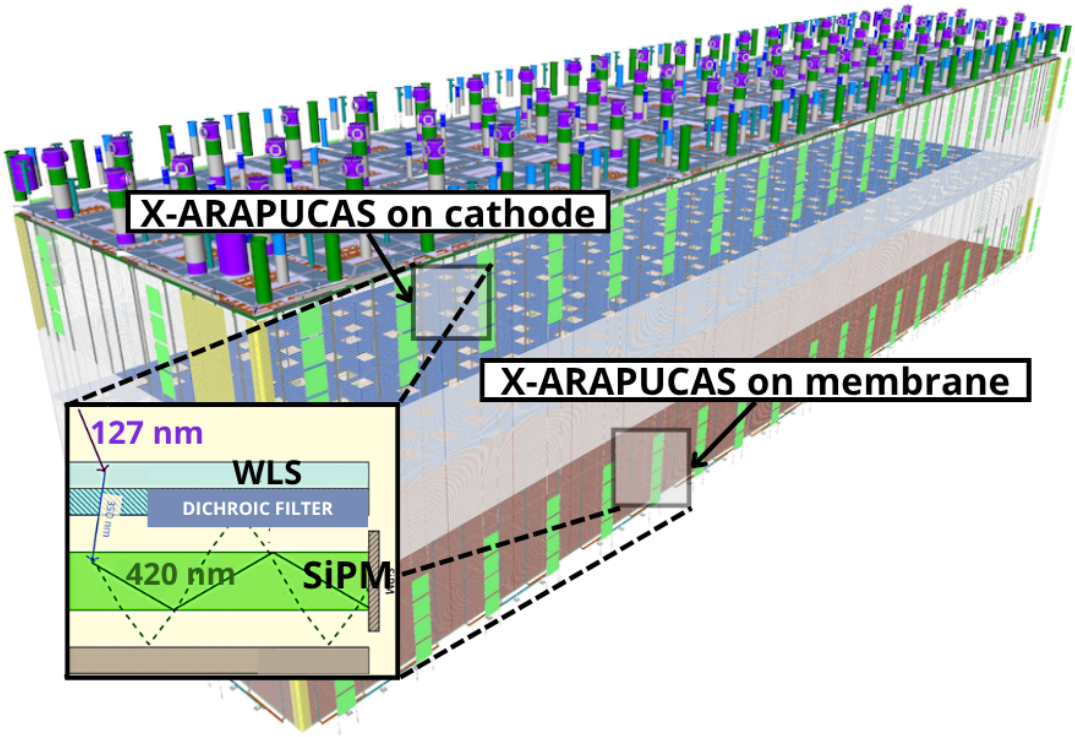


Figure 2.7: Overview of the DUNE Vertical Drift (VD) module illustrating the placement of the Photon Detection System. The inset details the X-ARAPUCA working principle: 127 nm LAr scintillation photons are shifted to 350 nm by a wavelength shifter, pass through a dichroic filter, and are further shifted to 420 nm, remaining trapped by total internal reflection until detected by the SiPMs.

perforated printed circuit boards (PCBs).
These copper readout strips are arranged in two induction layers and one collection layer, allowing the combined signals to provide a view of the event from three independent perspectives.

Each CRP consists of two overlapping PCBs measuring 3.0 m $\times$ 3.375 m, connected to one another by a frame. Each anode plane contains 80 of these structures. The side of the CRP facing the cathode serves to shield the structure from unexpected charges.
On the other three sides are the induction strips, which are transparent to drift electrons, and the conduction strips, on the surface furthest from the cathode. To increase transparency to electrons, the holes are arranged in perfect alignment with one another, whilst the fact that the strips on each surface have different orientations, as in the HD, necessary to achieve 3D reconstruction.

The upper and lower sections of the VD will utilise different readout electronics. The

bottom electronics are identical to the HD electronics and will be completely inaccessible once the cryostat is filled. In contrast, the top electronics consist of cryogenic boards located in dedicated chimneys on the roof of the cryostat. This specific design choice allows them to be accessed, replaced, or fixed if needed during the operation of the experiment.

X-ARAPUCA modules are also planned for the VD, although their positioning is less practical than in the case of the HD. In this case, the anode planes are opaque PCBs and the detectors cannot be installed behind them.
To increase light yield and improve uniformity, it was decided to position the X-ARAPUCA modules at the cathode as well, which is subject to a potential of –300 kV.
This detail is crucial as it requires the development of a power supply and electronic readout system that does not use conductive materials, and has led to the implementation of Power-over-Fibre (PoF) and Signal-over-Fibre (SoF) technologies, which use optical fibres to transmit signals into and out of the cryostat.
These systems will be described in greater detail in the following chapters.

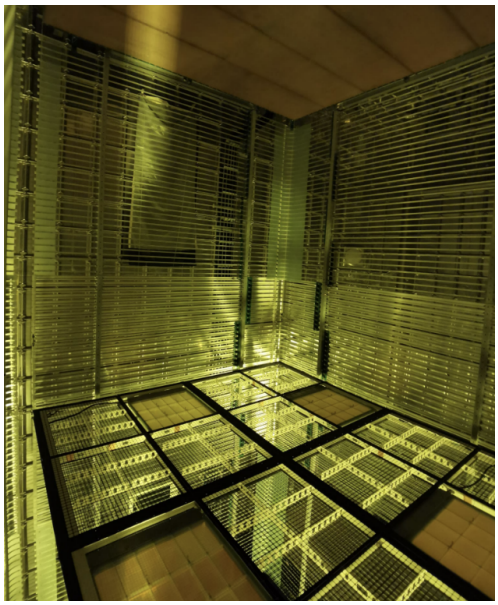


Figure 2.8: Inside view of the ProtoDUNE-VD detector during assembly. The image highlights the distinctive ”window blind” design of its field cage, which utilizes flat, horizontal metallic slats to shape the vertical electric field. The floor reveals a grid-like framework designed to support the bottom Charge Readout Planes (CRPs) and optical modules.

2.4.4 ProtoDUNE

Before proceeding with the actual construction of the Far Detector modules, the DUNE collaboration set up a prototyping programme at CERN's Neutrino Platform. The prototypes are smaller than the final modules but use full-scale components with the specifications envisaged for the final design, so as to test their functionality.
The program started in 2018 and is currently ongoing. It uses two kiloton-scale cryostats, called NP02 and NP04, which have hosted a total of four detector configurations so far, collecting data from charged-particle beams, calibration sources, and cosmic rays.
These prototypes represent the largest LArTPCs ever built and operated, successfully providing a demonstration of both the HD and VD technologies at the kiloton scale[52][53]. The successful operation of these modules and their integrated components represents the crucial validation step before the full-scale Far Detector construction.

Chapter 3

DUNE Vertical Drift Photodetection System

In the previous chapter, the DUNE project was presented through a comprehensive overview of its various components; this chapter will now examine in greater detail the design of the photon detection system (PDS), focus to the work I was able to carry out during my internship at the APC laboratory in Paris.
As explained in Chapter 2 the PDS serves to detect the instantaneous light signal from LAr scintillation. An important challenge of this detection system is that the ultraviolet scintillation light produced by interactions between charged particles and liquid argon is not trivial to detect, especially with detectors operating at cryogenic temperatures (87 K). This requires either the use of more complicated UV-sensitive detectors, or more common visible-light detectors combined with wavelength shifters (WLS).

The following sections will briefly describe the processes that produce LAr scintillation light, then focus on the mechanism by which the X–ARAPUCA photon collectors convert the VUV light emitted by LAr into the visible range so that it can be detected by the SiPMs, and finally, the PDS technology on the cathode, which utilises optical fibres to provide a practical solution to the problem of high voltage for conductive materials.

3.1 LAr Scintillation Light Production

When a charged particle passes through the volume of LAr, two distinct processes may occur, depending on the energy released by the incident particle. If the energy is sufficiently

high, an electron is released, free to begin its drift towards the anode or to recombine with LAr. In fact, if the energy is not sufficient, argon excitons Ar^* are produced instead of Ar^+ ions; both combine with LAr atoms, undergoing direct excitation and recombination processes, a scheme of the processes is shown in fig. 3.1.
Ar_2^+ molecular excitons directly emit a scintillation photon at a typical wavelength of 127 nm. Molecular ions Ar_2^+, on the other hand, emit the scintillation photon only after recombining with an electron and other LAr atoms. Although the sequence of reactions is much longer, the scintillation photon always originates from the same decay:

$$Ar_2^*(^{1,3}\Sigma_u^+) \rightarrow 2Ar + \gamma_{127\ \mathrm{nm}} \tag{3.1}$$

Depending on the state of Ar_2^+, the decay occurs with two different time constants: approximately 6 ns in the case of the singlet state $^1\Sigma_u^+$ or 1.5 μs in the case of the triplet state $^3\Sigma_u^+$. In the signal detected by the photodetectors, the two components are perfectly distinguishable[54, 55].
Pure liquid argon as an efficient scintillator emits approximately 40 photons/keV. However, in the environment of a LArTPC, the application of an external electric field of 500 V/cm, the one adopted in DUNE, suppresses the electron-ion recombination process. As a result of this reduced recombination, the practical scintillation light yield decreases to approximately 24000 photons per MeV for a minimum ionizing particle (MIP).
The temporal profile of the scintillation signal is strictly determined by the relative abundance of its fast and slow components. The pulse shape depends on the type of ionizing particle and its Linear Energy Transfer,which represents the average energy deposited by the particle per unit of path length.
Because different particles deposit energy at varying densities, the ratio of singlet to triplet state de-excitation changes significantly; this makes pulse shape analysis a powerful tool for particle discrimination. Furthermore, the scintillation waveform and the timing of the slow component are influenced by the intensity of any applied external electric field, which sweeps electrons away from the recombination process [54].

The photons produced may not reach the photodetectors if the LArTPC contains contaminants; for this reason, the LAr must be sufficiently pure. Electro-negative atoms that might collide with excited argon atoms are to be avoided. It is not always easy to remove contaminants, and attempts have been made to measure their effect on the light output and to identify experimental parameters that allow the purity of the scintillator to be monitored.
Furthermore, the photons themselves may interact after being produced, before reaching

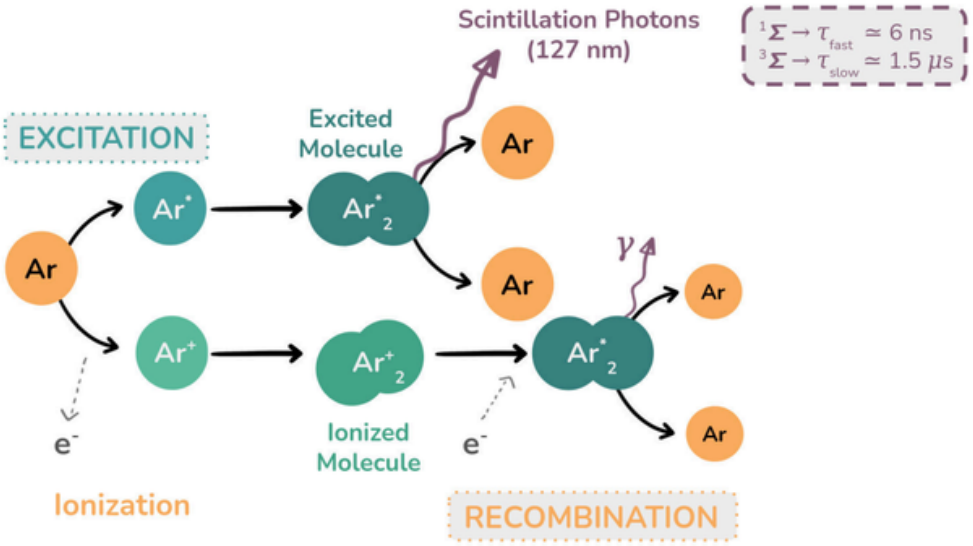


Figure 3.1: Schematic representation of the scintillation light production processes in liquid argon. The two main pathways are illustrated: direct excitation and ionization followed by recombination. Both processes lead to the formation of molecular excimers (Ar_2^*) which, upon decaying to their ground state, emit 127 nm VUV photons characterized by two time components (a fast component of ~ 6 ns and a slow component of ~ 1.5 μs).

the detector, through Rayleigh scattering, which does not alter the light intensity but increases the distance travelled and thus the probability that the light will be absorbed in the medium.
This process is characterized by the Rayleigh scattering length, which represents the mean path that a photon can travel before undergoing scattering. The estimation of this value in liquid argon is important; recent measurements[56] provide an estimation of $\lambda_{RS} \sim (99.1 \pm 2.3)$ cm, but it becomes larger when the mixture is doped with Xenon (Xe), for this reason the use of LAr doped with 10 ppm of xenon is under consideration.
The absorption of photons due to the presence of impurities such as nitrogen results in anabsorption length, defined as the distance after which the light intensity is reduced by a factor of 1/e of approximately 20 m.

3.2 The X-ARAPUCA Technology

To detect UV light from LAr, the DUNE project is promoting X-ARAPUCA technology, which, using wavelength shifters, shifts the photons into the visible spectrum so that they

can be detected by SiPMs with peak sensitivity at ~ 500 nm.

SiPMs are solid-state silicon photodetectors, composed of independent microcells known as APDs, i.e. avalanche photodiodes operating in Geiger mode. Photodiodes are characterised by a breakdown voltage[1]; when they are biased slightly above this threshold, a very intense electric field is generated in the depletion region.
If a photon is absorbed by the silicon, the first electron-hole pair is created, which, thanks to the electric field, in turn triggers a charge avalanche.
Through this mode of operation, even a single photon can generate a measurable electrical signal. In reality, the output signal from the SiPM is given by the discrete contributions of the individual APDs, which are connected in parallel. The intensity of the output signal is proportional to the flux of incident photons, as determined by the number of cells that have been activated.

SiPMs have a temporal resolution in the nanosecond range, good sensitivity and maintain robust performance even at cryogenic temperatures, such as that of the LAr (87 K). Furthermore, there is also a reduction in the dark count rate and therefore an improvement in the signal-to-noise ratio, one of the desired objectives of the PDS.

Thanks to the experience of previous experiments based on LArTPC, the choice of the optimal photodetectors for the project has fallen on SiPMs, as they are not particularly bulky and are therefore ideal given the space constraints within anodes and cathodes.
However an issue about the specific models of SiPMs chosen for this project is that they have low sensitivity to the VUV light emitted by the LAr; for this reason, they are fitted within a device designed to trap the photons propagating within the cryostat: the X-ARAPUCA.

The diagram shown in Fig. 3.2 illustrates the working principle of the X-ARAPUCA. Photons arrives to the X-ARAPUCA pass through an outer layer of PTP, the first WLS made of para-terphenyl, a coating deposited on the top side of the fused silica substrate of the dichroic filters, with an efficiency larger than 95%; at this stage, its wavelength is shifted from 128 nm to 350 nm.

[1]The breakdown voltage (V_{bd}) is the minimum reverse-bias voltage required to initiate and sustain a self-propagating charge avalanche within the depletion region.

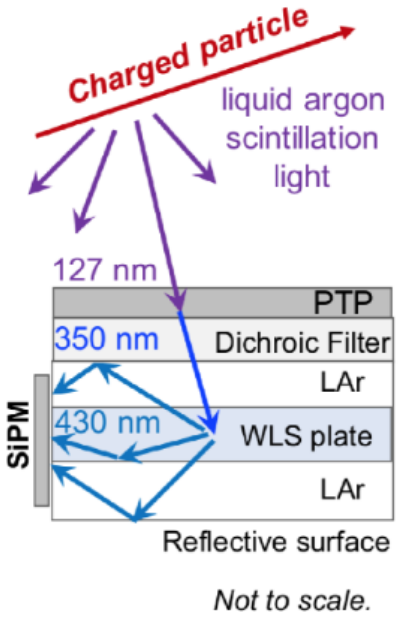


Figure 3.2: Cross-sectional schematic of an X-ARAPUCA module illustrating the multi-step wavelength-shifting and photon-trapping process

Next comes the optical trapping stage, as the photons enter the dichroic filter, the choice of fused silica is driven by its excellent low-temperature properties, making it a common optical window in cryogenic environments[39].
The filter is filled with LAr and contains a second WLS material made of tetra-phenyl butadiene (TPB), whose role is to shift the wavelength above the filter's cut-off threshold, from 350 nm to 430 nm.
This step is essential because the dichroic filter has a cut-off wavelength of 400 nm (a transmission band from 300 to 400 nm and a reflection band from 400 to 500 nm); the photon enters at its initial wavelength but afterwards cannot escape because it is within the reflection band.
Ultimately, a larger percentage of photons travel to the SiPM after the required number of reflections off the wall.

The performance of this light collector is quantified by its collection efficiency (ϵ_{coll}), defined as the ratio between the number of detected photons and the number of 128 nm incident VUV photons.
This key parameter is fundamentally determined by three main factors: the efficiency of the WLS in converting incident VUV photons into trapped visible photons, the proba-

bility that these trapped photons propagate successfully through the cavity to reach the photosensor, and the intrinsic quantum efficiency of the SiPMs to convert them into a measurable electrical signal. Recent tests on various module configurations have demonstrated an absolute detection efficiency of $(4.5 \pm 0.4)\%$ at a SiPM bias voltage of 4.5 V[57].

This architecture is designed to achieve a target photodetection efficiency of 3%. It is important to note that this implies approximately 97% of the photons arriving at the X-ARAPUCA are not detected. This substantial loss occurs because photons are re-emitted in random directions, and the dichroic filter is highly inefficient at trapping photons that hit it at non-ideal angles.
Specifically, the isotropic re-emission of photons by the PTP layer causes a fraction of them to be reflected by the dichroic filter, preventing their entry into the cavity. Furthermore, photons isotropically re-emitted within the WLS, exhibit a wide angular spread; while those exceeding the critical angle ($\theta \sim 56°$) are effectively trapped via total internal reflection, photons impinging at smaller angles can easily escape the device due to the non-ideal, angle-dependent transmittance of the dichroic filter.

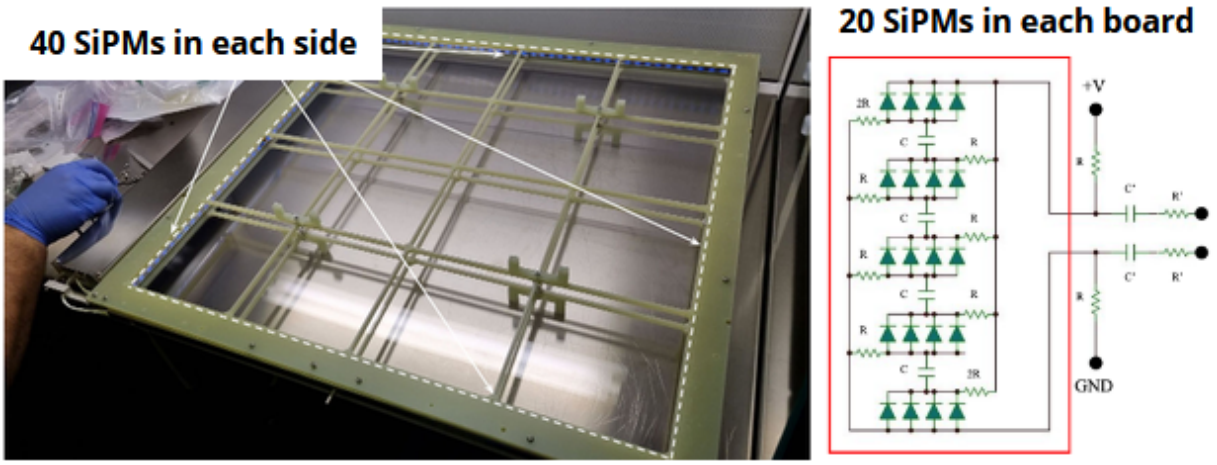


Figure 3.3: Left: Photograph of an X-ARAPUCA module during assembly, highlighting the placement of the SiPMs along its edges (40 SiPMs per side). Right: Electrical schematic of the configuration on a single flexible readout board. The circuit connects 20 SiPMs, arranged in five series-connected groups of four parallel SiPMs.

A X-ARAPUCA module measures approximately $60 \times 60\ cm^2$ in which 160 SiPMs are mounted on 8 flex–boards and positioned around the WLS bar as showed in Fig. 3.3. The SiPMs positioned around the module are arranged in parallel groups (ganged) of 20 along

the perimeter, and read out via two channels per module.
The SiPMs used in the PDS of the DUNE VD module are the FBK RGB-HD and Hamamatsu HPK S13370-6050CN models. These devices were chosen for their high photodetection efficiency (PDE) in the visible spectrum (400-500 nm), reaching approximately 45% at 430 nm at room temperature, as well as their reliability during long-term immersion in liquid argon[58].
At cryogenic temperatures, the breakdown voltage of these sensors is around 30 V or 40 V, depending on the model, and they operate with an overvoltage (OV) of +3 to 5 V. They demonstrate robustness with a failure rate below 0.5%, and their intrinsic dark count rate at cryogenic temperatures remains completely negligible compared to the natural background noise produced by ^{39}Ar decays and other sources.
The selection of these specific SiPM models is driven for the compatibility with cold electronics. In particular, the lower operating voltage of the FBK sensors makes them well-suited to be powered by non-conductive power supply systems, perfectly matching the requirements of the Power-over-Fiber technology employed on the high-voltage cathode[59].

3.3 Photodetecion System in VD

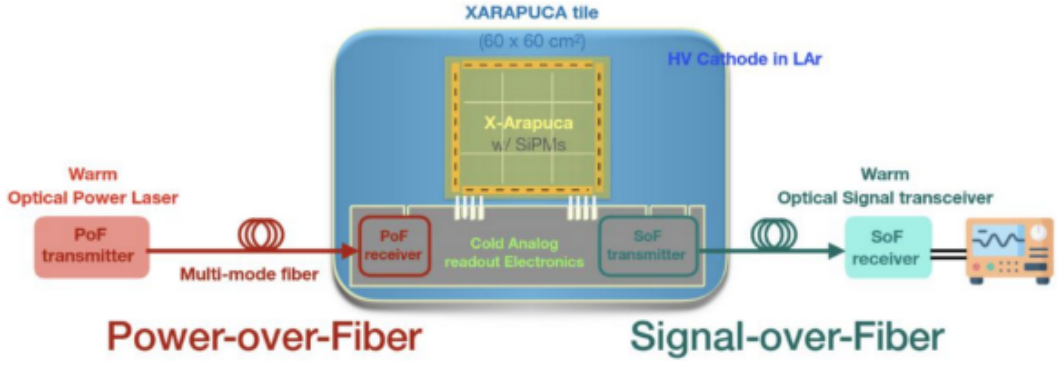


Figure 3.4: Schematic overview of the Power-over-Fiber (PoF) and Signal-over-Fiber (SoF) readout architecture for an X-ARAPUCA tile mounted on the high-voltage cathode in liquid argon (LAr).

In VD, X-ARAPUCA photodetectors are positioned in two distinct locations to optimize the optical coverage of the detection area, as shown in Fig. 2.7. Specifically, 352 modules are positioned on the cryostat membrane behind a transparent field cage. However, this specific placement results in a low light yield, as the scintillation photons are

partially obstructed by the field cage structure.
To compensate for this loss and ensure uniform light collection throughout the detector volume, an additional 320 modules are installed directly on the high-voltage (HV) surface of the cathode [60]. It is important to remind that the cathode operates at an extremely high voltage of -300 kV. Consequently, to operate the devices safely in this environment, both power supply and signal transmission must be managed exclusively through non-conductive materials. This is achieved using Power over Fiber (PoF) and Signal over Fiber (SoF) systems, which represent novel technologies developed for the DUNE experiment, as shown in Fig. 3.4

3.3.1 Power over Fiber System

The PoF system is designed to supply power for the X-ARAPUCA detector and readout electronics, whilst keeping the electronics it powers completely isolated from high voltage. It uses light from infrared lasers ($\lambda = 805$ nm) located outside the cryostat at a power set to 800 mW (which can reach up to 2 W); a multimode (MM) optical fibre ($63.5\mu m$ core) carries the light inside the cryostat.

On each X-ARAPUCA detector there are two gallium arsenide (GaAs) optical power

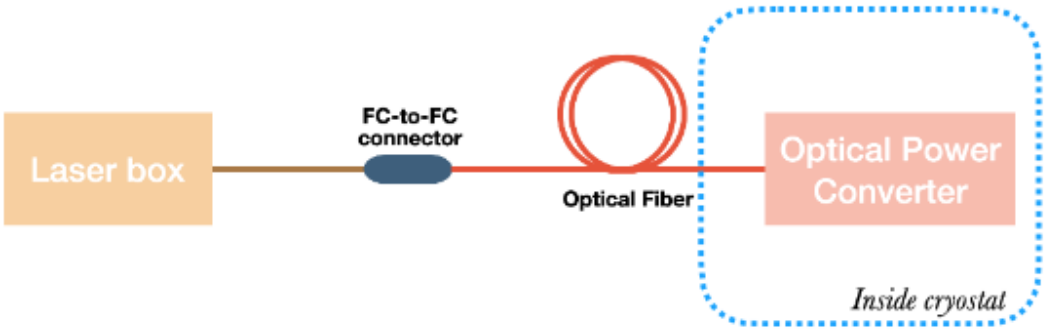


Figure 3.5: Block diagram of the Power-over-Fiber (PoF) system. Light from the Laser box is transmitted via an optical fiber, connected by an FC-to-FC adapter, to the Optical Power Converter located inside the cryostat.

converters (OPC), which, much like a solar cell, convert the optical power into electrical power with an efficiency of approximately 50% [61]. While the efficiency of these converters is highly temperature-dependent, their operation inside the cryostat is stable, as the LAr temperature is fixed at 87 K.
Using a high-power light signal to power the SiPMs (light detectors) could pose a risk of

increasing the rate of individual photoelectrons; although their peak sensitivity is at 500 nm, they still possess a small sensitivity at 800 nm. Given the high intensity of the laser, a fraction of this light could still be detected by the X-ARAPUCA.
To prevent this from happening, the fibres use opaque coatings to prevent light from escaping, such as a black polyvinylidene fluoride (PVDF) sheath and metallic connectors. The three main components (the lasers, the fibres and the power converter) are shown in the PoF diagram shown in Fig. 3.5.

3.4 Signal over Fiber System

In a similar way to the system just described, a dedicated readout chain has been developed to transmit the signal from the SiPMs out of the cryostat; this is also divided into three main stages: the cold electronics, located inside the cryostat; the transmission of the signal via optical fibre; and the warm electronics, located outside the detector at room temperature. The cold electronics section is responsible for reading and amplifying the analogue signal, while the warm electronics section receives the optical signal, digitises it, and routes it to the DAQ system.
Fig. 3.6 shows the entire readout system, which will be described in detail.

3.4.1 Cold electronics

The central component in this stage is the DUNE Cold Electronics Motherboard, the DCEM, which receives the signal from the SiPMs and transmits the same signal via the lasers.
The SiPMs are organised into groups of twenty, according to a configuration that allows them to share the same line that supplies both the bias voltage and the voltage required for differential readout.
As can be seen on the left-hand side of Fig. 3.6, the signal of the 20 SiPMs is transmitted via shielded twisted-pair cables approximately 1 m in length as a differential signal to the DCEM.

Power is supplied via the PoF system. On the DCEM, as previously mentioned, two OPCs receive the optical power and feed two Low-Dropout (LDO) linear voltage regulators that power the board. This type of regulator has an internal resistance that varies according to the input voltage, producing a constant output voltage; it operates optimally even when the input voltage is very close to the output voltage.

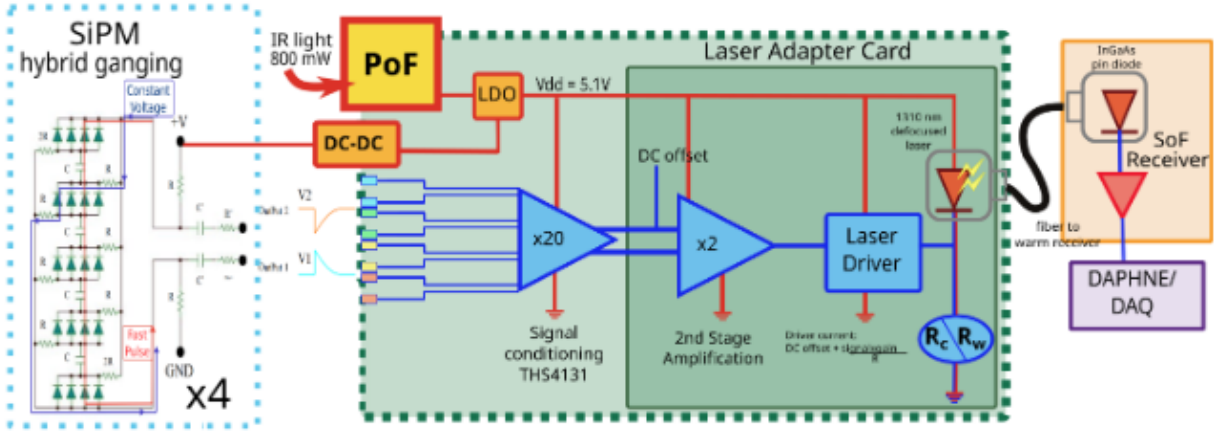


Figure 3.6: Schematic of the Signal-over-Fiber (SoF) readout electronics. On the left, the hybrid SiPM ganging powered via PoF; in the center, the cryogenic board with amplification stages and the laser driver; on the right, the room-temperature optical receiver connected to the DAPHNE/DAQ digitization electronics.

Furthermore, the SiPMs are biased using a DC-DC voltage step-up converter; this component receives approximately 6 V from the PoF-OPCs and converts it to roughly 47 V. The physical layout of these parts can be seen in Fig. 3.7, where the PoF components are located on the left, the DC-DC converter on the right, and the SiPM connectors are arranged at the top and bottom.

DCEM board

Fig. 3.7 shows a schematic of the simplified transmitter circuit; on the left, input signals are processed by a two-stage analogue amplification chain. The first amplification stage utilizes a Fully-Differential Amplifier (FDA) providing a gain of 20. Operating with a differential signal at this stage is crucial since the cables connecting the SiPMs to the board can ”pick up” ambient noise (pick up noise). Because this external noise induces an identical voltage on both wires of the twisted pair (common-mode noise), the differential amplifier effectively cancels it out when calculating the difference between the two inputs.
The second stage employs an amplifier with a gain of 2 to convert the differential signal into a single-ended unipolar signal. Overall, the amplification chain provides a total gain of 40.
This specific value represents a careful optimization compromise: while a larger gain yields a better Signal-to-Noise Ratio (SNR), it simultaneously reduces the dynamic range of the detector.
For long-term operation in liquid argon, standard CMOS components must be avoided due

to the "hot carrier effect," which degrades performance over time in cryogenic environments. Consequently, both amplifiers in this circuit are based on Silicon-Germanium (SiGe) bipolar technology, ensuring superior long-term stability and reliability.

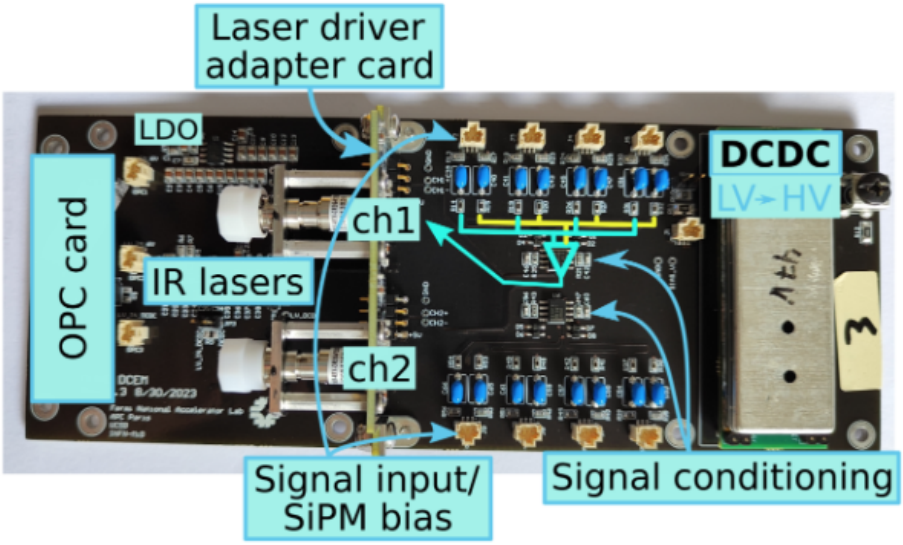


Figure 3.7: A detailed hardware overview of the DCEM circuit board. The image maps out the critical components, showing the integration of the IR lasers with the central signal conditioning electronics. It points out the power distribution modules, including the LDO and the high-voltage DCDC block, alongside multiple SiPM bias connectors

Furthermore, the gain also affects the bandwidth; as the gain increases, the bandwidth decreases. The expected signal has a rise time of approximately 50 ns and an expected voltage level per photoelectron of 30–50 μV; therefore, a bandwidth of at least 20 MHz will be required to transmit the signal without significant distortion, along with sufficient amplification to distinguish very low signals

Following the amplification stage, the unipolar signal goes to the laser driver. The laser driver is mounted on a board positioned at the centre of the DCEM, as shown in Fig. 3.7, and contains a circuit that converts the voltage signal into a current. This current, combined with a DC bias current, drives the infrared lasers housed on the board.
Upon entering the laser driver board, the signal passes through a SiGe bipolar operational amplifier (LMH6642) configured with a gain of 1, used in combination with an external SiGe transistor.

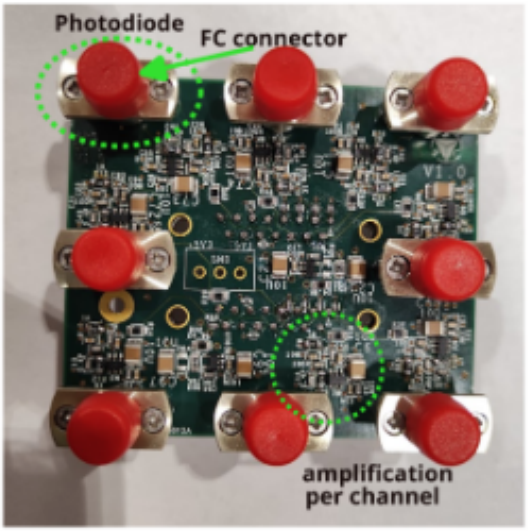


Figure 3.8: The 8-channel warm optical receiver board. The annotations highlight the photodiodes equipped with FC connectors and the dedicated amplification circuitry for each channel.

To ensure the laser current remains above the threshold current whilst staying within the linear operating region, a constant DC offset is added to the signal. For this reason, the laser driver circuit incorporates a negative temperature coefficient (NTC) thermistor, whose resistance decreases at higher temperatures and increases at lower temperatures.
At room temperature, its resistance is $R_{warm} = 16\Omega$, resulting in a warm bias current of $I_{warm} \sim 15$ mA. At cryogenic temperatures, its resistance becomes extremely high; this alters the parallel bias network so that the equivalent resistance becomes $R_{cold} \sim 70\Omega$, resulting in a properly adjusted cold bias current of $I_{cold} = 3$ mA.

The laser diodes used in the project are Fabry-Pérot (FP) side-emitting diodes equipped with an internal photodiode, with an emission wavelength of approximately 1310 nm. In this device, light is generated in the active region and emitted from the edge of the semiconductor chip, parallel to its surface.
At cryogenic temperatures, lasers generally become more efficient, as their threshold current—that is, the minimum current at which the laser begins to emit linearly with respect to the supply current—decreases; for example, for FP lasers, it changes from 10 mA to 2–3 mA. However, despite the increase in laser performance, another problem arises due to the difference in refractive index between LAr and air. The light emitted by the laser should be focused through a lens onto the optical fibre, but the focusing system in LAr has a different refractive index compared to air. This difference leads to an incorrect focal

distance, which results in poor laser-fibre coupling.
The solution is to replace standard lasers with lasers that are defocused under normal conditions but have the correct distance between the lens and the fibre to ensure alignment in LAr.

The light output from the laser diodes is then directed into a multimode (MM) optical fibre via a laser FC connector. These fibres are of the same type as those used in the PoF circuit. Through these fibres, the signal safely travels away from the high-voltage environment, exits the cryostat, and reaches the warm electronics located outside.

3.4.2 Warm electronics

In the experiment, this electronic circuit is located outside the cryostat at room temperature and receives the signal from the SiPMs in the form of a light pulse transmitted via optical fibres, converting it back into an analogue electrical signal.
Initially, the Koheron PD100, a commercially available single-channel device, was used as the signal receiver[62]. Subsequently, the DUNE group at the AstroParticule et Cosmologie (APC) laboratory developed a new receiver—an eight-channel version based on the Koheron circuit but adapted for interface with digital electronics, as shown in Fig. 3.8.

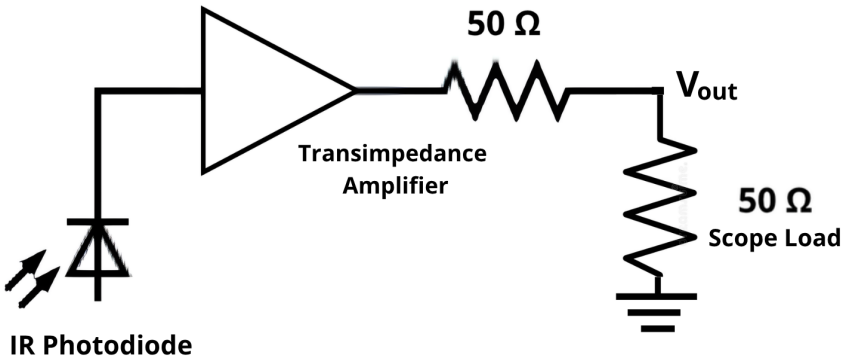
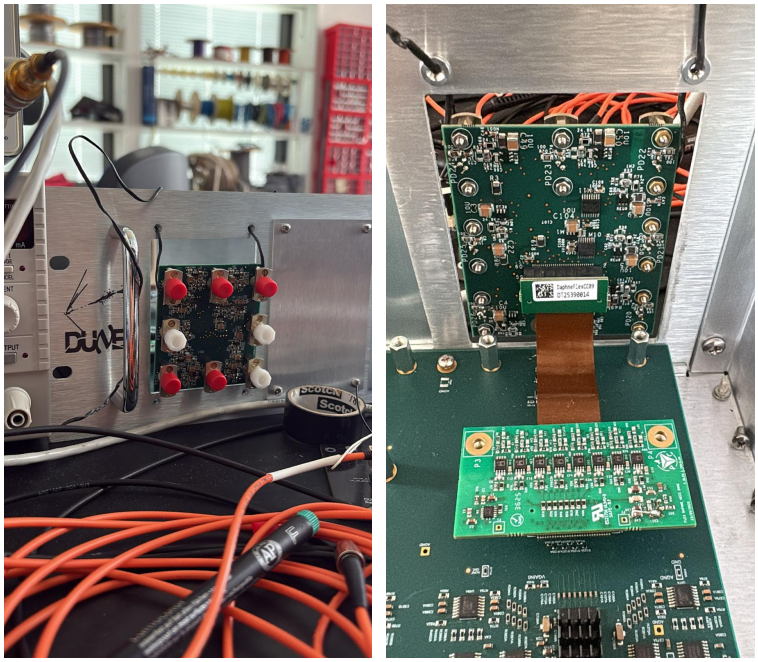


Figure 3.9: Simplified schematic of a single receiver channel. The incoming optical signal is converted to a photocurrent by the IR photodiode and amplified by the transimpedance amplifier (OPA847). The 50 Ω series resistor on the board and the 50 Ω input impedance of the oscilloscope form a 1:2 voltage divider, effectively halving the voltage step amplitude measured at the V_{out} node.

Each of these 8 channels is equipped with an IR (InGaAs) Photodiode, the single circuit is shown in Fig. 3.9. The primary function of the receiver circuit is to convert

this optical signal back into a readable electrical format. When the infrared light strikes the photodiode's active area, it generates a photocurrent. This current is immediately processed by a Wide- band, Ultra-Low Noise, Voltage-Feedback OPERATIONAL AMPLIFIER (OPA847), which amplifies the signal and converts it into a proportional voltage step, the gain applied to the current signal coming from the photodiode is determined by the feedback resistor, which is 3 kOhm.
The power-to-current conversion responsivity R_λ of the PDs depends on the wavelength of the incident light; for light at 1310 nm, it ranges between 0.8 and 0.9 A/W, depending on the manufacturer. Furthermore, the PD's sensitive area must be sufficiently wide to cover the dimensions of the fibre core, so as not to scatter the signal light; for this reason, a photodiode with a 120 μm diameter was chosen.



(a) The front of the receiver board, with the photodiodes that are connected to the optical fibers during the experiment

(b) The back of the receiver board connected with DAPHNE via the compensator card

Figure 3.10: The figure shows the front and back of the receiver board connected to Daphne

The current output of the photodiode is fed into a high-gain transimpedance amplifier. This amplification stage is strictly necessary because the weak optical signals ($\sim \mu$W) generate minimal photocurrents (in the μA range).
To ensure that even the smallest signals—which might originate from a single photoelec-

tron—are correctly digitised, the voltage signal must be amplified to be comparable with the Least Significant Bit (LSB) of the subsequent Analog-to-Digital Converter (ADC), which is approximately $122\,\mu$V (calculated from a 2 V range over 2^{14} bits).
The circuit has therefore been designed to provide over 1 kV/A of gain and a wide dynamic range, in order to accommodate even larger signals whilst also ensuring a good SNR and fast transmission.

An additional digitization stage is also included in the receiver architecture to monitor the baseline level of the signal. This stage is based on a relatively slow ADC, whose low sampling rate is sufficient for tracking the baseline rather than the fast variations of the received signal. Since the SOF receiver is AC-coupled to the DAPHNE system, the absolute baseline level of the signal cannot be directly determined from the digitized waveform, requiring an independent measurement of the baseline during operation.

Finally, the signal enters the digitisation module, the DAPHNE (Detector electronics for Acquiring PHotons from NEutrinos) board, via a compensator card, shown in the Fig. 3.10b. This card features the same connectivity as DAPHNE and utilizes a flexible kapton circuit as its physical interface. It acts essentially as a hardware "filter" (the "compensator") designed to counteract the pulse-shaping distortions—such as the characteristic undershoot—induced by DAPHNE's AC-coupled inputs, ensuring that the waveform remains balanced and properly shaped before digitization.
DAPHNE samples the signal waveform at 65 MHz using a 14-bit ADC and transmits the digitised data to the DAQ system, while supplying power to the cold front-end and providing trigger capabilities.

Chapter 4

Measurements at APC laboratory

Chapter 3 introduced the electronic readout system, and this chapter will now present the measurements carried out at the APC laboratory in Paris. The DUNE group at APC focuses on the development of the SoF readout circuit through a joint effort involving physicists and engineers. This chapter first presents the measurements related to the cold transmitter, specifically the laser tests at cryogenic temperatures, and second, the measurements regarding the receiver board.
The experimental work was conducted in collaboration with the DUNE APC team, including my supervisor Sabrina Sacerdoti, group leader Jaime Dawson, and Sylvie Blin (responsable technique) who provided vital engineering support. Additionally, all measurements were performed alongside fellow internship student Luca Malinverni.

4.1 SoF Transmitter and Laser Characterization

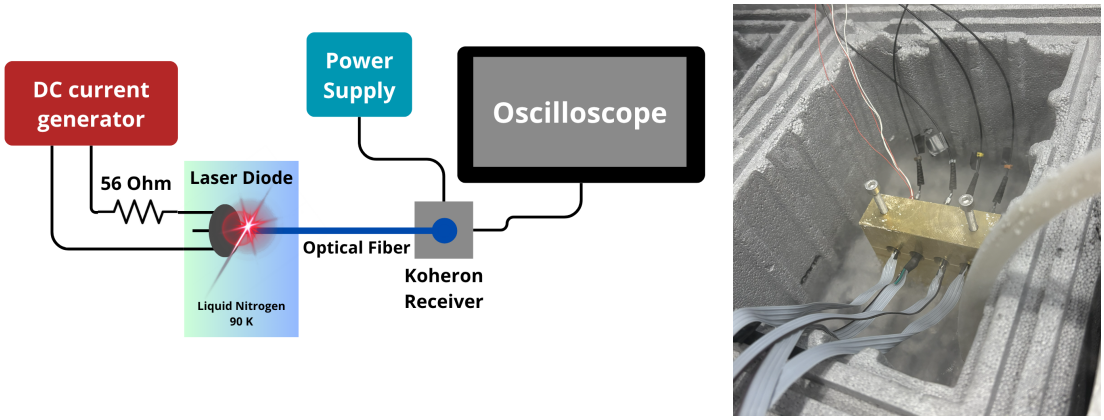
As previously described in Chapter 3, the SoF Transmitter is a crucial component that relies on infrared laser diodes to convert electrical signals into optical pulses. For the final DUNE detector, a massive production scale is required, and approximately 770 lasers need to be procured.
Because these components are destined to operate submerged in liquid argon, before these lasers can be permanently integrated into the final laser adapter cards, a rapid but rigorous validation of their Power-Voltage-Current (PVI) characteristics at cryogenic temperature is mandatory.

As part of the Quality Assurance and Quality Control (QA/QC) procedure, the official validation process designed to identify and intercept defective components before final

assembly, this test aims to demonstrate that the laser light output remains strictly linear with respect to the input current at cryogenic temperatures.
Previous experience with the batch acquired in 2025 revealed a significant batch dependence: while those lasers exhibited good linearity at room temperature, their response became highly non-linear when operated in cold conditions. Due to this observed batch dependence, it is now a mandatory procedure to test at least 10% of the lasers from any given batch in a cryogenic environment before permanently mounting them on the PCBs.

Setup

The test must be performed in liquid nitrogen. The liquid nitrogen is initially stored in a cryogenic tank at a temperature of 77 K; it is then poured into a special polystyrene container using cryogenic gloves. A special copper container holds four lasers at a time as shown in Fig. 4.1b; the lasers are in series with a 56Ω resistor and powered by a KEYSIGHT E36312A, TRiple Output Programmable DC Power Supply, connected via a multi-wire cable that terminates at the laser pin header. The four lasers are connected to four optical



(a) Schematic representation of the experimental setup.

(b) Box housing the laser diode in LN

Figure 4.1: Cryogenic experimental setup for laser diode characterization.

fibers, through which the emitted light signal reaches the receiver; in this case we used the Koheron receiver introduced in the previous chapter. Four Koheron receivers are available in the laboratory; three of them have a gain of 4 kΩ, while one has a gain of 3 kΩ. The sole unit with a gain of 3 kΩ was used to detect the signal emitted by a laser belonging to the 2025 batch. The other three are connected to the new 2026 lasers, the ones being tested.
The 2025 laser is used to verify that the cryogenic conditions of the system are sufficient to affect the laser's operation and produce the anomalous results. The lasers under test

must operate in linear mode, even when malfunctioning lasers cease to function properly. The temperature inside the liquid nitrogen container was measured using a PT100 sensor. By measuring the resistance value within the laser structure—which is temperature-sensitive—and inverting the Callendar–Van Dusen equation (4.1), which describes how resistance varies with temperature, it is found that when $R \approx 25$, the operating temperature is approximately 90–100 K.

$$R(\theta) = R_0\left[1 + A\theta + B\theta^2 + C\theta^3(\theta - 100)\right] \tag{4.1}$$

Data Acquisition

Data acquisition is performed using a Python script that sets current values from 0.5 to 60 mA in the KEITHLEY 2460 SourceMeter and records both the output voltage from the Koheron optical receiver (measured by the TELEDYNE LECROY 6034 High Definition Oscilloscope[63]) and the voltage drop across the circuit (measured by the Keithley). Specifically, the test allows us to view a graphical interface with the following interactive graphs:

- **V-I characteristic** of the laser diode, shown in Fig. 4.2a. The Keithley 2460 acts as both the current source and the voltmeter, measuring the circuit via multi-wire connections. The actual voltage across the diode is then calculated as $V_{laser} = V_{tot} - V_R$, where V_R is the voltage drop across the series resistor.

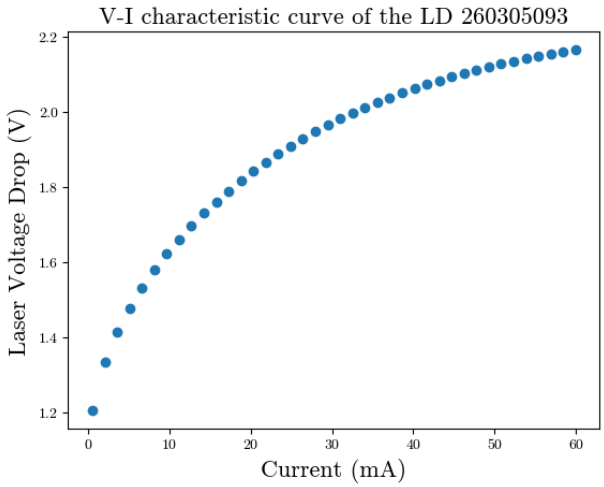
- The I_{in} **vs** V_{PDout} curve, shown in Fig. 4.2b, where V_{PDout} is the voltage measured across the internal monitor photodiode inside the laser, serving as a monitor for the emitted optical power.

- The I_{in} **vs** P_{out} curve, shown in Fig. 4.2c, where P_{out} is the output power calculated from the voltage output measured by the oscilloscope. This voltage value can be directly converted into the corresponding optical power to evaluate the laser's emission by tracing the signal path backwards.

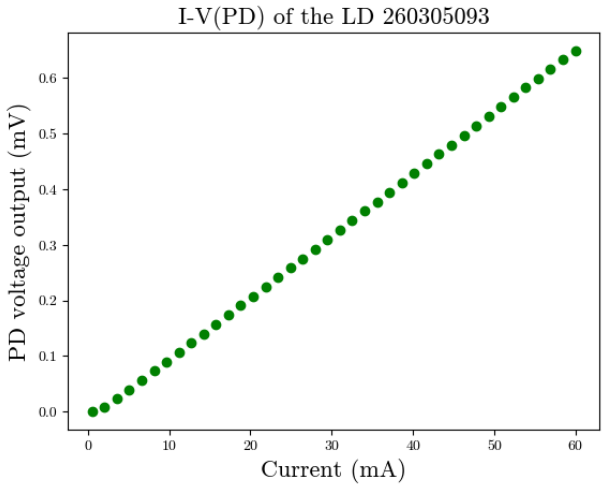
- **Waveforms** recorded with the oscilloscope for each input current; the signal waveform is a constant voltage. This graph is shown in Fig. 4.5.

The correct formula to convert the measured output voltage into optical power, based on the Koheron receiver circuit featuring a 3 kΩ/4 kΩ transimpedance gain, similar the one in Fig. 3.9), is given by:

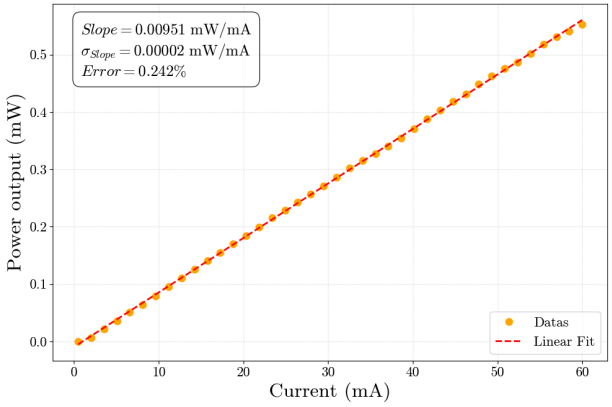
$$P\,[mW] = \frac{2V_{out}[mV]}{R_\lambda G} \tag{4.2}$$



(a) V–I characteristic



(b) I_{in} vs V_{PDout}



(c) *I–P* characteristic

Figure 4.2: Experimental characterisation curves obtained for LD 260305093: (a) diode voltage drop as a function of forward current, (b) monitor photodiode response, and (c) emitted optical power.

Where R_λ is the responsivity of the photodiode in $\frac{A}{W}$, G is the gain in $\frac{V}{A}$, and the factor of 2 is required to take into account the two 50-ohm resistors, one in the circuit and the other representing the oscilloscope's load.

For each laser, the test was initially conducted at room temperature. To speed up data

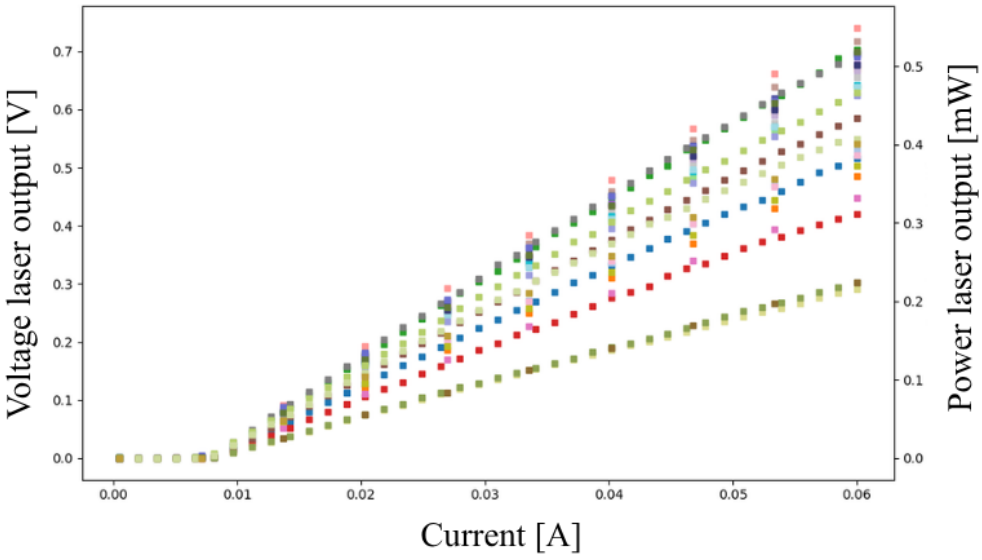
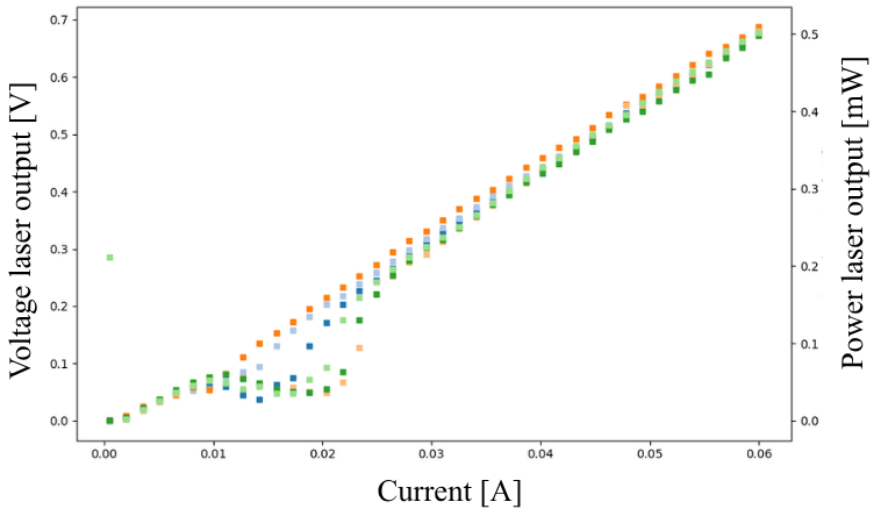


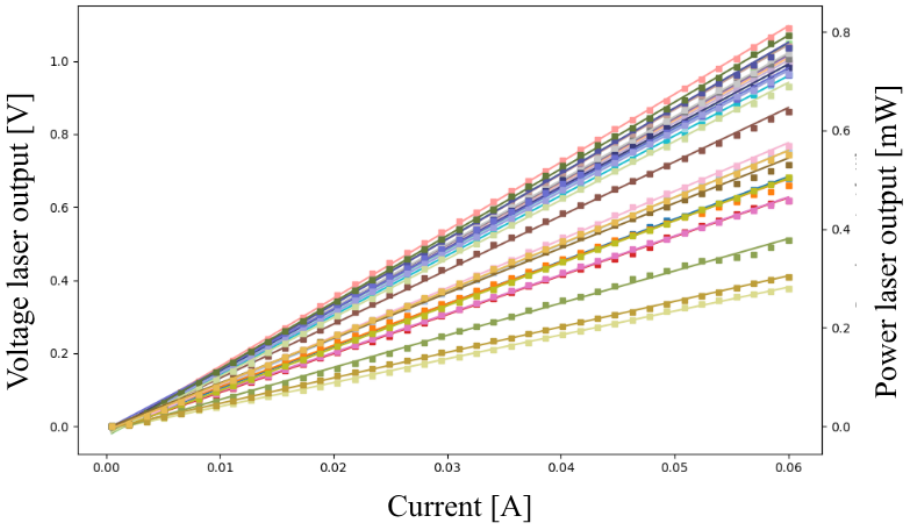
Figure 4.3: Linearity plot of all the laser under test of 2026 at room temperature.

collection after the first set of lasers, we chose to record only half the data points, since this measurement serves only as a verification and not as the actual QA/QC test. At the end of the full cryogenic testing cycle, the randomly selected lasers are dried and safely stored in the designated box.

To properly evaluate the system's performance, we analyze the linearity plots, which graph the laser's measured optical output response against the applied input driving current. This characteristic curve is shown in Fig. 4.3 at room temperature for the 2026 lasers, and in Fig. 4.4a and 4.4b at cryogenic temperatures for the 2025 and 2026 batches, respectively. It is important to note that although testing in cold N_2 gas is not optimal compared to the final liquid argon environment, it is a crucial validation step as it demonstrates the required linear behavior.



(a) Linearity plot of defocused lasers from the 2025 batch tested at cryogenic temperatures. These lasers were employed as a control reference to verify that the cryogenic conditions were sufficient to reproduce the expected non-linear anomaly in the 10–25 mA range.



(b) Linearity of all the lasers under test of 2026 in liquid nitrogen.

Figure 4.4: Comparison of cryogenic laser testing results.

The linearity check of the 2026 laser batch is aided by a linear fit of the experimental data, performed using Python's optimization routines. As depicted in the V-I characteristic curve (Fig. 4.2a), the laser diode exhibits the expected non-linear forward voltage drop as the driving current increases up to 60 mA. However, the crucial parameters for our validation are the optical responses. Both the internal monitor photodiode response (Fig. 4.2b) and the calculated optical power output (Fig. 4.2c and Fig. 4.4b) demonstrate a strictly proportional relationship with the input current. To quantitatively assess this, a linear regression was applied to the data. By extracting the fit uncertainties directly from the covariance matrix (`pcov`), the relative error on the slope is confirmed to be extremely small—for instance, just 0.24% for the laser diode LD 260305093.

The linear fit mathematically confirms that, unlike the problematic 2025 batch (which

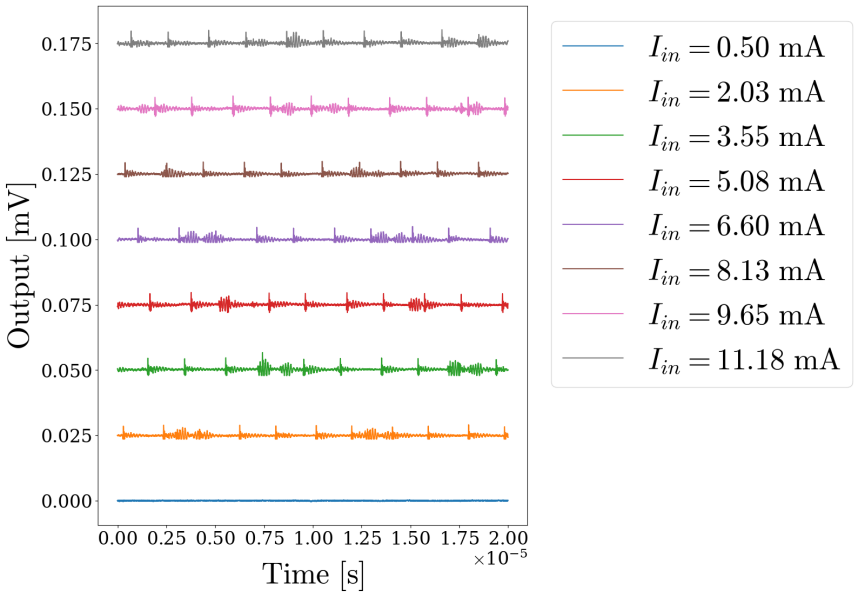


Figure 4.5: Waveforms of the laser 260305088 of 2026 bunch as the direct current supplying them varies from 0.5 mA to 12 mA.

shows a large non-linearity in the 10–25 mA range, as seen in Fig. 4.4a), the new 2026 lasers maintain a perfectly linear emission profile without any saturation or distortion in cold conditions. This robust linearity is corroborated by the coefficient of determination (R^2) extracted from the fits. Across the entire 2026 batch tested in liquid nitrogen, the R^2 values consistently exceed 0.998, indicating an optimal agreement between the data and the linear model. This successful validation allows these components to pass the QA/QC test and proceed to the final PCB assembly.

4.2 SoF Warm Receiver Testbench

Most of my work at the APC laboratory focused on studying the SoF warm receiver boards. As explained in chapter 3, in the experiment, this electronic circuit is located outside the cryostat at room temperature, and it receives the X-ARAPUCA signal as a light pulse transmitted through optical fibers. The output of the SoF warm receiver is an electrical signal, which will be processed by the next readout stage of chain, Daphne. Figure 3.10 shows a picture of the SoF warm receiver connected to DAPHNE.

During my internship in the laboratory, I worked on the development of the testbench for SoF Warm Receiver Production. During my internship in the laboratory, I worked on the development of the testbench for SoF Warm Receiver Production. The APC group has to provide warm SoF readout electronics for VD/FD, comprising 640 channels distributed across 80 boards. Before installation, these boards must undergo a QA/QC check to verify that all channels have been correctly fabricated and function properly. Consequently, these devices need to be tested. For this reason, I focused on designing the protocol that will be used to test the receiver boards to be used in the DUNE experiment.

The main goal of the test bench is to verify that the receiver board functions correctly through a testing procedure. First, the receiver's linearity is measured before integration. Once the full receiver is assembled and tested, further evaluations are conducted, including power consumption, overall circuit linearity, board-to-board uniformity, and saturation limits.
The initial receiver response is verified by applying a light pulse of varying amplitude to the input and recording the linear variation in the response for each amplitude value. the expected result is a strictly proportional relationship between the input signal and the output voltage, with minimal dispersion among channels and negligible crosstalk.

During the commissioning of the testbench, initial measurements yielded unexpected results because certain stages of the transmission chain have non-ideal performance. Rather than halting the workflow to await replacement parts, our primary objective was to develop reliable alternative solutions, finding practical compromises and optimizing the acquisition process using the available components. This approach aim to prevent similar problem during future data acquisition process and it's useful to suggest how to identify analogous anomalies.

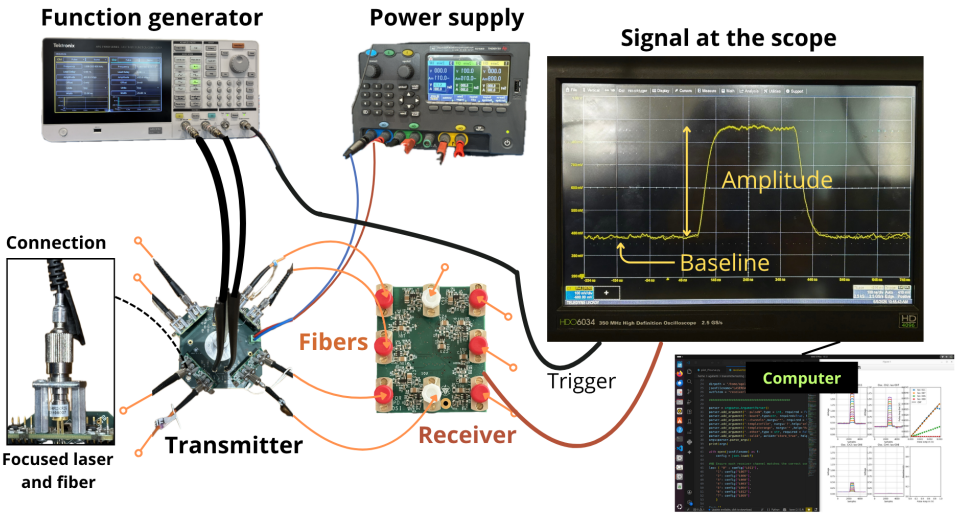


Figure 4.6: Picture of the complete testbench setup.

4.2.1 Setup Descriprition

In order to understand the measurement presented in this section, it is helpful to introduce the path of the signal from its generation by the function generator to the voltage observed on the oscilloscope, shown in Fig. 4.6. We divide the signal path into three stages, which will be described separately in greater detail below. In the first stage, the circuit uses the voltage signal to generate the current that powers the lasers, which emit a quantity of light whose power is proportional to the difference between the initial current and the laser's threshold current ($P_{light} \propto (I_{in} - I_{tr})$; in the second stage, the light source is transmitted to the receiver's photodiodes via the optical fibre; in the final stage, the light is converted back into an electrical signal by the photodiodes.

The transmitter circuit

To test the receiver, there is a need to input known and controlled light pulses. Rather than operating at cryogenic temperatures, the setup uses the same SoF transmitter described in Chapter 3.4 adapted for room temperature operation. Furthermore, to handle multiple simultaneous inputs, an adapter board is employed (as shown in Fig. 4.7), which uses the same laser driver circuit to emit infrared light. This board applies a known amplification and distributes the signal separately to channel 1 and channel 2 across four laser adapter cards.

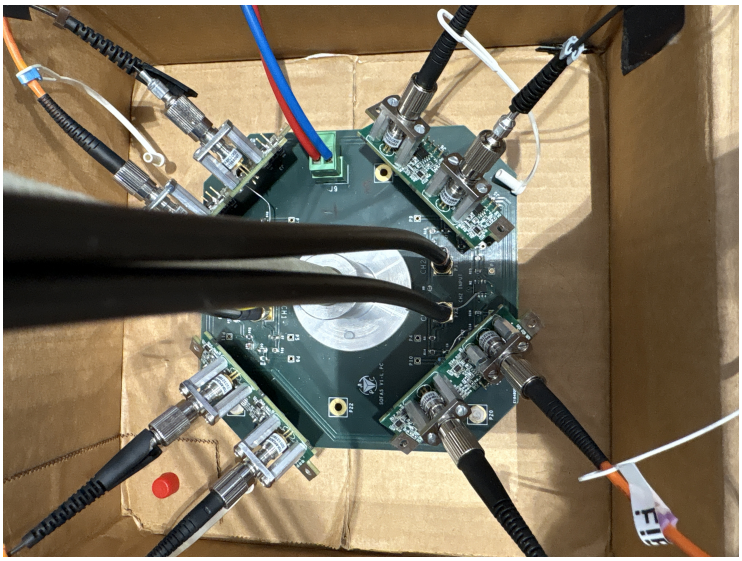


Figure 4.7: Warm version of the transmitter module designed for the testbench in the APC laboratory.

The circuit is specifically designed to receive the signal from TEKTRONIX AFG 3022B Function Generator, emulating differential input from X-ARAPUCA. It produces two voltage steps of equal amplitude identical frequency and bandwidth, but with opposite polarity. The pulse shape was chosen with a width of 300 ns, rise time of 50 ns, and fall time of 50 ns.

At the output of the voltage generator, the two signals are attenuated using a 20 dB BNC attenuators of a factor 1/10.
An attenuator was used to control the voltage values with greater precision. Since our function generator has a precision of 1 mV, as shown in Fig. 4.8, during our initial measurements with the defocused lasers, we observed discontinuities in the linearity of the output emission when the input pulse amplitude approaches the minimum value that can be set by the generator.
By introducing a factor of 10 attenuation, larger amplitudes can be set on the function generator and subsequently reduced at the output, allowing much smaller voltage steps to be generated with the required precision. The amplitudes of the voltage steps after attenuation, V_{in} [mV], are used as the independent variables in our linearity plot that will be discussed later.

After attenuation, the two signals of opposite polarity enter separately into the SOFAs transmitter board. In SOFAs there is a first attenuation stage consisting of a voltage divider formed by 240 Ω series resistors and a 100 Ω shunt resistor, followed by an amplifi-

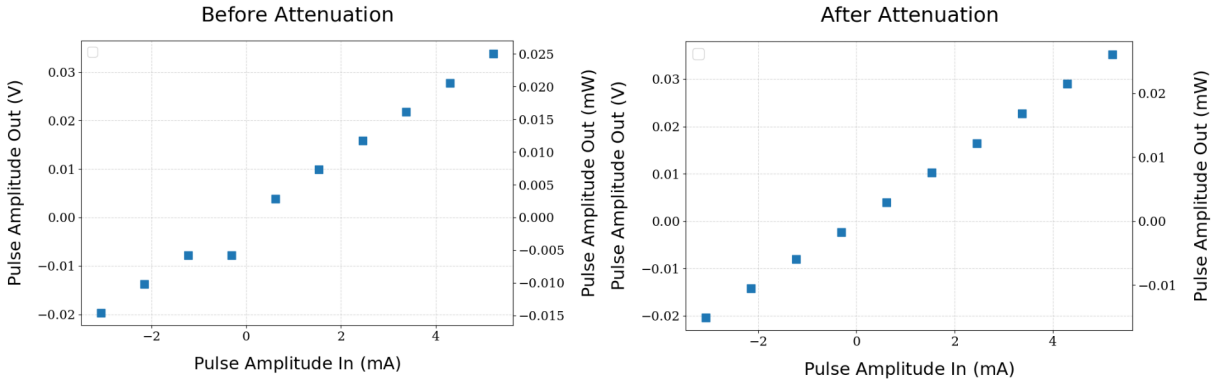


Figure 4.8: Comparison of the system's linearity before (left) and after (right) the use of an attenuator, obtained with a defocused laser. The left plot shows non-linear artifacts near zero input voltage, caused by the minimum amplitude step resolution of the TEKTRONIX function generator. The introduction of the attenuator (right plot) enabled the generation of finer effective voltage steps, restoring a proportional response.

cation stage using fully differential amplifier THS4131, the same model used on the DCEM as described in Section 3.4.1, with 1 $k\Omega$ feedback resistors; the signals are thus amplified by a total factor of 4.6, as shown in the diagram in Fig 4.9.

The SOFAS transmitter board is equipped with two amplifiers,one for channel 1 and one for channel 2, followed by four connectors that interface with the laser adapter cards. While it shares the same general architecture as the SoF transmitter discussed in Section 3.4.1, the testbench setup features two important differences: it utilizes a different amplifier model from an older version, and it employs "normal" (focused) lasers operating at room temperature rather than defocused lasers designed for cryogenic use in liquid argon.
Because these lasers operate at room temperature, no voltage divider is needed, as the current-voltage relationship is already adequate.

The output signal from the amplifier is a voltage step, with an offset previously discussed in section 3.4.1, whose value depends on the power supply voltage of the transmitter board. In our case, with a supply voltage of 5.1 V, the offset is 400 mV. As the final component of the circuit, the laser driver converts the input voltage into the drive current for the lasers via a resistor system, which also enables input signal tuning. The infrared light is then transmitted via optical fibres to the photodiodes to the receiver board.

.

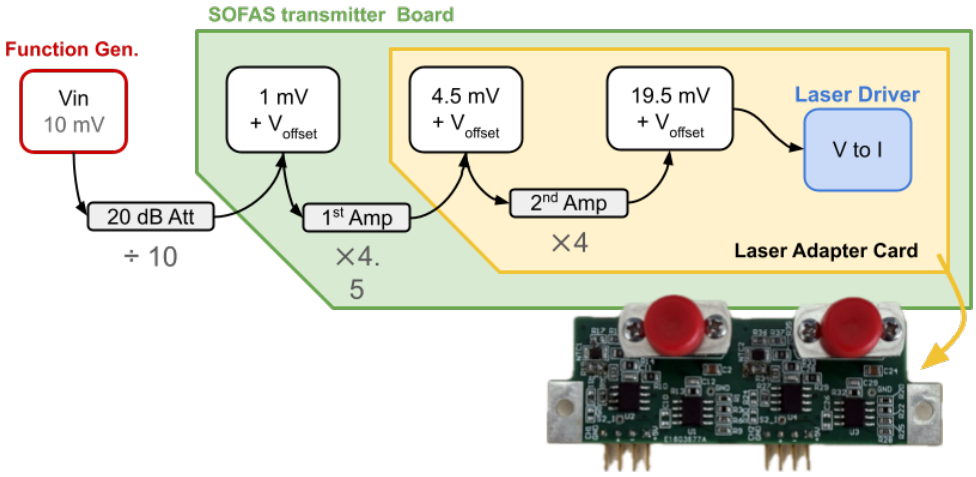


Figure 4.9: Diagram showing the various stages of the signal within the transmitter module

Laser Characterisation

The first aspect that was investigated concerns the properties of the lasers we used as light sources.The lasers soldered onto the laser driver modules for the testbench setup are Lasermate focused laser diodes operating at a 1310 nm wavelength, with a nominal optical output power of 1 mW.

Since the input signal to the transmitter board comes from the same function generator, each of the four laser driver modules uses the same voltage level to power the lasers. Although the setup is built so that all lasers receive an almost identical current signal, with variations primarily driven by 1% resistor tolerances and slight differences in amplifier response, the resulting light output can still vary significantly due to inherent variations in each laser's electro-optical response. Unfortunately, this causes the amplitude of the receiver's output signals to vary noticeably across channels, as shown in Fig 4.10 .

In Fig. 4.11, one can compare the characteristic voltage output curves of the available lasers, measured at the oscilloscope after the receiver. As the voltage is directly proportional to the optical power (see Eq. 4.2), these curves show that the threshold current (ranging approximately from 8 mA to 9 mA) and the linear coefficient vary from laser to laser.

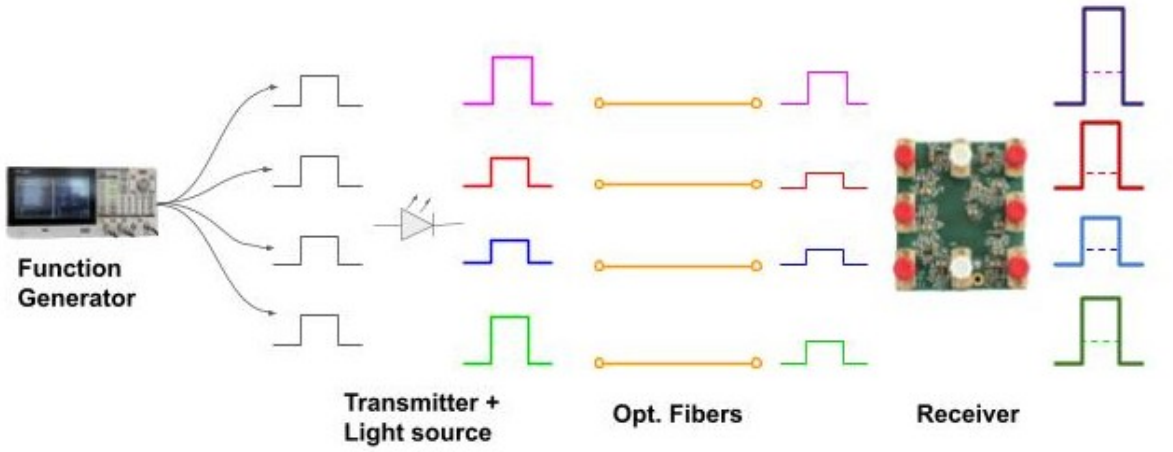


Figure 4.10: Diagram explaining how the differentiated laser emission propagates through the electronic chain, producing different and incomparable signals in the channels of the receiver board

This means for the same injection current, different lasers yield different light outputs. For instance, at a direct current of 13 mA, the most efficient laser produces an output of 1600 mV, hitting the saturation limit of 1.6 V, whereas the least efficient ones only reach between 680 mV and 800 mV. This poses a challenge for our testbench: to properly test all receiver channels under similar conditions, the channels must receive comparable amounts of light. Consequently, this discrepancy prevents us from using the same input signal but also acquire a consistent number of data points to validate the linearity across all channels.

To achieve a uniform optical output across the different lasers, we used their characteristic curves to determine the required driving current for a given light output level.
By adjusting the resistor network (comprising series and parallel resistors) at the end of the driver circuit, we compensated for individual laser variations, ensuring that identical input pulses from the function generator produce consistent light signals.
The resistance R, which converts the voltage step entering the laser driver into current, consists of resistors and capacitors connected in series and in parallel as shown Fig. 4.12. The load resistance at the end of the circuit that affects the DC voltage contribution V_{offset} generated in the amplification stage is different from the one used to calculate the current contribution proportional to the step voltage $\Delta V_{in} G$, specifically:

$$I_{DC} = \frac{V_{offset}}{R_2 \parallel (R_{\mathrm{NTC}} + R_3)} = \frac{V_{offset}}{R_{DC}} \tag{4.3}$$

$$I_{AC} = \frac{\Delta VG}{R_1 \parallel R_2 \parallel (R_{\mathrm{NTC}} + R_3)} = \frac{\Delta VG}{R_{AC}} \tag{4.4}$$

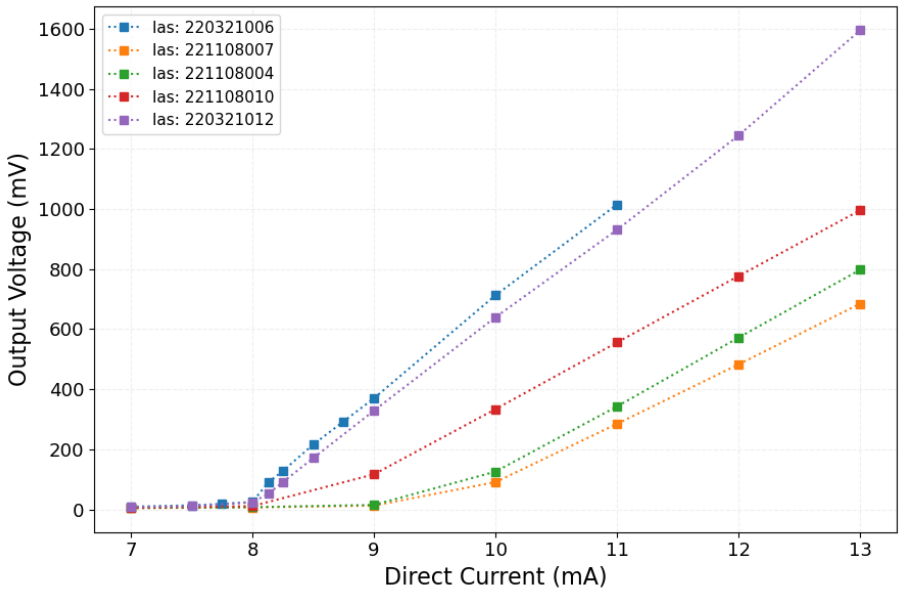


Figure 4.11: Characteristic curves of some of the lasers used in the laboratory, showing different emission thresholds.These curves were acquired by driving the lasers with varying injection currents using a Keithley SourceMeter SMU.

The resistor R_{NTC} is a resistive component whose electrical resistance decreases nonlinearly as the temperature rises; in our case, we measured a nominal value of 10 Ω. It is difficult to adjust. The capacitances C_1, C_2, and C_3 each have a value of $1\mu F$. Since they are connected in parallel we add these values together to find the cutoff frequency of the RC branch, which is:

$$\frac{1}{2\pi R_1 C} \tag{4.5}$$

Based on this configuration, the optical power output P_{out} is given by the product of the laser efficiency E_l and the driving current I:

$$P_{out} = E_l \times I = E_l \times \left(\frac{\Delta V_{in} G}{R_{AC}} + \frac{V_{off}}{R_{DC}} \right) \tag{4.6}$$

Consequently, the measured voltage at the oscilloscope after the receiver (V_{out}) depends on the receiver gain G_{rec} (denoted as G_{rec}):

$$V_{out} = G_{rec} \times E_l \times I \tag{4.7}$$

Substituting the current expressions yields the final input-output relation:

$$V_{out} = \frac{G_{rec} \times E_l \times G}{R_{AC}} \Delta V_{in} + \frac{G_{rec} \times E_l}{R_{DC}} V_{off} \tag{4.8}$$

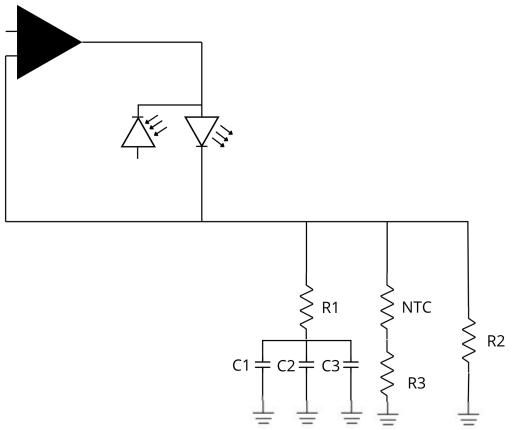


Figure 4.12: Schematic of the resistor and capacitor network at the output of the laser driver. This load network determines both the DC offset and the AC step current used to drive the laser diode.

To achieve a uniform optical output across the different lasers, our goal is to equalize their overall response slopes (m). Based on the circuit model, the measured slope corresponds to:

$$m = \frac{G_{rec} \times E_l \times G}{R_{AC}} \tag{4.9}$$

Therefore, by choosing appropriate values for the resistor network (R_{AC} and R_{DC}), we can obtain a matched behavior between lasers. However, this choice is subject to specific physical constraints regarding the available resistor values and their impact on the signal baseline.

The cutoff frequency (Eq. 4.5) poses the first constraint we must consider when selecting resistors: the frequency must remain around 5 kHz, which corresponds to a resistance R_1 of approximately 10–11 Ω. Since not all resistance values are available in the lab, this constraint allows for R_1 to be either 10 Ω or 12 Ω.

The second constraint that limits our choice of resistors R_i is the requirement that the current flowing through the laser be sufficient to ensure the laser operates in the linear region; that is, the current flowing through the laser must exceed the threshold current,

which, as already noted in Fig. 4.11, differs for each laser. For this reason, we calculated the threshold current for each laser, approximating it to the value of the intercept where the power is zero ($P = 0$ when $I = -\frac{q}{m} \approx I_{tr}$). This value represents an upper limit for selecting the resistance R_{DC}.

$$R \leq R_{max} = \frac{\Delta V G}{I_{tr}} \tag{4.10}$$

The third constraint requires the final offset voltage level to be comparable across all lasers. For the same light pulse, a laser operating with a higher offset signal, determined by the value of the resistance R_{DC}, would cause the photodiode to saturate prematurely, whereas an excessively low baseline would alter the dynamic response. To maintain comparable baseline levels across the system, this voltage must be kept within a defined window between a minimum of 100 mV and a maximum of 300 mV. Consequently, this requirement translates into a precise allowable range for the resistance R_{DC}.

To minimize the variance among the linearity coefficients m_i of the different lasers, a Python script was implemented to optimize the resistance values (R_{1i}, R_{2i}, R_{3i}) for each channel. Since the slope is defined by Eq. 4.9 and the individual laser efficiencies E_l are fixed, the script adjusts R_{AC} selecting of available discrete resistors.
Because R_{AC} and R_{DC} share part of the resistive network (namely R_2 and R_3), tuning the AC resistance inherently affects the DC contribution and thus the baseline offset voltage. Consequently, the optimization had to simultaneously satisfy both the slope matching and the offset voltage constraints listed in Tab 4.1.

Table 4.1: Hardware and physical constraints applied during the resistor optimization process.

i

Constraint Description	
Linear operating region (Current > Threshold)	$R_{DC} \leq \frac{\Delta V \cdot G}{I_{tr}}$
Acceptable offset voltage range (Baseline)	$100\ \text{mV} \leq V_{offset}(R_{DC}) \leq 300\ \text{mV}$
Signal integrity (Cutoff frequency)	$f_c = \frac{1}{2\pi R_1 C} \approx 5\ \text{kHz}$
Component availability	$R_{1i}, R_{2i}, R_{3i} \in \{\text{Available Lab Resistors}\}$

The script outputs the optimal resistance combination for each laser. The actual slope

achieved after soldering approached the theoretical prediction closely in most cases.

Table 4.2 summarizes the final resistor values selected from the available in the laboratory. A compromise was necessary for a few channels (e.g., laser 221108003), resulting in a baseline voltage exceeding the 300 mV threshold, while still successfully guaranteeing the correct biasing current (I_{base}) and reducing the overall linearity dispersion.

Laser ID	**Baseline**	**Sat.** $V_{\mathbf{in}}$	**R19**	**R17**	**R18**	**NTC**	$R_{\mathbf{DC}}$	$I_{\mathbf{base}}$
(mV)	(V)	(Ω)	(Ω)	(Ω)	(Ω)	(Ω)	(mA)	
221108003	400	2.5	47	10	160	8.5	41.21	10.14
221108007	300	3.1	43	10	150	8.5	38.34	11.16
221108004	230	3.3	43	10	160	8.5	38.96	10.88
220321006	338	2.5	43	10	160	8.5	38.96	10.93
220321012	250	2.3	62	12	160	8.5	48.94	8.58
220321008	170	2.3	62	12	160	8.5	48.94	8.68
220321009	200	2.4	68	12	160	8.5	51.76	8.41

Table 4.2: Complete hardware configuration for each optimized laser channel. The table reports the implemented values for the resistor network, the resulting equivalent R_{DC}, the biasing current I_{base}, and the operational voltage limits (Baseline and Saturation).

The result was a reduction in the dispersion of the linearity coefficients, and as shown in the plot in Fig. 4.13, the standard deviation relative to the slopes $\bar{m}_i$ of the lines decreased from 103 to 87..
All data regarding the resistance values were saved to a JSON file; this file serves as the reference on which the Python code relies during data acquisition, both because it acts as a database containing information on the resistors inserted into the circuit, different for each laser, and because it links each laser to its linearity coefficient.

The receiver circuit

In the final stage of the testbench signal path, the optical pulse emitted by the laser is delivered to the SoF warm receiver board under test, which is read out using an oscilloscope instead of DAPHNE.

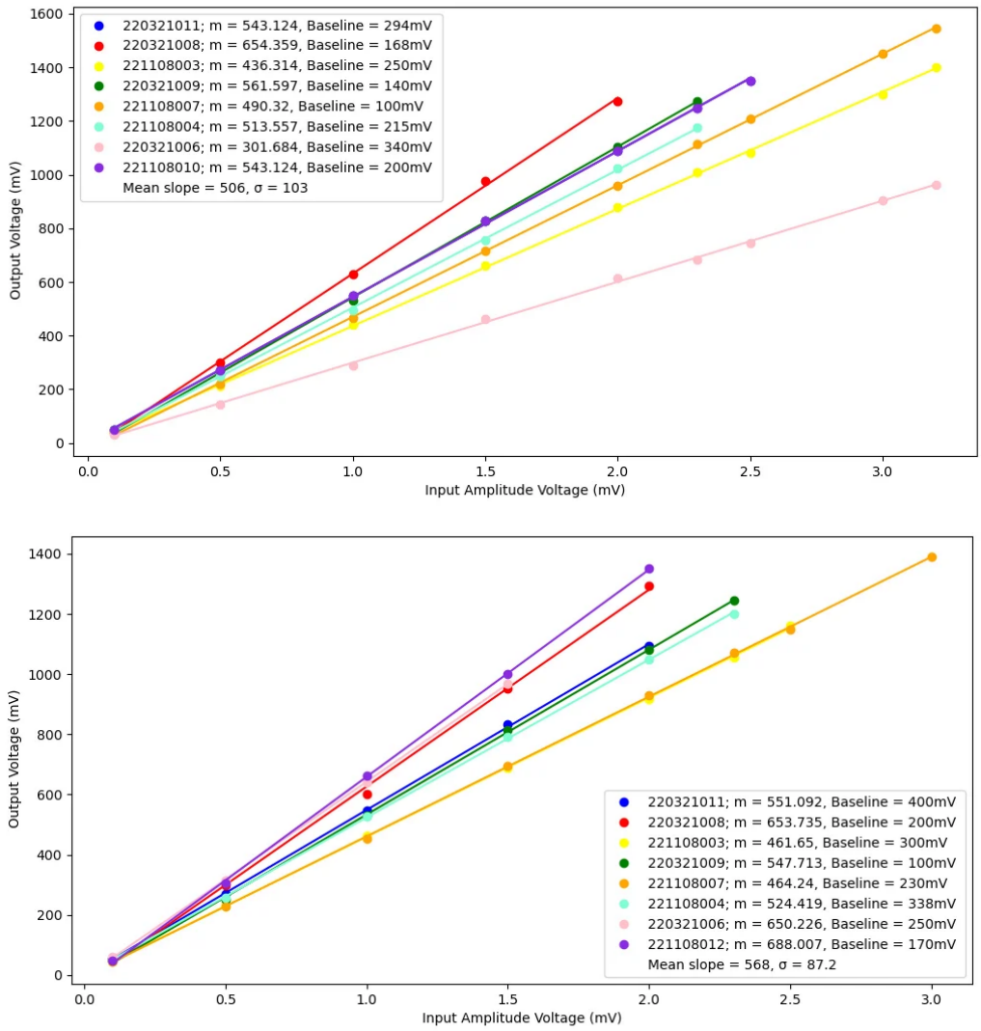


Figure 4.13: Dispersion of the linear coefficients characterizing the response of each channel before and after the optimization process. The legends show the standard deviation of the coefficients $\bar{m}$ drecrease from 103 to 87.2.

Regarding the signal transmission via optical fiber, it was necessary to use eight optical fibers in total to match the eight channels of the receiver board. However, since this number of identical fibers from the same manufacturer was not available in the laboratory, the following combination was used:

- 2x 20m, 62.5um/0.27NA, FC connector, 1.5mm PVDF jacket
- 2x 10m, 62.5um/0.27NA, FC connector, 1.5mm PVDF jacket
- 2x 10m, 62.5um/0.275NA, FC/PC connector, 3.0mm PVC jacket

- 2x 20m, 62.5um/0.275NA, FC/PC connector, 3.0mm PVC jacket

Each fiber is permanently associated with a specific laser and always carries the signal to the same photodiode on the receiver board.

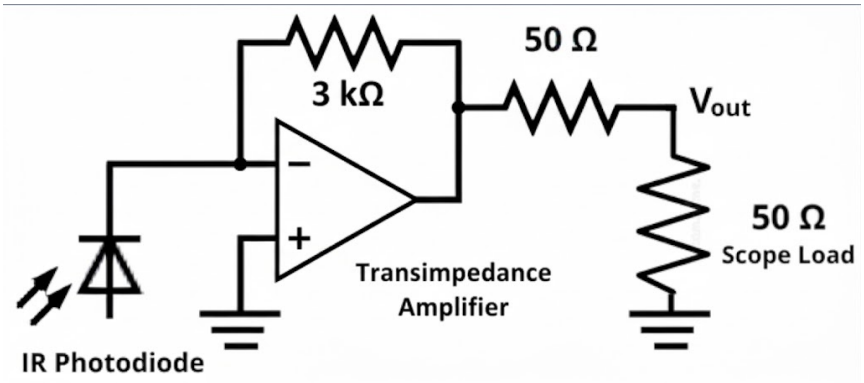


Figure 4.14: Simplified schematic of a single receiver channel. The incoming optical signal is converted to a photocurrent by the IR photodiode and amplified by the transimpedance amplifier (OPA847). The 50 Ω series resistor on the board and the 50 Ω input impedance of the oscilloscope form a 1:2 voltage divider, effectively halving the voltage step amplitude measured at the V_{out} node.

Because the receiver board features a $50\,\Omega$ output adaptation network, and the oscilloscope also presents a $50\,\Omega$ input impedance to the ground, this two resistor in series creates a voltage divider. As a result, the voltage step amplitude actually measured by the oscilloscope is half of the true voltage generated by the amplifier.
This attenuation explains why a factor of 2 must be included in the calculations when converting the measured output voltage (V_{out}) into the corresponding optical power by tracing the signal path backwards, applying the same formula used for the Koheron circuit (Eq. 4.2) in Sec 4.1 .

The output signal observed at the the oscilloscope is a voltage step, with an amplitude proportional to the value set by the function generator, plus an offset generated during the differential amplification stage in the warm transmitter board. The typical signal observed at the oscilloscope is shown in Fig 4.15.
The setup is completed by an eight-output Lemo connector, which, via coaxial cables, transmits the electrical signals from the individual photodiodes directly to the oscilloscope.
The fundamental architecture of the receiver circuit is standard, but several prototype iterations featuring slightly different components (such as different photodiodes or termination resistors) were used during the testbench development.

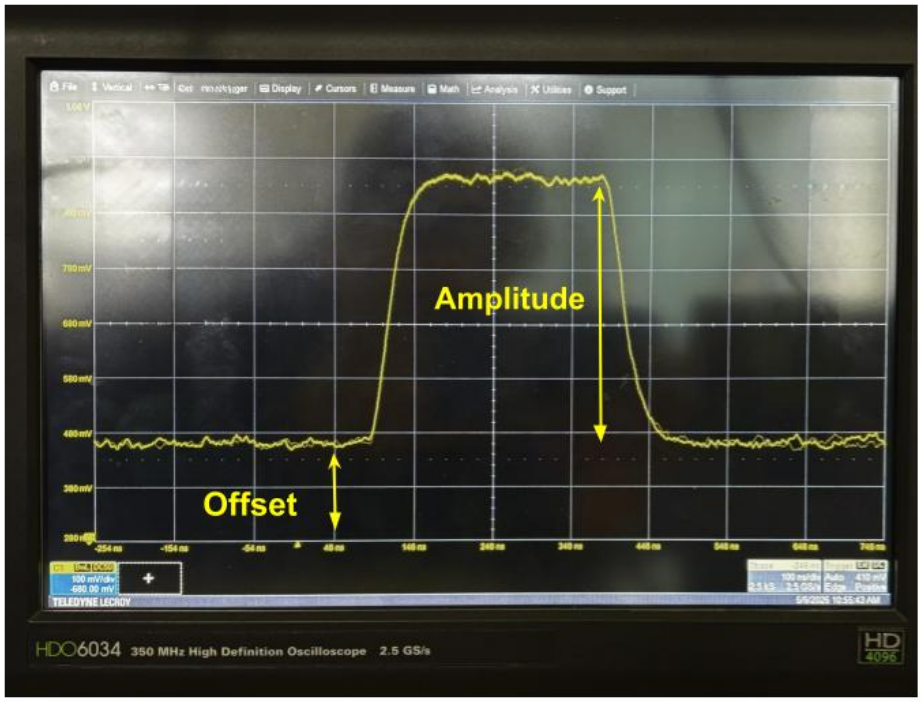


Figure 4.15: Typical voltage step signal seen on the oscilloscope at the output of the receiver board.

A detailed description of these hardware variations and a comprehensive analysis of their performance will be discussed in next sections.

4.2.2 DAQ description

Python code

To automate the data acquisition process, we use a Python script, which I worked on during my internship to improve the data acquisition process. The script interacts with the function generator and sets the amplitude of the voltage step on the function generator for both polarities. The signal is then transmitted to the receiver and finally to the oscilloscope.

At this stage, the script interfaces with the oscilloscope to record the essential parameters for the linearity test: the baseline offset and the signal peak. The actual signal amplitude is then calculated as the difference between these two values.
Furthermore, the code also captures the signal waveform and saves all the values to a text file, so that the data can be analysed at a later stage.

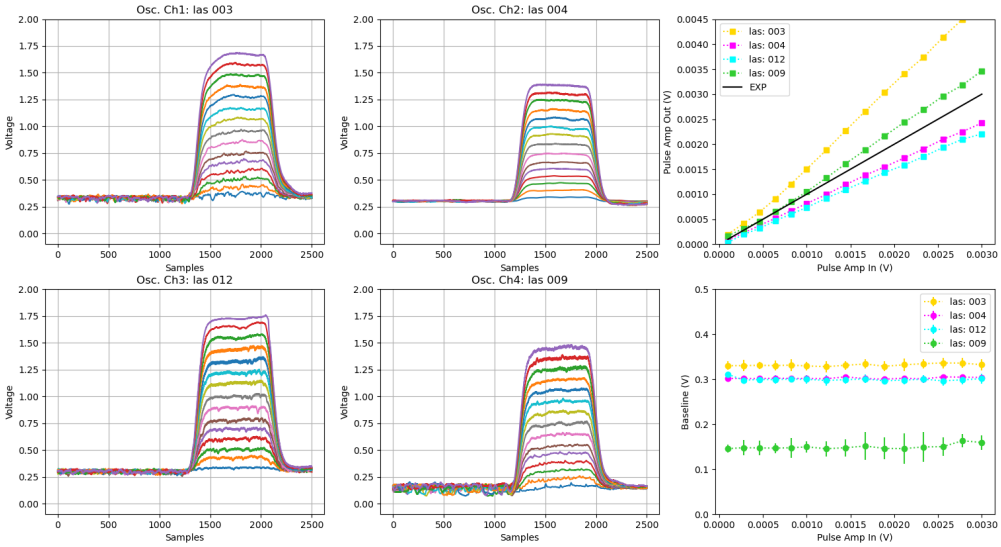


Figure 4.16: Graphical interface displayed during data acquisition. The layout allows for real-time monitoring of the oscilloscope traces across multiple laser channels. The top-right panel generates a plot of the output versus input signal, enabling an immediate visual verification of linearity alongside an automated linear fit. The bottom-right panel monitors the baseline voltage stability.

The code displays iterative linearity graphs during data acquisition,shown in Fig. 4.16 which are very useful for monitoring the process, identifying any issues during data collection and avoiding wasted time. The acquisition concludes by generating a plot of the output signal versus the input signal. This allows for an immediate visual verification of the linearity, while an automated linear fit calculates the proportionality coefficient and its associated error.

Acquisition Time Optimization

As the DAQ process will need to be repeated several times, one of the objectives was to reduce the programme's acquisition time and find the most efficient way to verify the linearity and uniformity of the response. To identify the most time-consuming steps during data acquisition and implement targeted optimizations, the execution time for each operation was systematically measured.

- Configuring the oscilloscope to measure the specific output signal parameters;
- Adjusting the appropriate vertical voltage scale on the instrument.

The initial code caused significant delays by re-evaluating the oscilloscope's voltage scale for every single measurement. We optimized this by introducing a preliminary calibration step: because the system's response is linear, the script now calculates the expected output voltage in advance and adjusts the scale automatically.

This strategy of minimizing redundant commands was extended to all oscilloscope interactions. By configuring the measurement parameters just once at the beginning of the script, rather than clearing and resetting them for every data point, we reduced the total data acquisition time by 50%
Thanks to these optimizations, testing four channels simultaneously now takes 2 minutes of script execution. Including the manual swapping of optical and Lemo cables to test the remaining half, a full 8-channel board is fully characterized in approximately 10 minutes. This efficiency is crucial to meet the testing schedule for the upcoming mass production of 80 boards.

4.2.3 System Stability and Setup Calibration

The mass production of the SoF warm receivers requires a highly reliable testbench. Commissioning and validating this setup is therefore a critical step. During the initial operation of the complete experiment, unexpected structural and dynamic instabilities were observed in the system's response.
This section describes the investigation of these anomalies, specifically the temporal variability of the linearity coefficients, and the automated calibration implemented to guarantee measurement reproducibility.

Variability of the linear coefficient

Once the setup was finalized by permanently soldering the optimized resistors into the laser driver circuits, continuous data acquisition cycles were executed to evaluate the time stability of the system's response. The primary objective was to ensure that the optical signal transmitted to the receiver remained stable in time and exhibited a repeatable response comparable to the pre-calculated coefficients.

The response remains consistent across multiple measurements taken at very close intervals. However, significant temporal fluctuations were observed in both the baseline offset and the response coefficient of the photodiodes.
As can be seen from the graph illustrated in Fig. 4.17, the data show a variation of around

10% from the average, both in terms of the offset variation and the linearity coefficient, with peak-to-peak offset fluctuations reaching up to 30% in specific channels (e.g., Channel 3). These variations exhibited no systematic pattern; adjacent laser in the same laser driver displayed anti-correlated behavior.

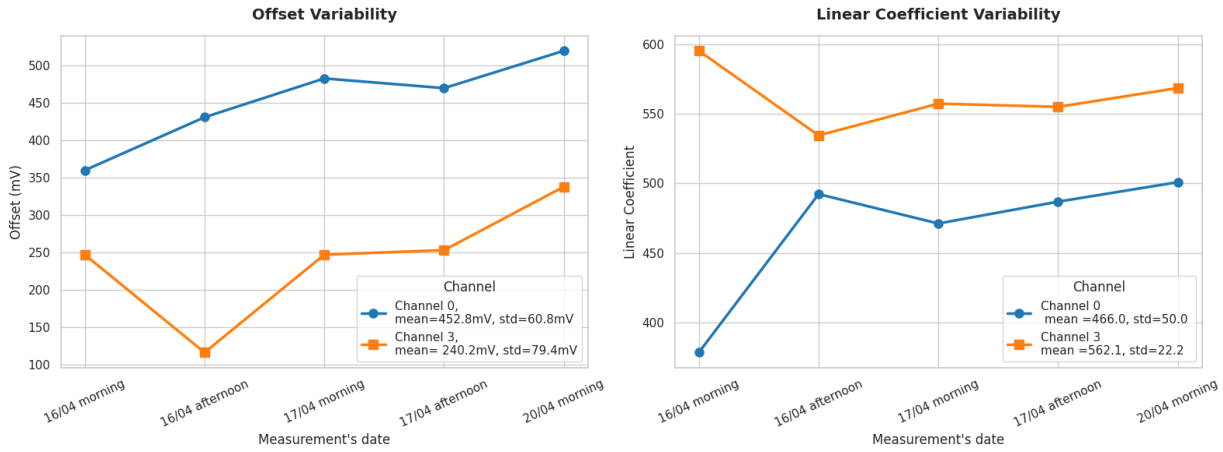


Figure 4.17: The graphs show the variation in the offset value and the linear coefficient during a series of measurements taken at different times. Specifically, two measurements were taken each day—one in the morning and one in the afternoon—for three consecutive days, without making any changes to the experimental setup between one measurement and the next.

To address this issue, an initial diagnostic effort was made to isolate the specific stage of the signal transmission chain responsible for the instability.
Signal conversion anomalies at the receiver were immediately ruled out: swapping the optical fibers and routing the signals into different receiver channels did not alter the measured fluctuations, meaning the anomaly followed the optical input rather than staying with a specific receiver channel. Consequently, the instability was isolated to either the laser diode emission level or the optical coupling between the laser and the fiber.

Initial mitigation efforts focused on the mechanical stabilization of the test bench. All optical fibers and electrical cables were rigidly secured to eliminate tension at the connectors and reduce operator-induced charges.
While these mechanical improvements successfully suppressed short-term, low-amplitude fluctuations—bounding the linearity slope error to approximately 5%—significant long-term drifts persisted between measurements separated by larger time intervals.

For instance, Fig. 4.18 documents a progressive degradation in the optical output of laser 220321012, eventually resulting in a near-zero signal at the receiver.
Interestingly, this drastic emission loss was not permanent; the laser occasionally recovered its initial emission levels, effectively ruling out irreversible hardware damage, such as laser diode burnout.

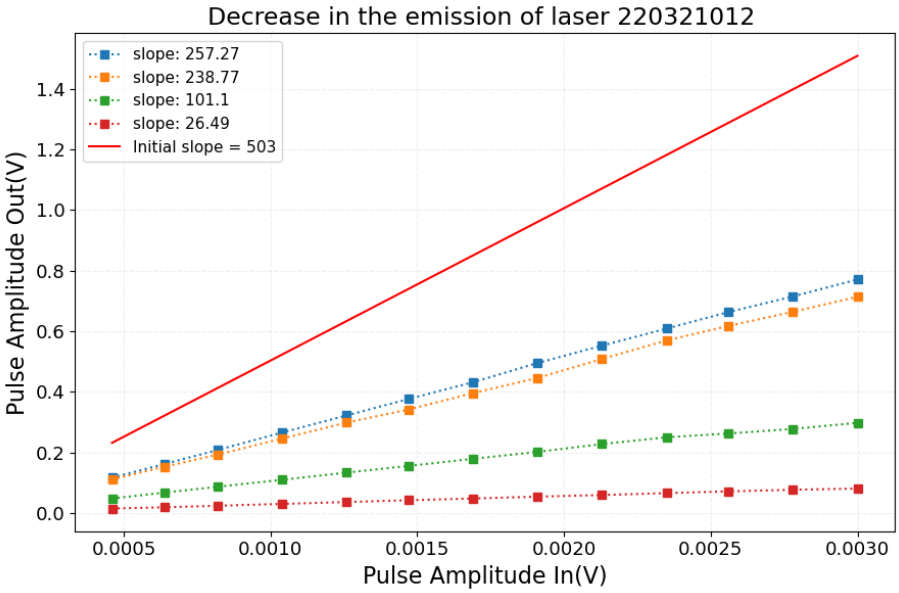


Figure 4.18: The graph shows the continuous decrease in the coefficient that characterizes the receiver's linear response, caused by the sudden decrease in the laser's emitted light. All measurements were taken on the same day.

To further isolate the root cause while awaiting for new focused lasers to arrive, several specific diagnostic tests were conducted:

- Visual and electrical inspection of the laser pin solder joints, performed utilizing a microscope and an MTX 204 digital multimeter, to rule out contact degradation or impedance variations.
- Comparative measurements utilizing optical fibers of varying lengths and core diameters to assess potential transmission losses.
- Direct optical power measurements at the fiber output using a calibrated power meter, definitively confirming that the anomaly originated prior to the receiver board, directly at the optical emitter.

- Simultaneous readout of the laser's internal monitoring photodiode to cross-check the intrinsic emission stability against the externally coupled signal.

Although these comprehensive tests did not definitively identify the fundamental cause of the temporal variability, they successfully pinpointed the issue to the electro-optical conversion and coupling stage.
Structural variations across different laser production batches, such as differences in lens assemblies (e.g., standard versus aspheric lenses), are considered a primary contributing factor to the observed instabilities.

Implementation of a calibration step in the acquisition code

Because it was not possible to eliminate variability in the amount of light reaching the receiver's photodiodes, we decided to implement the possibility to perform a calibration step and determine the reference linearity coefficient each time the setup suffers a modification. In practice, the calibration mode allows for the acquisition of data used solely to calculate the correct linearity coefficient, which can then be used as a reference during the actual channel test, so that any differences or anomalies compared to the expected results can be immediately identified.

When the Python code acquires data in calibration mode, the initial and final voltage values are saved and immediately used to perform a linear fit. The value of the linear coefficient m is saved in the JSON file, under the properties of the laser being used. It is useful to repeat this operation more than once; in fact, during the actual linearity test, the average of all the linear coefficients saved in the JSON file will be calculated, and the reference line for the measurement will be plotted, as shown in Fig. 4.19.

The plot also includes a red interval, which indicates the acceptable range within which we have estimated a deviation from the reference to be acceptable. The interval was calculated by considering two possible fluctuations:

- Random signal fluctuations—due to noise, reflections within the fiber, or other factors—which we estimate do not cause a deviation of more than 5% from the calibration slope, affect the V_{out} values:

$$m^{min/max} = m \pm 2s_m \tag{4.11}$$

$$V_{out}^{min/max} \propto m^{min/max} \tag{4.12}$$

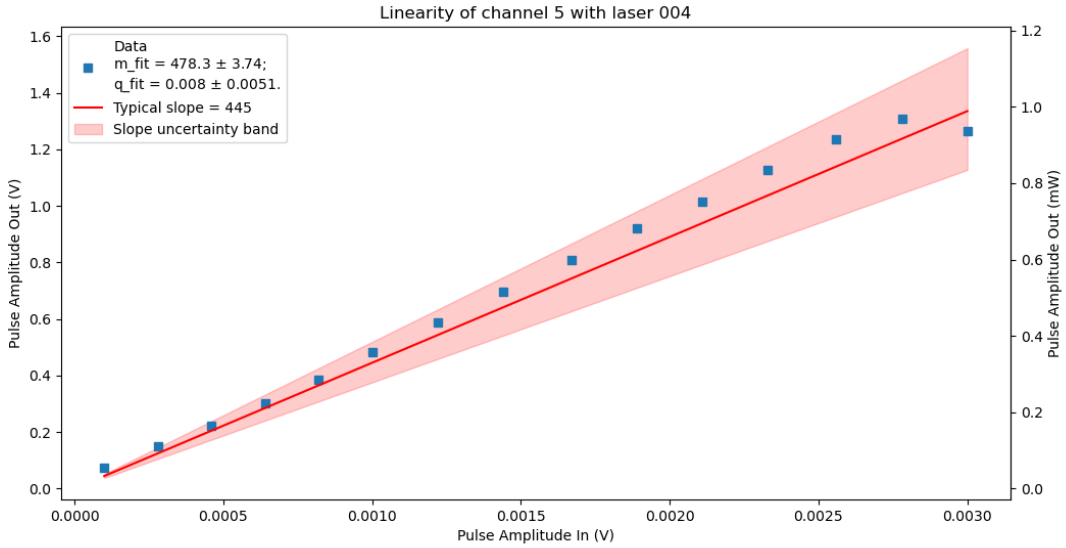


Figure 4.19: Linearity plot displaying the reference line obtained during calibration, along with the acceptable tolerance interval.

- The responsivity of the photodiode may vary from its nominal value according to the manufacturer's specifications; therefore, knowing the maximum and minimum responsivity values given in the specs, we can calculate the range within which V_{out} falls:

$$V_{out}^{max/min} = \frac{PGR_{\lambda}^{max/min}}{2} = V_{out}\frac{R_{\lambda}^{max/min}}{R_{\lambda}} \tag{4.13}$$

Therefore, each value of V_{out} estimated using $\bar{m}_{reference}$ is associated with an interval:

$$V_{out}^{min/max} = \bar{m}V_{in}\frac{R_{\lambda}^{min/max}}{R_{\lambda}}\left[1 \pm \frac{2s_{\bar{m}}}{\bar{m}}\right] \tag{4.14}$$

This not only tests linearity but also provides greater control over the consistent and reliable operation of the setup and the circuit in general. If data is not acquired in calibration mode before data acquisition begins, the reference line remains the last one that was used.

4.3 SoF Warm Receiver Measurement

4.3.1 Receiver's channels performance

Five receiver boards were instrumented with variations of the base circuit shown in Fig. 4.14. Specifically, variations were introduced in the components on the cards, such as the pho-

todiode model and the feedback resistors, which determine the amplifier gain.
The boards were then compared to evaluate if their performance was different, focusing on noise levels and output signal amplitudes. This comparative analysis allows us to understand the hardware characteristics that will guide the design of the final receiver module.

Based on the photodiode model installed, the boards are classified into two categories. The "OSI" boards are equipped with OSI Optoelectronics high-speed InGaAs PIN photodiodes, featuring an active area diameter of 120 μm and a responsivity of ≈ 0.9 A W^{-1} at 1310 nm. Conversely, the "HAMA" boards utilize Lasermate high-speed InGaAs PIN photodiodes with an identical active area diameter of 120 μm and a responsivity of ≈ 0.9 A W^{-1} at 1300 nm. Alongside these variations, different feedback resistors were implemented across the boards to evaluate their impact on the amplifier gain and noise levels.

Further design variations among the boards include the presence or absence of an integrated ADC circuit. Additionally, the boards differ in the physical placement of the 50 Ω output resistor, which constitutes the final component in the signal path before the compensator or the readout oscilloscope.
This layout modification was an attempt to reduce severe signal oscillations that arose due to issues with the integrated ADC when connected to the DAPHNE system. This resistor is placed at a distance from the amplifier. In contrast, test resistor was soldered directly onto the amplifier's output pins.
Table 4.3 summarizes the properties of the five receiver boards used in the laboratory.

Name of the board	PD type	ADC	50 Ohm Resistence
HAMA1	lasermate	yes	default
HAMA5	lasermate	no	on the amplifier
OSI7	OSI	no	default
OSI8	OSI	yes	default
OSI9	OSI	no	default

Table 4.3: Summary of the properties of the receiver boards used in the laboratory during the internship

A primary parameter for characterizing the receiver boards is the linearity of the overall receiver response (encompassing both the photodiode and the readout circuit). When an optical pulse illuminates the active area of the photodiode, the generated photocurrent, I_{PD}, is directly proportional to the incident optical power, P_{in}, governed by the responsivity, R_λ,

of the device:

$$I_{PD} = R_\lambda P_{in}$$

Furthermore, the final output voltage V_{out} is proportional to the photocurrent through the amplifier gain:

$$V_{out} = G_{rec} \times I_{PD} = G_{rec} \times R_\lambda P_{in}$$

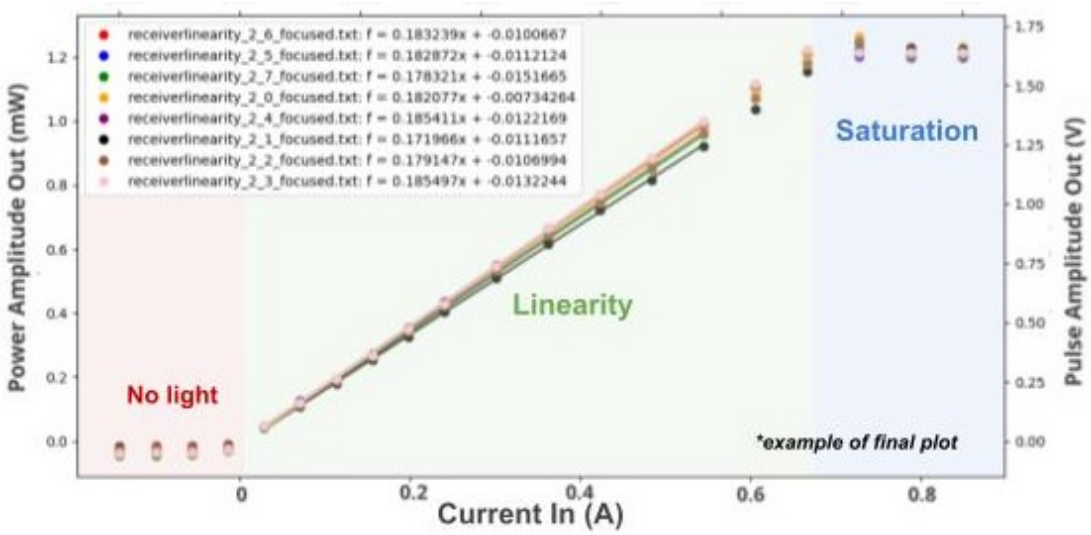


Figure 4.20: The figure shows a linearity plot; the signals used range from -0.5 to 3 mV and cover the entire dynamic range of the photodiode. The photodiode begins to emit only in response to positive input signals, and saturation occurs at an input signal of 2.5 mV. The other axes of the graph show the corresponding values for the laser input current and the photodiode output power.

To ensure that the response is linear from the minimum power required to activate the photodiode right up to an input signal corresponding to saturation, the aim is to use signals that cover the entire dynamic range of the photodiodes. Figure 4.20 shows a linearity plot using input signals that cover the entire operating range of the photodiode.
The signal observed on the oscilloscope at the receiver's output is the sum of the two components descussed in the previous section: the amplitude of the potential step, which depends on the input signal, and the baseline value, which is constant for each amplitude but may depend on other conditions, such as the type of laser that emitted the light pulse.

Receiver saturation occurs at a maximum output voltage of approximately 1.6 V. Since it is not possible to measure the corresponding incident optical power directly at the input, this value is determined analytically using the circuit parameters established previously. By applying Eq. 4.2, which accounts for the photodiode responsivity, the amplifier gain,

and the termination resistance, the saturation voltage is calculated to correspond to an input optical power of approximately 1.2 mW.
To generate the linearity plots, a fixed set of 30 data points is recorded for each measurement, corrisponding to 30 input pulse output. Because the operational limits can vary depending on the specific laser and board configuration, adjusting the input voltage range for each measurement ensures that the 30 acquisition points consistently cover the dynamic range across different test conditions.

Channels linearity

Initially, the linearity of the receiver channels' response is analysed using defocused lasers, comparing it with that of the Koheron receiver, whose operation has already been validated. The defocused lasers exhibit not optimal alignment with the fiber; consequently, for the same driven current, the photodiodes detect a lower amount of light respect the focused laser.
The linearity graphs for all channels of the OSI 7 board are shown in Fig. 4.21 and compared with the response of the Koheron receiver, which uses a 3 kOhm gain.

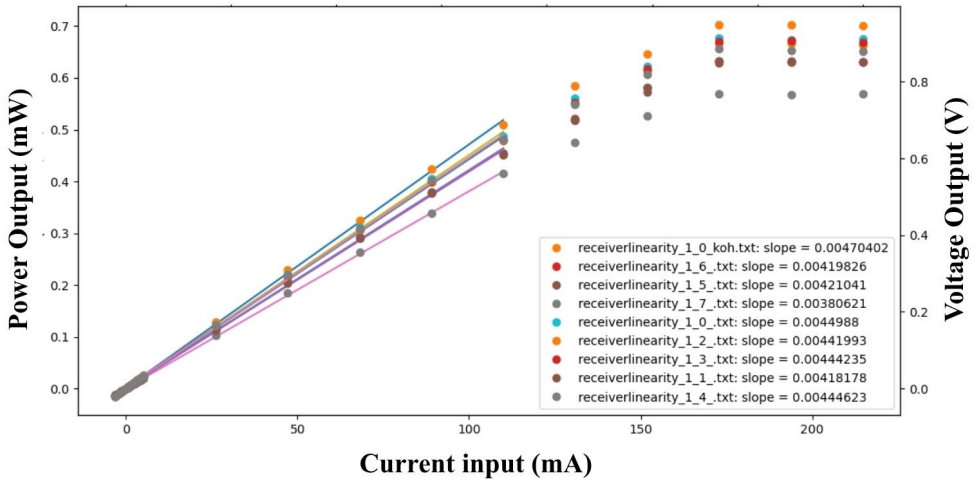


Figure 4.21: Linearity response of the receiver channels tested with defocused lasers. The graph compares the power output of various channels with the Koheron receiver as a function of the input current. Saturation is visible at around 0.8 V on the secondary right axis.

Saturation occurs at an output voltage value measured by the oscilloscope of approximately 0.8 V. This limit is not attributable to receiver saturation, but rather to a component on the transmission board, which saturates due to the excessively high input signal.

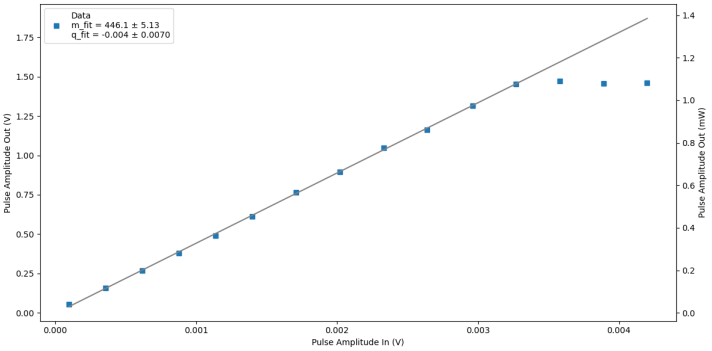
The slopes of the lines were calculated using a linear fit, analytically confirming the linearity of the experimental data that is already visually evident. The values extracted from this fit were subsequently used to calculate the mean and the corresponding standard deviation, yielding: $(4.2755 \pm 7.24) \times 10^{-3}$.
Comparing the mean channel response to that of the Koheron receiver, characterized by a linear coefficient of 4.70402×10^{-3}, reveals a percentage difference of 9.11% .
This result allows us to state that the performance of the receiver channels, tested with the defocused lasers, is fully consistent with that of the Koheron receiver, confirming the test expectations.

Subsequently, we investigated the linear response of the channels using a focused laser, evaluated using a common optical fiber. This configuration enables a controlled comparison of the channel response across different boards under identical initial conditions.
Repeatedly connecting and disconnecting the fiber manually is not practical for a testbench, this approach remains acceptable for these preliminary measurements.

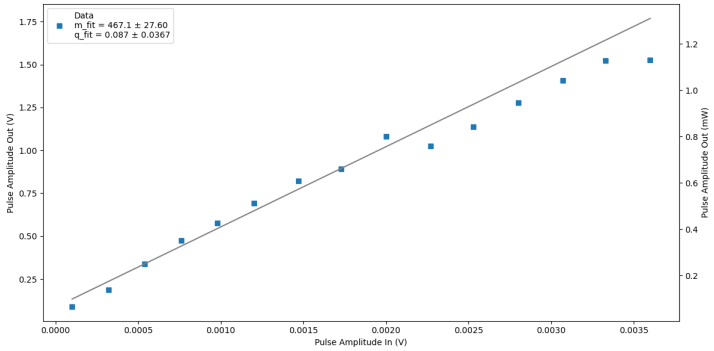
An overview of the linearity results for channel 0 across all receiver boards listed in Table 4.3 is shown in Fig. 4.22. The solid lines represent the best linear fits to the data, with the corresponding equations and fit errors reported in the legends.
While the fit uncertainties remain minimal across all measurements, distinct dispersion patterns are observed: certain boards exhibit data points closely aligned with the linear fit, whereas others display periodic fluctuations around the trend line.

These deviations do not stem from intrinsic non-linearities in the receiver electronics, but rather from measurement artifacts associated with the peak-detection algorithm of the oscilloscope. During acquisition, the oscilloscope measures the maximum of the voltage step. At low amplitudes, a poor signal-to-noise ratio causes noise spikes to be mistaken for the real signal peak, introducing a positive shift that alters the apparent linearity.

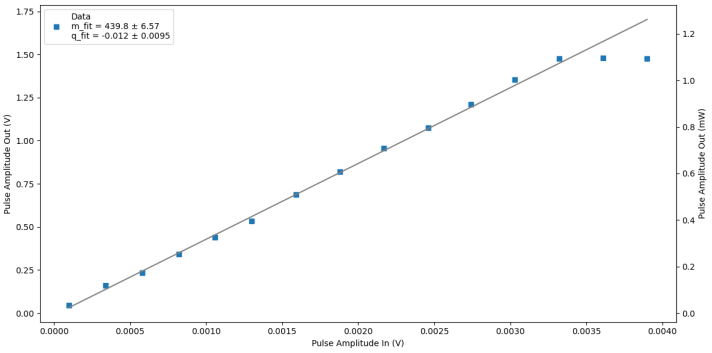
On the noisiest receiver boards, these noise issues impact the data points, indicating that high noise levels can degrade the accuracy of the linear response estimation. Standard boards show reliable behavior, the linearity coefficient m_{fit} calculated via a fit has an error of less than 10% on all boards, even the noisiest ones; but the performance of the noisiest prototypes requires bandwidth filtering before final validation.



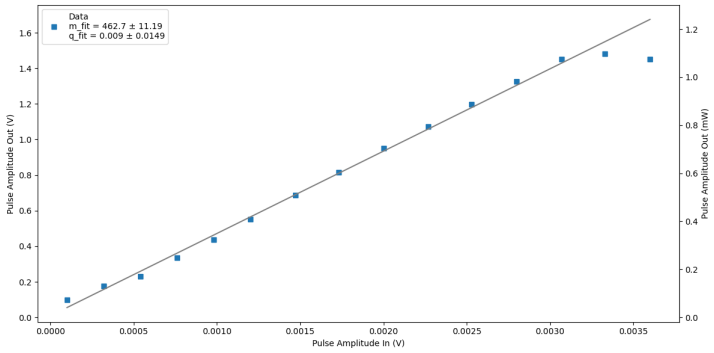
(a) Linearity OSI7



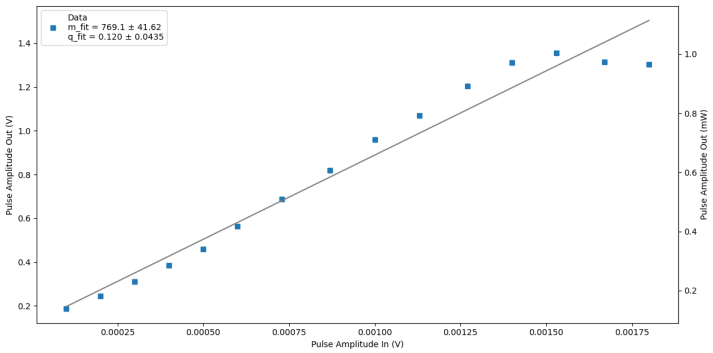
(b) Linearity OSI8



(c) Linearity OSI9



(d) Linearity HAMA1



(e) Linearity HAMA5

Figure 4.22: Comparison of the linearity responses of channel 0 of the receiver across all boards. The grey straight lines represent the best linear fit to the data; the equation of the line is shown in the legend.

Linearity test with compensator

Because the compensator card is specifically designed to counteract the pulse-shaping effects of DAPHNE, connecting it directly to the oscilloscope during the testbench measurements introduces visible signal alterations.
As a result, the compensator alters the voltage step by creating an overshoot at the beginning of the pulse and an undershoot at the end, visible in the comparative waveforms of Fig. 4.23, causing the signal to dip below its normal baseline during the test.
To prevent these distortions from biasing the peak detection, to perform the input pulse profile was optimized: the trailing edge was extended to 150 ns, the pulse width was reduced to 100 ns, and the oscilloscope acquisition delay was increased to 200 ns.

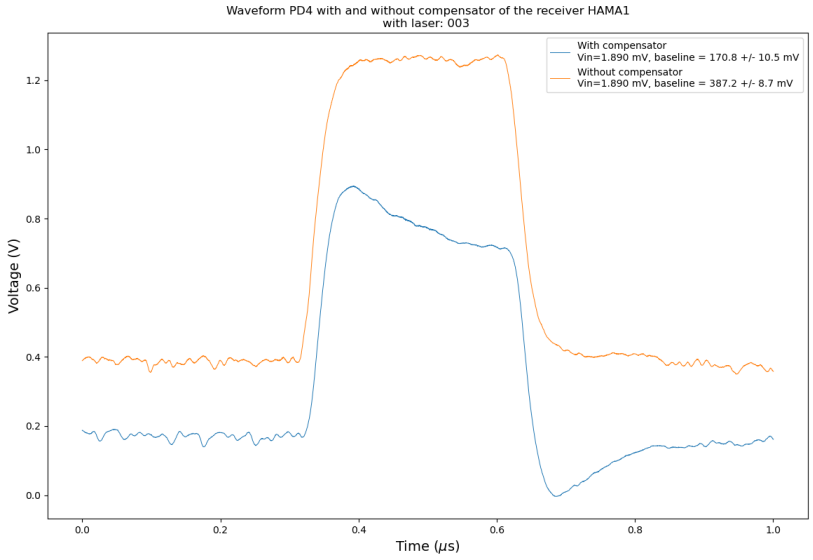


Figure 4.23: Comparison of receiver waveforms acquired without the compensator (left) and with the compensator card (right), highlighting the characteristic undershoot and overshoot phenomena at room temperature.

To verify that response is still linear, a dedicated ”compensator” operating mode was implemented in the automated Python script for DAQ.
By passing a specific command-line argument, this mode activates at the end of the data acquisition: when the graphical user interface displays the new linearity plot, it automatically overlays the reference straight line obtained without the compensator. This allows for an immediate, side-by-side comparison, as shown in Fig.4.24.

Ultimately, despite the waveform shaping introduced by the card, from the linear fit results an error of less than 10%, and a difference of 10% between the slope extimated from the linear fit with and without the compensator. These values confirm the system maintains a linear behavior.

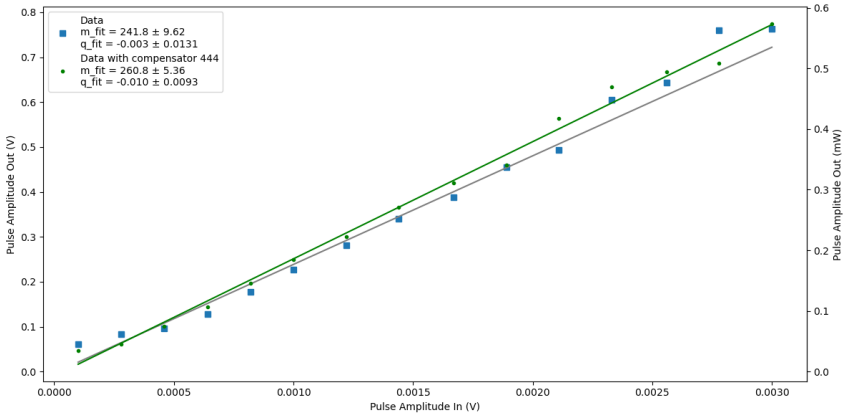


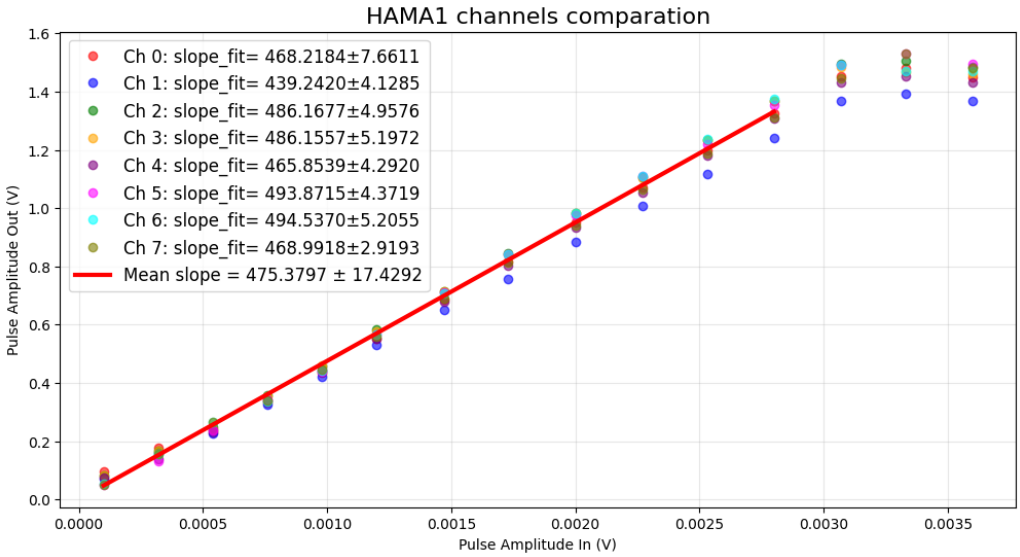
Figure 4.24: Linearity fit comparison of the pulse amplitude output as a function of the input amplitude, comparing standard data (blue squares) with the data with the CC08 compensator (green dots) and their respective linear fits.

Channel dispersion

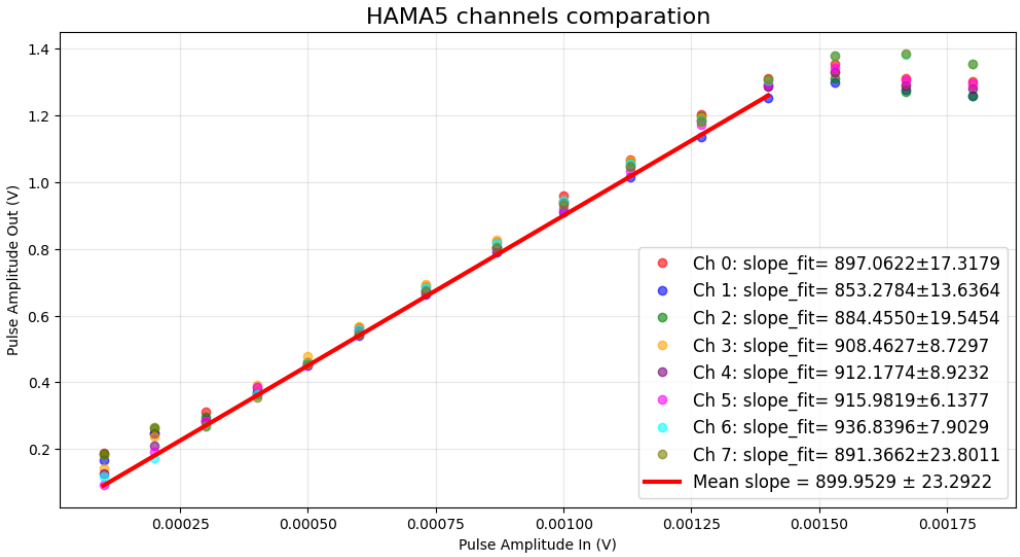
Beyond evaluating the linearity of individual channels, it is also important to compare the response uniformity across different channels within the same receiver board. To ensure an unbiased comparison, all measurements were performed under identical test conditions, utilizing the same laser, the same optical fiber, and the same receiver channel.

The possible dispersion is driven by a combination of factors: the responsivity range of the individual photodiodes and the additional contributions from circuit component tolerances.
Ideally, this overall dispersion should match the expected photodiode range. Although these variations affect individual channel responses, they do not pose a limitation for the final experiment, because during full-scale production the responsivity of each individual photodiode will be known and accounted for.

To highlight any possible differences between channels, we plotted the data from all channels on the same graph. Figure 4.25 presents the results for the HAMA1 and HAMA5



(a) Linearity HAMA5



(b) Linearity HAMA1

Figure 4.25: Comparison of the linearity response of two different receiver boards, HAMA1 (a) and HAMA5 (b). The solid line represents the average linear trend across all channels for each board. While the intra-board uniformity is high, the absolute value of the average linearity coefficient (reported in the legends) varies significantly between the two receivers, increasing from approximately 475 for HAMA1 to 899 for HAMA5

boards, including the linear fits applied to the data. The legend reports the mean of the linear coefficients extracted from the fits, utilizing the standard deviation as the error estimate. This mean value defines the slope of the reference line (shown in red), which provides an immediate visual representation of the receiver's overall response and facilitates comparative analysis between different boards.

The graphs show that the channels on the same board behave very similarly. This consistency was found across all the tested boards.
Measurements were conducted using both focused and defocused laser configurations. Figure 4.26 illustrates the dispersion of the linearity coefficients across the channels under the defocused laser setup, whose emission characteristics were previously detailed in Figure 4.21. From this distribution, the linearity coefficients exhibit a coefficient of variation of 5.35%

In contrast, the average linearity coefficient changes significantly between different receiver boards, for example the slope calculated with the fit increases from 475 in HAMA1 to 899 in HAMA5, as shown in Fig. 4.25. However, during our laboratory tests, these hardware differences required us to adjust the acquisition parameters for each board (for example, the voltage offset).

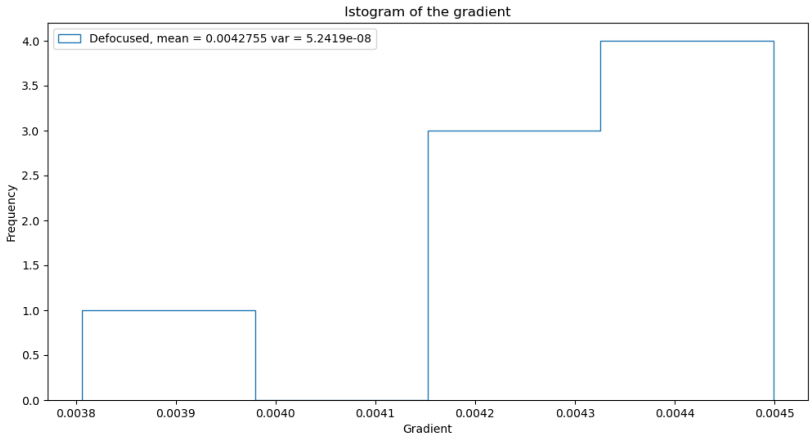


Figure 4.26: Histogram of the gradients across the evaluated channels in OSI7 receiver board. The distribution demonstrates the high uniformity of the intra-board response.

Crosstalk Evaluation

The crosstalk between channels of the receiver board was evaluated to quantify inter-channel interference. Crosstalk manifests as an additional signal component induced on a given channel by activity in adjacent channels. Given the eight-channel architecture of the receiver board, verifying that this mutual coupling does not distort signal amplitude measurements is essential.
To isolate the crosstalk contribution, the photodiode of the channel under analysis was disconnected from the optical fiber to prevent any direct light input, while signals were applied to the neighboring channels.

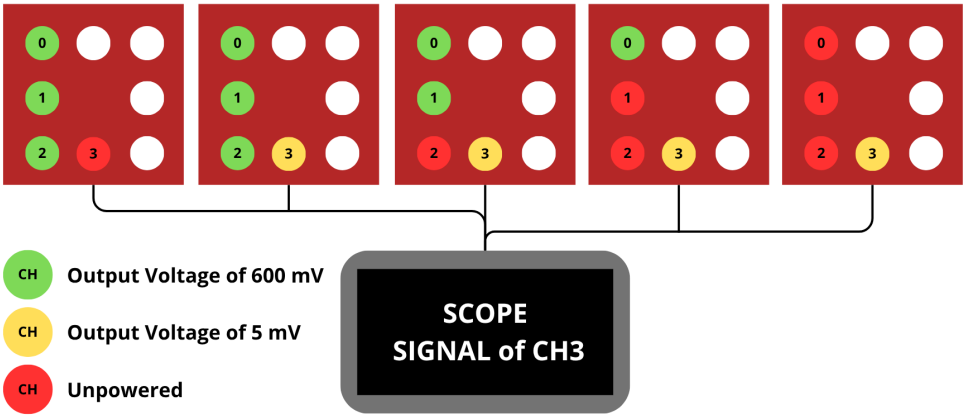


Figure 4.27: Schematic representation of the crosstalk measurement procedure.

For example, the crosstalk was evaluated on channel 3 (utilizing photodiode 23, with channels numbered from 20 to 27). The adjacent channels (ch0, ch1, and ch2) were driven with an input signal V_{in} of 1.7 mV, producing an output voltage step between 600 and 800 mV on the oscilloscope for each channel, which corresponds to approximately half of the receiver's dynamic range, a schematic is shown in Fig 4.27. The input signal was configured with a pulse width of 300 ns, a leading edge of 100 ns, and a trailing edge of 250 ns.
The residual signal on ch3 was then monitored while the inputs of the neighboring channels were removed sequentially, revealing a maximum crosstalk impact of less than 1 mV per channel, as illustrated in Fig. 4.28. To put this into perspective under standard operational conditions, the minimum measured output amplitude—representing the first data point of our linearity test—is typically around 100 mV. Consequently, a maximum crosstalk contribution of 1 mV translates to an error of $\leq 1\%$. For the signal output we obtain in the linearity test, the crosstalk effect doesn't affect the final linearity evaluation.

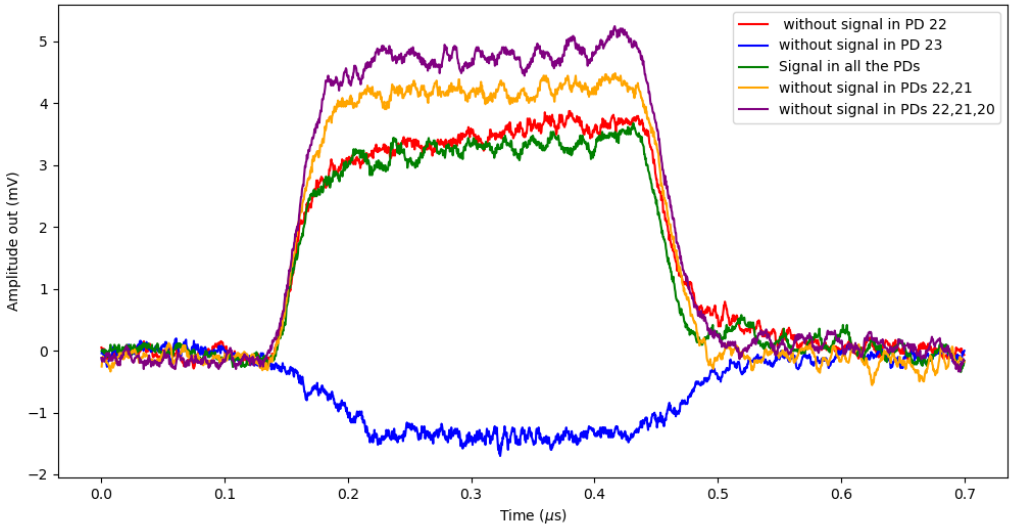


Figure 4.28: Effect of crosstalk in the channel under test as the number of neighbouring channels through which the signal passes increases. The negative signal obtained in the channel under test when it is not the only one not receiving a signal is shown in blue.

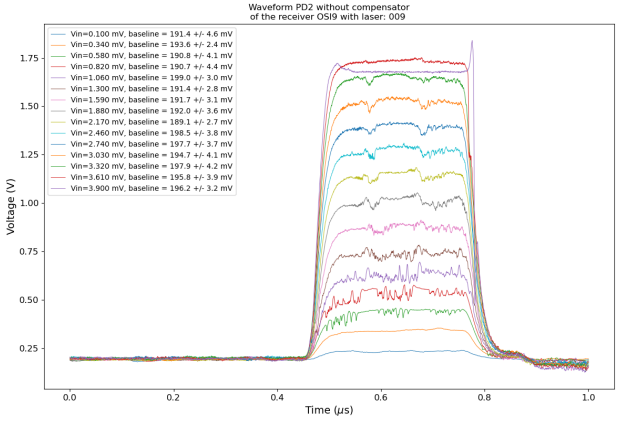
Waveform Analysis

A crucial aspect of the offline data analysis is determining the signal amplitude with uniformity across all the channels. While the oscilloscope provides automated peak detection functions, the measure of the parameters is susceptible to noise and signal fluctuations.

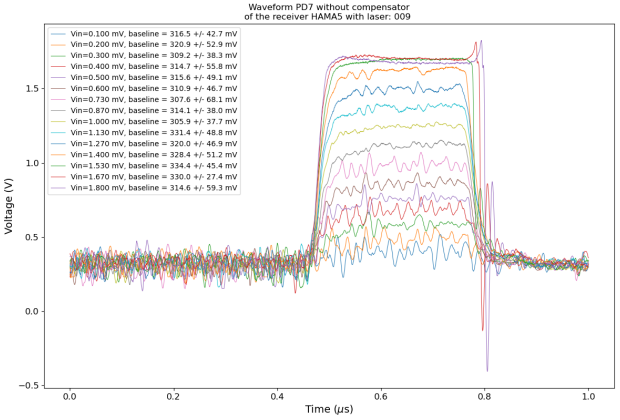
As illustrated in the waveform plots Fig. 4.22, the measurements are frequently affected by different types of noise. There are two possible sources: setup artifacts and intrinsic circuit issues. To overcome these problems and establish a DAQ method that doesn't require modifying the code for each specific channel, we evaluated the signal amplitudes by saving the full waveform data during the DAQ.

The waveform of the signal read on the oscilloscope can be observed, on channel 2 in OSI9 and channel 7 for HAMA5 and OSI7, for different input signal amplitudes. Both high-frequency and low-frequency noise complicate the oscilloscope's automatic peak detection functions and cause the acquired data to deviate from the linearity curves.

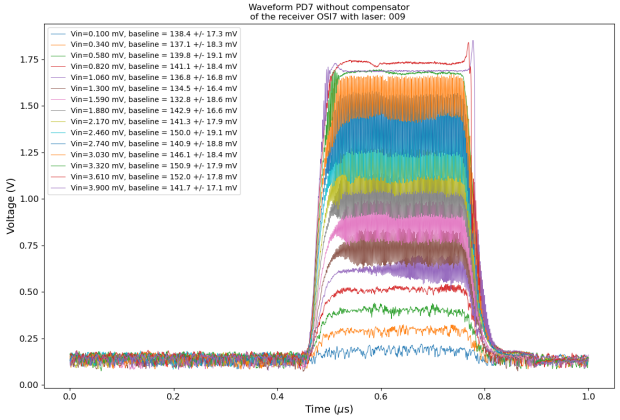
Frequency analysis of signal oscillations helps identify the noise source. In this cases, noise can originate from optical reflections within the fiber. By measuring the oscillation frequency and knowing the speed of light propagation v within the optical fiber, the distance L corresponding to these reflections can be calculated as



(a) Waveform OSI9



(b) Wavefom HAMA5



(c) Waveform OSI7

Figure 4.29: Waveform of the signal detected by the oscilloscope, as the input amplitude varies, across the outputs of three different receiver boards.

$$f = \frac{v}{2L} \tag{4.15}$$

A frequency of 10 MHz corresponds to a reflection length of 10 m, matching the physical length of the optical fiber used in the setup. Consequently, the 10 MHz noise component observed in the OSI9 board waveform is attributed to signal reflections along the fiber.

Since this is strictly an issue related to the test setup, its impact on the amplitude measurement is minimal. The ultra-high-frequency noise observed in the OSI7 board introduces measurable deviations. The frequency of this noise approaches the 350 MHz bandwidth limit of the oscilloscope, suggesting an origin within the amplification stage. This high-frequency component affects the linearity measurements through two mechanisms. First, it interferes with the automatic peak detection, causing a positive shift in the recorded voltage amplitude. Second, this detection error is not systematic across all input signal values, resulting in the misalignment of data points on the linearity plot.

Part of this instability, visible as high-frequency oscillations, is related to the ADC circuit, which was mentioned at the beginning of the section. Some cards had this ADC removed because of issues related to the DAPHNE system. However, the cards still exhibited severe signal oscillations. To understand and solve this issue, several measurements were performed. One of the tests involved moving the 50 Ω output resistor directly onto the amplifier's pins in an attempt to suppress the interference.

Unfortunately, this solution did not work, and the oscillations persisted. The waveform plots in Fig. 4.29 were produced precisely to investigate this phenomenon.
While high-frequency noise must be minimized in future board iterations, its impact on current measurements is mitigated by restricting the input bandwidth of the oscilloscope. This procedure is consistent with the final readout architecture, as the DAPHNE analog front-end incorporates a third-order low-pass filter, with a selectable cut-off frequency between 10 and 30 MHz, to suppress high-frequency noise prior to signal digitization.

4.4 Results of the Measurements

The tests conducted successfully validated the components of the optical acquisition chain. The main results obtained during the measurements are summarized below:

- The laser diodes for the transmitter tested at cryogenic temperatures shows a linear emission profile, validating their use inside the cryostat.
- The measurements confirmed a linear response across the entire dynamic range of the photodiodes. Furthermore, uniformity response was observed among the channels belonging to the same receiver board.
- Crosstalk between adjacent channels proved a negligible effect. The frequency analysis of the waveforms allowed to separate specific sources of instrumental noise, such as internal reflections in the optical fibers and high-frequency noise originating from the amplification stage.
- A primary objective of evaluating the different receiver boards was to compare the OSI and HAMA photodiodes to verify if their performance was identical.

In conclusion, these measurements prove that the fundamental performance of the OSI and HAMA photodiodes is equivalent, meaning they can be used interchangeably for the experiment.

Conclusion

The DUNE experiment represents an ambitious scientific and technological challenge in contemporary physics. The experiment aims to study the oscillation phenomenon using an intense muon neutrino (ν_μ) beam produced by an accelerator, in order to measure its transition into electron neutrinos (ν_e) with unprecedented sensitivity. These precision measurements are designed to determine the oscillation parameters that are still affected by uncertainties, allowing for a definitive resolution of the mass hierarchy unknown (normal or inverted) and the measurement of the CP phase, a crucial step to ascertain any CP symmetry violation in the leptonic sector.

By employing large-scale Liquid Argon Time Projection Chamber technology, the project achieves highly sensitive measurements of neutrino oscillations.
For this detector to operate effectively, the charge collection system must be complemented by an efficient Photon Detection System capable of capturing the scintillation light produced in the liquid argon. Within this framework, the work presented in this thesis addresses one of the complex engineering challenges of the Far Detector's Vertical Drift module: the extraction of signals from the X-ARAPUCA optical detectors positioned directly on the surface of the ultra-high voltage cathode.
Operating in an environment at -300 kV makes the use of traditional conductive cables impossible, necessitating the implementation of the Signal-over-Fiber technology. This solution is a novel approach for such applications and requires development and validation.

My work within the DUNE group at the APC laboratory focused on the preparation and optimization of this SoF electronics ahead of its future mass production. I carried out dedicated experimental measurements designed to build and enhance the Quality Assurance and Quality Control (QA/QC) protocols.
A crucial part of this effort involved the validation of a new batch of lasers for the cold transmission electronics. By testing these components at cryogenic temperatures, I con-

firmed that their emission profile complies with production standards and maintains a linear behavior even when immersed in liquid nitrogen.

Furthermore, I improved the testbench setup that will be used to ensure the quality of the warm receiver electronics during mass production.
These upgrades were implemented across several fronts. Mechanically, I improved the physical stability of the setup by firmly fixing all the components in place. This helped to reduce random signal fluctuations and background noise.
I optimized the data acquisition scripts. This reduced the testing time required for each board and introduced new features that allow for real-time monitoring of the results, enabling an immediate comparison of the performance across different channels against reference calibration values.
Ultimately, I performed a tailored adjustment of the resistor values on the laser adapter card, equalizing the optical light output across all channels for a given voltage input.

The optimized setup was utilized to test several receiver prototype boards currently under evaluation in the laboratory.
Through data acquisition and offline analysis, we were able to draw important conclusions for the final electronic design.
First, we demonstrated that the performance provided by two different photodiode vendors (OSI and HAMA) is equivalent, thus, one can opt for the less expensive option. Additionally, the acquired data and noise analysis helped the team better understand certain circuit instabilities. We verified that high-frequency oscillations were triggered by the removal of the ADC from the circuit.
We tested several proposed modifications to mitigate this noise, such as changing the value and the placement of the output resistor. Although these physical corrections did not resolve the issue they provided useful diagnostic insights to prevent such issues in future iterations of the board.

Ultimately, the automated testbench developed in this work establishes a robust evaluation procedure for the SoF electronics, representing a necessary step toward the assembly of the Vertical Drift module, bringing the DUNE experiment one step closer to achieving its fundamental physics goals.

Bibliography

[1] D. Vignaud, M. Cribier, and J. Dumarchez. History of the neutrino, May 2019.

[2] H. Bethe and R. Peierls. The 'neutrino'. Nature, 133:532, 1934.

[3] F. Reines and C. L. Cowan. Detection of the free neutrino. Phys. Rev., 92:830–831, Nov 1953.

[4] C. L. Cowan, F. Reines, F. B. Harrison, H. W. Kruse, and A. D. McGuire. Detection of the free neutrino: a confirmation. Science, 124(3212):103–104, 1956.

[5] M. Goldhaber, L. Grodzins, and A. W. Sunyar. Helicity of neutrinos. Physical Review, 109:1015–1017, Feb 1958.

[6] C. S. Wu, E. Ambler, R. W. Hayward, D. D. Hoppes, and R. P. Hudson. Experimental test of parity conservation in beta decay. Phys. Rev., 105:1413–1415, 1957.

[7] F. Terranova. A Modern Primer in Particle and Nuclear Physics. Oxford University Press, 2021. Chapter 10, Sections 10.5-10.7.

[8] G. Danby, J-M. Gaillard, K. Goulianos, L. M. Lederman, N. Mistry, M. Schwartz, and J. Steinberger. Observation of high-energy neutrino reactions and the existence of two kinds of neutrinos. Phys. Rev. Lett., 9:36–44, Jul 1962.

[9] M. L. Perl et al. Evidence for anomalous lepton production in $e^+ - e^-$ annihilation. Phys. Rev. Lett., 35:1489–1492, 1975.

[10] F.J. Hasert et al. Observation of neutrino-like interactions without muon or electron in the gargamelle neutrino experiment. Physics Letters B, 46(1):138–140, 1973.

[11] ALEPH, DELPHI, L3, OPAL, SLD Collaborations, LEP Electroweak Working Group. Precision electroweak measurements on the z resonance. Physics Reports, 427(5-6):257–454, 2006.

[12] S. Aoki et al. DsTau: Study of tau neutrino production with 400 GeV protons from the CERN-SPS. JHEP, 01:033, 2020.

[13] A.C. Philips. The Physics of Stars. John Wiley & Sons, 1999. Chapter 6.

[14] G. Bendiscioli. Fenomeni Radioattivi. Springer, 2013. Chapter 12, Section 5.

[15] Cathryn Carson. The peculiar notion of exchange forces—ii: From nuclear forces to qed, 1929–1950. Studies in History and Philosophy of Science Part B: Studies in History and Philosophy of Modern Physics, 27(1):99–131, 1996.

[16] Q. R. Ahmad et al. Measurement of the rate of $\nu_e + d \rightarrow p + p + e^-$ interactions produced by ^8b solar neutrinos at the sudbury neutrino observatory. Phys. Rev. Lett., 87:071301, 2001.

[17] Y. Fukuda, T. Hayakawa, E. Ichihara, et al. Evidence for oscillation of atmospheric neutrinos. Physical Review Letters, 81(8):1562–1567, August 1998.

[18] M Ambrosio, R Antolini, G Auriemma, D Bakari, A Baldini, GC Barbarino, BC Barish, G Battistoni, Y Becherini, R Bellotti, et al. Measurement of the atmospheric neutrino-induced upgoing muon flux using macro. Physics Letters B, 434(3-4):451–457, 1998.

[19] WWM Allison, GJ Alner, DS Ayres, WL Barrett, C Bode, PM Border, CB Brooks, JH Cobb, DJA Cockerill, RJ Cotton, et al. The atmospheric neutrino flavor ratio from a 3.9 fiducial kiloton-year exposure of soudan 2. Physics Letters B, 449(1-2):137–144, 1999.

[20] M. H. Ahn, S. Aoki, H. Bhang, et al. Indications of neutrino oscillation in a 250 km long-baseline experiment. Physical Review Letters, 90(4), January 2003.

[21] K Hirata, T Kajita, M Koshiba, M Nakahata, Y Oyama, N Sato, A Suzuki, M Takita, Y Totsuka, T Kifune, et al. Observation of a neutrino burst from the supernova sn1987a. Physical Review Letters, 58(14):1490–1493, 1987.

[22] RM Bionta, G Blewitt, CB Bratton, D Casper, A Ciocio, R Claus, B Cortez, M Crouch, ST Dye, S Errede, et al. Observation of a neutrino burst in coincidence with supernova 1987a in the large magellanic cloud. Physical Review Letters, 58(14):1494–1496, 1987.

[23] Carlo Giunti and Chung W. Kim. Fundamentals of Neutrino Physics and Astrophysics. Oxford University Press, 2007.

[24] Aartsen, M. G. and others. Evidence for High-Energy Extraterrestrial Neutrinos at the IceCube Detector. Science, 342:1242856, 2013.

[25] Sudeshna Ganguly. Accelerator neutrinos. Fermilab Engineers' Retreat Presentation (FERMILAB-SLIDES-25-0024-AD), 2025.

[26] M. Tanabashi et al. Review of particle physics. Phys. Rev. D, 98:030001, 2018.

[27] S. Abe et al. Precision Measurement of Neutrino Oscillation Parameters with KamLAND. Phys. Rev. Lett., 100:221803, 2008.

[28] Y. Ashie et al. A Measurement of Atmospheric Neutrino Oscillation Parameters by Super-Kamiokande I. Phys. Rev. D, 71:112005, 2005.

[29] MH Ahn, D Aston, S Aoki, H Bhang, S Boyd, D Casper, JH Choi, S Fukuda, Y Fukuda, A Gando, et al. Measurement of neutrino oscillation by the k2k experiment. Physical Review D, 74(7):072003, 2006.

[30] An, F. P. and others. Observation of Electron-Antineutrino Disappearance at Daya Bay. Phys. Rev. Lett., 108:171803, 2012.

[31] Ahn, J. K. and others. Observation of Reactor Electron Antineutrino Disappearance in the RENO Experiment. Phys. Rev. Lett., 108:191802, 2012.

[32] Abe, Y. and others. Indication of Reactor $\bar{\nu}_e$ Disappearance in the Double Chooz Experiment. Phys. Rev. Lett., 108:131801, 2012.

[33] Abe, K. and others. Indication of Electron Neutrino Appearance from an Accelerator-Produced Off-Axis Muon Neutrino Beam. Phys. Rev. Lett., 107:041801, 2011.

[34] M. C. Gonzalez-Garcia and Yosef Nir. Neutrino masses and mixing: Evidence and implications. Rev. Mod. Phys., 75:345–402, 2003.

[35] P. De Bernardis et al. Introduzione alla fisica dei neutrini. Ithaca: Viaggio nella Scienza, 2014.

[36] KATRIN Collaboration, M. Aker, et al. Direct neutrino-mass measurement with sub-electronvolt sensitivity. Nature Physics, 18:160–166, 2022.

[37] A. Aguilar et al. Evidence for neutrino oscillations from the observation of $\bar{\nu}_e$ appearance in a $\bar{\nu}_\mu$ beam. Phys. Rev. D, 64:112007, 2001.

[38] A. A. Aguilar-Arevalo et al. Significant excess of electronlike events in the miniboone short-baseline neutrino experiment. Phys. Rev. Lett., 121:221801, 2018.

[39] Babak Abi et al. Deep Underground Neutrino Experiment (DUNE), Far Detector Technical Design Report, Volume I Introduction to DUNE. JINST, 15(08):T08008, 2020.

[40] R. Acciarri et al. Long-Baseline Neutrino Facility (LBNF) and Deep Underground Neutrino Experiment (DUNE) Conceptual Design Report, Volume 1: The LBNF and DUNE Projects. 2016.

[41] Matteo Galli. Investigating Atmospheric Neutrinos and Photon Detection Readout in the Deep U
Thèse de doctorat, Université Paris Cité, 2026.

[42] Camille Sironneau. Sensibilité à l'existence des neutrinos stériles par le biais des neutrinos atmosp
Thèse de doctorat, Université Paris Cité, 2025. HAL Id: tel-05497877.

[43] Adrian-Martinez, S. and others. Letter of intent for KM3NeT 2.0. Journal of Physics G: Nuclear and Particle Physics, 43(8):084001, 2016.

[44] Rubbia, C. and others. Underground operation of the ICARUS T600 LAr-TPC: first results. Journal of Instrumentation, 6(07):P07011, 2011.

[45] Acciarri, R. and others. Design and construction of the MicroBooNE detector. Journal of Instrumentation, 12(02):P02017, 2017.

[46] Babak Abi et al. Deep Underground Neutrino Experiment (DUNE), Far Detector Technical Design Report, Volume II: DUNE Physics. 2020.

[47] PIP-II Collaboration. Proton improvement plan-ii final design report. Technical Report FERMILAB-DESIGN-2021-01, Fermi National Accelerator Lab. (FNAL), Batavia, IL (United States), 2021.

[48] J. Alvaresetto et al. DUNE Near Detector Conceptual Design Report. Instruments, 5(4):31, 2021.

[49] DUNE Collaboration. DUNE-PRISM: Reducing neutrino interaction model dependence with a movable neutrino detector. arXiv preprint arXiv:2501.14811, 2025.

[50] Carlo Rubbia. The Liquid-Argon Time Projection Chamber: A New Concept for Neutrino Detectors. Technical Report CERN-EP-INT-77-8, CERN, 1977.

[51] B. Abi et al. Deep underground neutrino experiment (dune), far detector technical design report, volume iv: Far detector single-phase technology. Journal of Instrumentation, 15(08):T08010, aug 2020.

[52] Abud, A. Abed and others. Design, construction and operation of the ProtoDUNE-DP liquid argon TPC. JINST, 17(01):P01005, 2022.

[53] Abi, B. and others. First results on ProtoDUNE-SP liquid argon time projection chamber performance from a beam test at the CERN Neutrino Platform. JINST, 15(12):P12004, 2020.

[54] Ettore Segreto. Properties of liquid argon scintillation light emission. Physical Review D, 103(4), 2021.

[55] H. V. Souza et al. Liquid argon characterization of the X-ARAPUCA with alpha particles, gamma rays and cosmic muons. Journal of Instrumentation, 16(11):P11002, 2021.

[56] M. Babicz, S. Bordoni, A. Fava, U. Kose, M. Nessi, F. Pietropaolo, G. Raselli, F. Resnati, M. Rossella, P. Sala, F. Stocker, and A. Zani. A measurement of the group velocity of scintillation light in liquid argon. Journal of Instrumentation, 15(09):P09009, Sep 2020.

[57] Brizzolari, C. and others. Measurement of the absolute detection efficiency of a DUNE X-ARAPUCA photon detector in liquid argon. Journal of Instrumentation, 18(04):P04034, 2023.

[58] A. Abed Abud et al. Deep Underground Neutrino Experiment (DUNE) Far Detector Technical Design Report, Volume VIII: DUNE FD2-VD. 12 2023.

[59] Abed Abud, A. and others (DUNE Collaboration). The DUNE Far Detector Vertical Drift Technology, Technical Design Report. Technical report, Fermilab, 2023.

[60] Sabrina Sacerdoti and DUNE Collaboration. Cryogenic Signal and Power transmission over Fiber in the DUNE Far Detector. In Proceedings of The European Physical Society Conference on High Energy Physics (EPS-HEP2025), volume 485, page 499, 2026.

[61] M. A. Arroyave et al. Characterization and novel application of power over fiber for electronics in a harsh environment. Journal of Instrumentation, 19(10):P10019, 2024.

[62] Koheron. Koheron PD100 photodetector, 2018.

[63] Teledyne LeCroy. Operator's Manual HDO6000B High Definition Oscilloscopes, 2024.